Observational and Numerical Studies of Solar Coronal Magnetic Field

Daiki Yamasaki

A thesis presented for the degree of

Doctor of Philosophy

Astronomical Observatory

Kyoto University

Japan

6th January 2023

Observational and Numerical Studies of Solar Coronal Magnetic Field

Daiki Yamasaki

Abstract

Solar flares are rapid energy-release phenomena via magnetic reconnection in the solar corona. It is widely accepted that the eruption of dark filaments which are the cool and dense plasma cloud in the hot solar corona drives magnetic reconnection during solar flares. Plasma materials of dark filaments are supported by a bundle of helical magnetic field lines, magnetic flux ropes (MFRs). However, due to observational limitations, it is hard to obtain the magnetic field structures of the MFRs directly, and thus, the magnetic field configuration of dark filaments is still under argument between two types; one is the normal polarity model proposed by Kippenhahn & Schlüter (1957), and the other is the reverse polarity model proposed by Kuperus & Raadu (1974). In addition, the formation process and the eruption mechanism of the MFRs have not yet been cleared.

In Chapters 2 and 3, to understand the evolution of the three-dimensional (3D) coronal magnetic field including MFRs, we performed a nonlinear force-free field extrapolation and a data-constrained magnetohydrodynamic simulation using a series of photospheric vector magnetic field data obtained from the Helioseismic and Magnetic Imager onboard the *Solar Dynamics Observatory*. In these studies, we focused on two large-scale solar flares which have *GOES*(: *Geostationary Operational Environmental Satellite*) flare class larger than X1: an X9 flare observed in an active region (AR) National Oceanic and Atmospheric Administration (NOAA) 12673 of 2017 September and an X1 flare observed in an AR NOAA 12887 of 2021 October. According to the investigation of the AR NOAA 12673, we found that a large MFR concerning the X9 flare formed 2 days before the onset of the flare. We suggested that the magnetic field reconfiguration via magnetic reconnection of several M flares took place several days before the onset of the X9 flare suppressed the MFR. From the results of the study on the AR NOAA 12887, we found that both the torus instability and the formation of the magnetic arcade below the MFR during the eruption contributed to the acceleration of the erupting MFR of the X1 flare.

In Chapter 4, we performed the spectro-polarimetric observation in the He I (10830 Å) line to investigate the magnetic field configuration of dark filaments. The observation was carried out with the Domeless Solar Telescope at Hida Observatory with a polarization sensitivity of 3.0×10^{-4}. We obtained 8 samples of filaments in quiet regions. As a result of the analysis of full Stokes profiles of filaments, we found that the field strengths were estimated as 8 - 35 G. By comparing the direction of the

magnetic field in filaments and the global distribution of the photospheric magnetic field, we determined the magnetic field configuration of the filaments, and we concluded that 6 out of 8 samples have normal polarity configuration, and 2 out of 8 have reverse polarity configuration.

Supervisor: Kiyoshi Ichimoto

Acknowledgements

First of all, I would like to express my great gratitude to my supervisor, Prof. K. Ichimoto. He have taken care of me for more than five years since I was an undergraduate student. I would like to thank Dr. S. Inoue for being a collaborater for two studies in this thesis. He invited me to New Jersey Institute of Technology for 3 months and my stay there with great hosts, Prof. H. Wang, Dr. J. Lee, and the other wonderful members was an excellent moment. Regarding the observational study, Dr. S. Nagata, Dr. S. UeNo, Dr. D. P. Cabezas, and Mr. Y. W. Huang were the powerful supporters at Hida Observatory. Prof. T. Yokoyama and Dr. A. Asai gave me some important comments on our study. I would also like to thank all the other observatory members. Regarding the numerical study, Dr. Y. Bamba was a helpful collaborater and Prof. K. Kusano gave me some critical advices to improve our study.

This work was supported by MEXT/JSPS KAKENHI Grant Number JP21J14036 and 21K20379. This work was also supported by MEXT/JSPS KAKENHI Grant Number JP15H05814, Project for Solar-Terrestrial Environment Prediction (PSTEP) and the computational joint research program of the Institute for Space-Earth Environmental Research (ISEE), Nagoya University. This work was also supported by MEXT/JSPS Overseas Challenge Program for Young Researchers. This study is partially supported by National Science Foundation AGS-2145253, AGS-1954737 and AST-2204384. This study is also supported by NASA grants, 80NSSC18K1705 and 80NSSC21K1671.

SDO is a mission of NASA's Living With a Star Program. This work utilizes data from the National Solar Observatory Integrated Synoptic Program, which is operated by the Association of Universities for Research in Astronomy, under a cooperative agreement with the National Science Foundation and with additional financial support from the National Oceanic and Atmospheric Administration, the National Aeronautics and Space Administration, and the United States Air Force. The GONG network of instruments is hosted by the Big Bear Solar Observatory, High Altitude Observatory, Learmonth Solar Obser-

vatory, Udaipur Solar Observatory, Instituto de Astrofisica de Canarias, and Cerro Tololo Interamerican Observatory.

Finally, I would like to appreciate great support of my family, especially devoted help by my beloved wife.

Contents

List of Figures

List of Tables

CHAPTER 1

General Introduction

1.1 The solar atmosphere

The solar atmosphere consists of roughly three layers of photosphere, chromosphere, and corona from lower to upper. In Figure 1.1, we show the temperature and the density profile with respect to the height in the solar atmosphere calculated with the VAL model (Vernazza et al., 1981). The typical temperature of the photosphere is about 6000 K and that of the chromosphere is about 10000 K. The temperature of the corona varies from 1 MK to more than 10 MK. There is a temperature minimum ($T_{\rm min}$) of about 4000 K between the photosphere and the chromosphere, and there is about a 2-order gap in temperature between the chromosphere and the corona. This region is called the transition region (TR). Regarding the mass density, it decreases as height increases. In the photosphere, the typical mass density is about 10^{-4} kg/m^3. In the chromosphere, it varies from 10^{-5} to 10^{-10} kg/m^3. In the corona, it is below 10^{-11} kg/m^3. We can also find a 1-order jump in density, in the TR.

Since the solar atmosphere is high temperature and low density, some of the atmospheric materials are ionized, $i.e.$, the solar atmosphere is partially ionized plasmas. Therefore, to understand the dynamics of plasma phenomena in the solar atmosphere, we need to consider both the gas dynamics and the interaction between plasmas and magnetic field. To discuss which is more dominant in the dynamics of the plasma, we often use a key parameter of plasma β, which is defined as follows; $\beta = p_{\rm gas}/p_{\rm mag}$, where $p_{\rm gas}$ and $p_{\rm mag}$ are the gas pressure and the magnetic pressure, respectively. If $\beta > 1$, then the gas dynamics are superior to the interaction between plasma and magnetic field, and if $\beta < 1$, then the case is the opposite. In Figure 1.2, we show the one-dimensional β profile proposed by Gary (2001). As shown in the figure, in the photosphere and in the lower chromosphere, $\beta > 1$, and in the upper chromosphere and in the corona, $\beta < 1$.

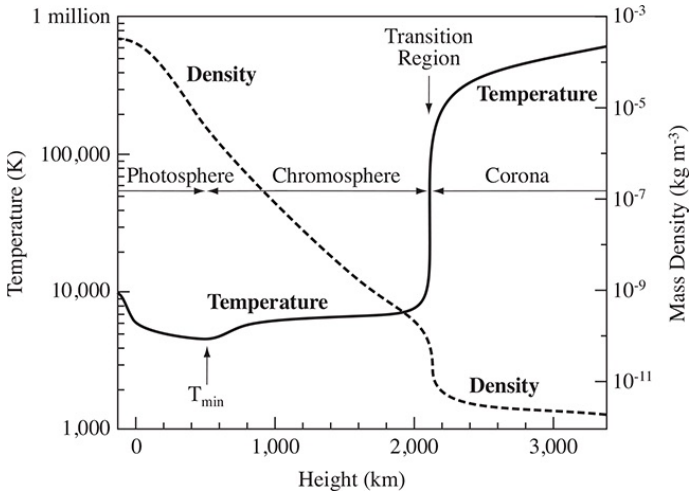

Figure 1.1: One-dimentional temperature and mass density profile of solar atmosphere. Solid and dashed lines correspond to temperature and mass density, respectively. $T_{\min}$ denotes the location of the temperature minimum. From Priest (2020)

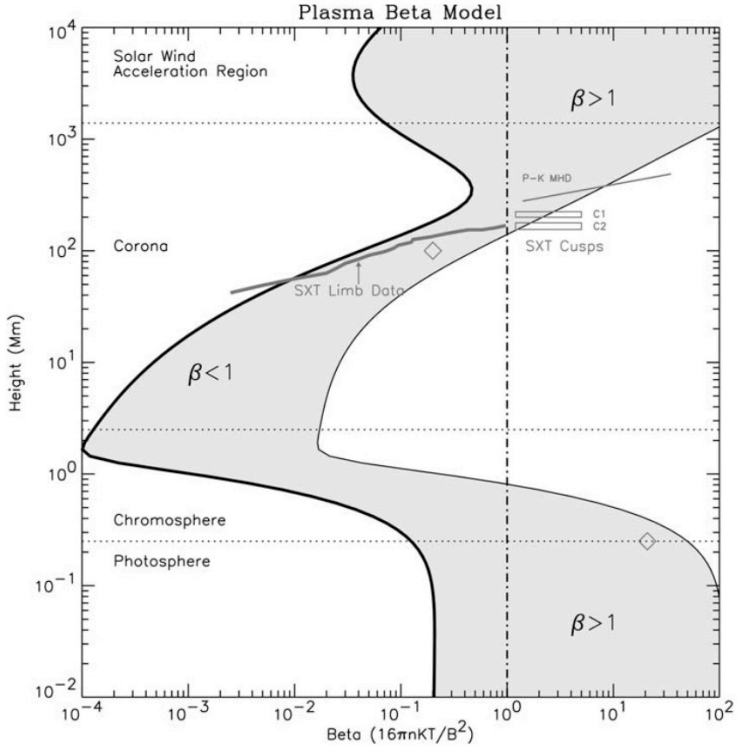

Figure 1.2: Plasma β profile of the solar atmosphere. Original figure is from Gary (2001).

1.2 Solar flares

1.2.1 Overview and Observations

Solar flares are the rapid energy release phenomena in the solar corona. The energy source of the flares is widely thought to be the magnetic free energy stored in the coronal magnetic field (Priest & Forbes, 2002). The typical released energy varies in 10^{28-32} erg. The first observation of solar flares was reported by Carrington (1859) and Hodgson (1859), and they observed the flare in white light. Then, according to the development of the instrumentations and observation techniques, solar flare observation has been performed by spectroscopic observation in the visible and near-infrared from ground-based telescopes and in X-rays or in extreme ultraviolet (EUV) from space satellites. It is now well known that during solar flares, enhancements in the wide range of the wavelength, from radio to γ-ray are observed (see Figure 1.3). As shown in Figure 1.3, the temporal evolution of the flares consists of three phases: precursor, impulsive phase, and gradual phase. In precursor, we observe enhancements in X-rays (< 30 KeV) and in extreme ultraviolet (EUV) which typically last for less than 5 minutes. In the impulsive phase, we observe drastic enhancements in X-rays (> 10 KeV), EUV, and microwave radio within several minutes. Soon after the impulsive phase, we observe a gradual decrease of emissions in whole the wavelength range for ~ 30 minutes in the gradual phase.

1.2.2 Standard model

During the solar flare, rapid energy conversion from magnetic energy to radiation, thermal energy, and energy of accelerated particle takes place via the magnetic reconnection (Shibata & Magara, 2011). By taking into account the magnetic reconnection as a key process, Carmichael (1964), Sturrock (1966), Hirayama (1974), and Kopp & Pneuman (1976) proposed the standard model of the solar flare: CSHKP model. In Figure 1.4, we display the schematic of the standard model drawn by Shibata et al. (1995). In this model, an eruption of plasmoids which are the magnetic cloud in the coronal magnetic field induces rapid inflow at a point below the plasmoid and results in the magnetic reconnection at the point. According to the successive magnetic reconnection, plasma outflow is accelerated by slow shock formed below the reconncetion point. Then the accelerated plasmas follow the magnetic field lines of coronal loops and hit the upper chromosphere at the footpoints of the coronal loops. Since the chromosphere is a high-density region compared to the corona, penetrating accelerated particles heat the chromosphere and result in plasma evaporation. The heated chromosphere appears as flare ribbons, they are typically observed in the Hα line (see Figure 1.5). Eventually, the evaporated plasmas fill the coronal loop and they appear as flare loops observed in soft X-rays or in EUV lines. Several observations

support this model; Tsuneta et al. (1992) and Tsuneta (1996) reported that the cusp-shape enhancement in coronal loops by X-ray observation with the $Yohkoh$ observations (see Figure 1.6), and Masuda et al. (1994) presented that the location of hard X-ray sources well matched to the location of the loop top and two footpoints of the loops (see also Figure 1.7).

1.2.3 Effects on the space weather

Solar flares are the most energetic phenomena in the solar system and they affect the electromagnetic environment of interplanetary space via a sudden increase of X-ray emissions, solar energetic particles (SEPs: Desai & Giacalone, 2016) which are often caused by coronal mass ejections (CMEs: Parenti, 2014) accompanied by solar flares, and interplanetary disturbances in a magnetic field (see also Kihara et al., 2020). In Figure 1.8, we display the effects of solar activities on the Earth and interplanetary space. Since our advanced civilization highly relies on space technologies such as GPS and other satellite systems, aircraft transportation, the international space station (ISS), and so on, it is critical to forecasting the effects of solar flares. This is called the space weather study, and one of the most important topics in the space weather study to comprehensively understand the connection between solar flares and CMEs. Since the core structure of CMEs is thought to be a bundle of twisted coronal magnetic field lines or magnetic flux ropes (MFRs: Xu et al., 2012; Hanaoka & Sakurai, 2017; Gibson, 2018) which is often formed in ARs, it is critical to clarify the flare-productive three-dimensional (3D) coronal magnetic field.

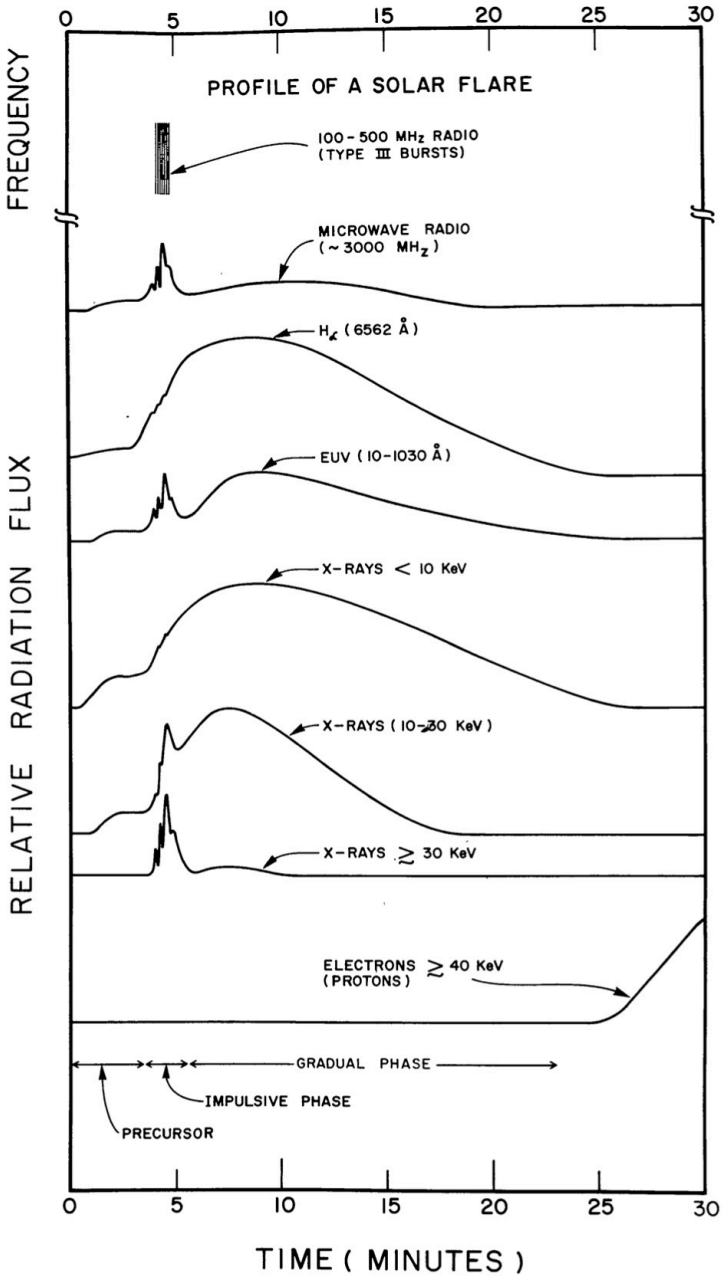

Figure 1.3: Temporal evolution of the multi-wavelength emissions during solar flares. From top to bottom plots are corresponding to $100 - 500$ MHz radio, microwave radio with ~ 3000 MHz, Hα (6563 Å), extreme ultraviolet ($10 - 1030$ Å), X-rays of < 10 keV, X-rays of $10 - 30$ keV, X-rays of > 30 keV, and electrons with > 40 keV. From Kane et al. (1974)

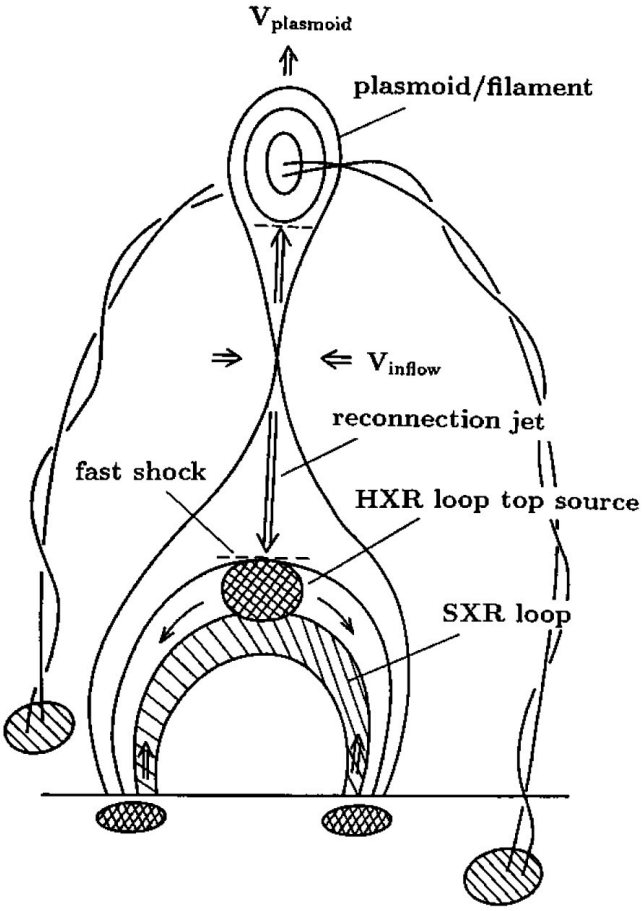

Figure 1.4: Standard unified model of filament eruptions and solar flares. Black solid lines show the coronal magnetic field. Helical structure represents the filament. The vertical cross-section of the filament corresponds to the plasmoid. V_{inflow} and V_{plasmoid} represent the inflow and outflow velocities to and from the reconnection point, respectively. Original figure is presented by Shibata et al. (1995).

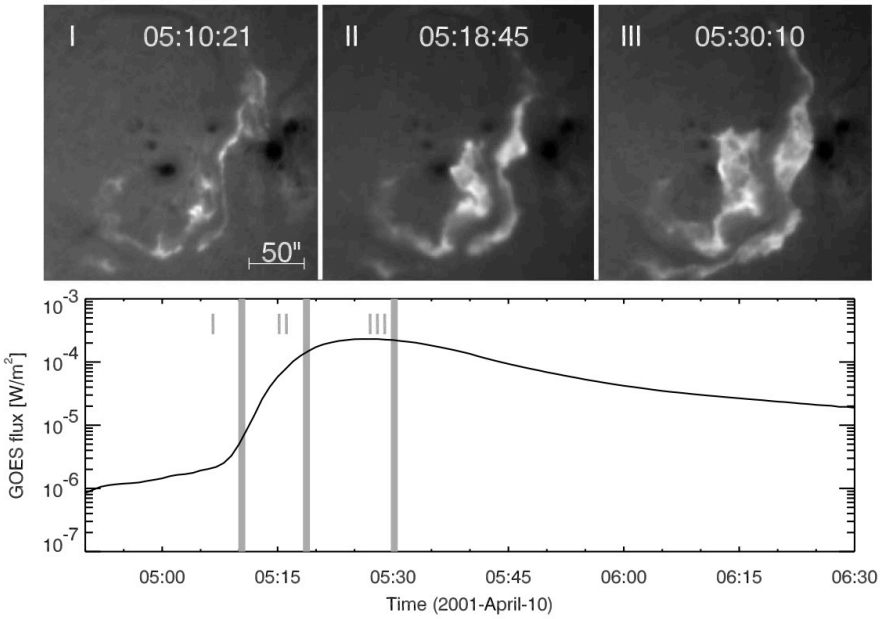

Figure 1.5: Top three panels show the temporal evolution of flare ribbons of the flare observed on April 10, 2001. Bottom panel show the soft X-ray light curve observed by the $GOES$ $1.0 - 8.0$ Å channel. Original figure can be found in Asai et al. (2004).

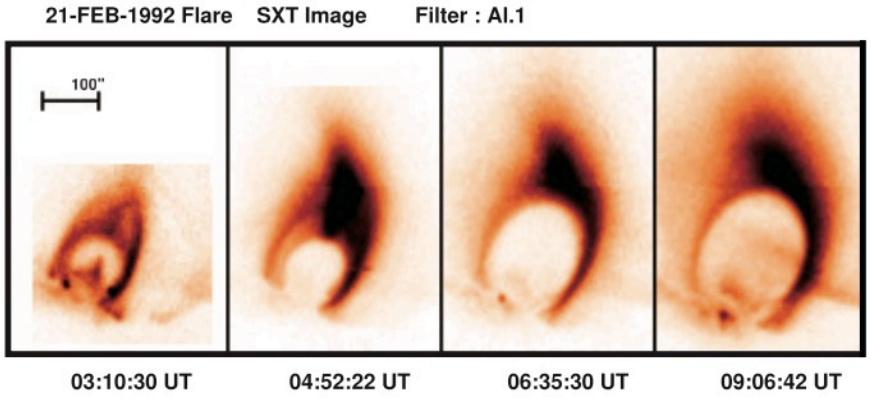

Figure 1.6: Cusp-shape structure observed in X-ray with $Yohkoh$ in the flare of Feburary 21, 1992. See also Tsuneta et al. (1992) and Tsuneta (1996).

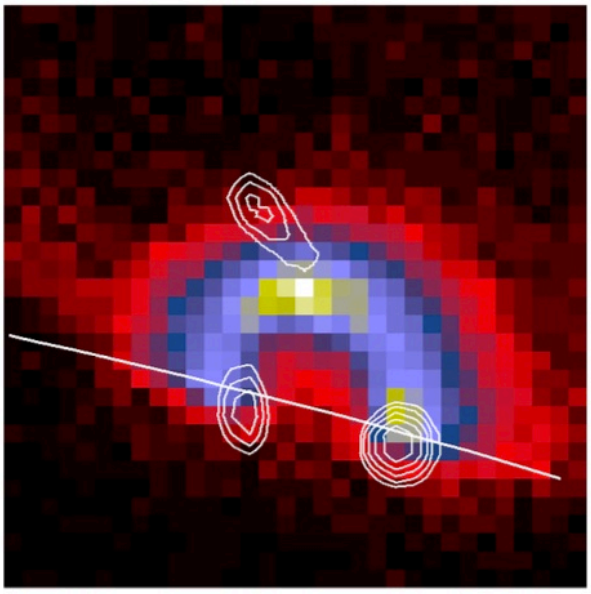

Figure 1.7: Colors represent the intensity of soft X-ray from flare loops. White contours show the location of the hard X-ray sources. The target event was the flare of January 13, 1992. From Masuda et al. (1994).

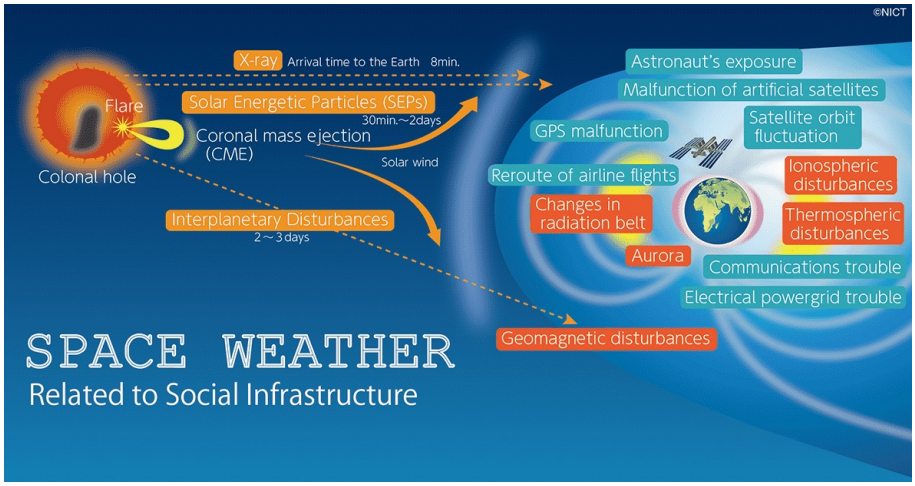

Figure 1.8: Schematics of the comprehensive view of effects of solar activities on the Earth and interplanetary space: space weather. ©NICT.

1.3 Magnetic flux ropes

As we mentioned in Section 1.2, an eruption of plasmoids is a driver of rapid magnetic reconnection during solar flares. According to some studies of 3D coronal magnetic field structure in flaring regions, MFRs are thought to be a 3D view of the plasmoids. In this section, we present extrapolation methods of 3D coronal magnetic field in Section 1.3.1, formation process of MFRs in Section 1.3.2, trigger of eruptions of MFRs in Section 1.3.3, and acceleration mechanism of MFRs in Section 1.3.4.

1.3.1 Extrapolation of 3D coronal magnetic field

Due to observational limitations, it is hard to observe the coronal magnetic field directly. Thus, we need to extrapolate them by using photospheric vector magnetic field data to obtain 3D coronal magnetic field. Since the solar atmosphere consists of magnetized plasmas and the Magnetohydrodynamic (MHD) approximation can be applied, the equation of motion (EOM) of coronal plasmas can be written as follows:

$$\rho \frac{d\boldsymbol{v}}{dt} = -\boldsymbol{\nabla} p + \frac{1}{4\pi}(\boldsymbol{\nabla} \times \boldsymbol{B}) \times \boldsymbol{B} + \rho \boldsymbol{g}_{\odot}, \tag{1.1}$$

where ρ, $\boldsymbol{v}$, $\boldsymbol{B}$, and p are the density, velocity, magnetic field, and gas pressure, respectively. $\boldsymbol{g}_{\odot}$ represents the gravitational acceleration of the sun. The first, the second, and the last terms of the right side of the EOM correspond to gas pressure gradient, the Lorentz force, and gravitational force, respectively. As we mentioned in Section 1.1, in the solar corona, the density is low enough, and the magnetic pressure is much more dominant compared to the gas pressure, *i.e.*, $\beta < 1$. Thus, the gravity and the gas pressure are negligible compared to the Lorentz force. In such a condition, to achieve a dynamical equilibrium, the magnetic field can be expected to meet a condition as follows:

$$\boldsymbol{\nabla} \times \boldsymbol{B} = \alpha \boldsymbol{B}, \tag{1.2}$$

where α is a constant value called as force-free α. The magnetic field which satisfies the force-free condition (in eq. 1.2) is called force-free field.

Force-free field is categorized into three types with different conditions of force-free α; potential field (PF) with $\alpha = 0$, linear force-free field with uniform α through a system, and nonlinear force-free field (NLFFF) with non-uniform α through a system. There are some robust techniques that can extrapolate nonlinear force-free field with observed photospheric vector magnetic field as a bottom boundary condition (Wiegelmann & Sakurai, 2012). Some of the NLFFF extrapolation methods are based on the MHD equations (Inoue et al., 2014b; Inoue, 2016). This kind of observation-based 3D coronal magnetic field is useful to understand the evolution of coronal magnetic field including MFRs in ARs. In

addition, by using 3D NLFFF and PF, we can estimate the accumulated magnetic free energy in ARs by the following equation:

$$E_{\rm free} = \frac{1}{8\pi}\int_V \left(\boldsymbol{B}_{\rm nlfff} - \boldsymbol{B}_{\rm pf}\right)^2 dV, \tag{1.3}$$

where $\boldsymbol{B}_{\rm nlfff}$ and $\boldsymbol{B}_{\rm pf}$ correspond to 3D NLFFF and PF, respectively.

1.3.2 Formation process of magnetic flux ropes

Magnetic field structure of MFRs strongly deviates from the potential field, which corresponds to the lowest energy state with a given boundary condition. Therefore, understanding the formation process of MFRs leads to comprehension of the energy build-up of ARs. MFRs can be formed in two ways; one is by flux emergence, and the other is by magnetic reconnection (Filippov et al., 2015). The former claim that magnetic flux tubes which have helical field lines are generated in the solar interior and emerged into the solar surface via magnetic buoyancy (Okamoto et al., 2008; Toriumi & Wang, 2019). The latter is that the photospheric motions such as conversion flows, shear motions, and sunspot rotations induce magnetic reconnection of coronal magmetic field and result in the formation of MFRs. For instance, van Ballegooijen & Martens (1989) proposed the tether-cutting (TC) reconnection scenario in which the reconnection between preexisting magnetic field lines creates MFRs (see Figure 1.9).

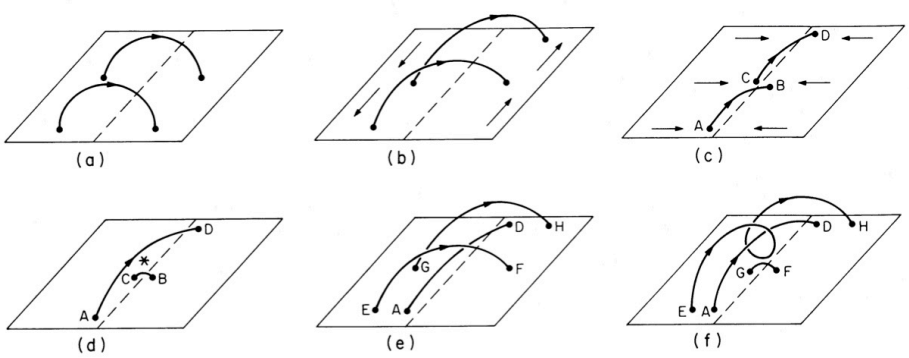

Figure 1.9: Schematics of the tether-cutting reconnection. From van Ballegooijen & Martens (1989).

1.3.3 Trigger of magnetic flux rope eruptions

Once MFRs are formed in ARs, MFRs lose their dynamical equilibrium and result in eruptions. There are some candidates for "trigger" mechanisms that disrupt the equilibrium of MFRs. One is the kink instability (KI) which is one of the ideal MHD processes (Török

& Kliem, 2004, 2005). The magnetic twist is a proxy of the instability, and the magnetic twist is defined as follows:

$$T_{\rm w} = \int_L \frac{\boldsymbol{\nabla} \times \boldsymbol{B} \cdot \boldsymbol{B}}{4\pi B^2} dl, \tag{1.4}$$

where dl is a line element and L is an integral path along field lines (see also Berger & Prior, 2006). In Figure 1.10, we display a comparison between an observed erupting MFR and the kink-unstable MFR in a numerical simulation. The observation was performed in 195 Å with the *Transition Region and Coronal Explorer* (*TRACE*: Handy et al., 1999). In the Figure, we can find good agreement with each other.

The other candidate is the double-arc instability (DAI) proposed by Ishiguro & Kusano (2017) and Kusano et al. (2020). They extended the TC reconnection scenario into an MHD instability. In their model, they consider a pair of two arcs as an initial condition. Then, the reconnection between two arcs results in the formation and the eruption of MFRs. A proxy of this instability is given as follows:

$$\kappa = \frac{\alpha d}{4} \frac{\Phi_{\rm rec}}{\Phi_{\rm total}}, \tag{1.5}$$

where α and d represent a force-free α and a diameter of single arc, which is consequently formed by the reconnection between two arcs, respectively. $\Phi_{\rm rec}$ and $\Phi_{\rm total}$ represent the reconnected magnetic flux and the overlying magnetic flux, respectively. They analytically proposed the critical value as $\kappa > 1/4\pi$. The schematics of the DAI are shown in Figure 1.11. By studying a flaring region observationally, Muhamad et al. (2018) pointed out that the DAI analysis can be applied to actual ARs.

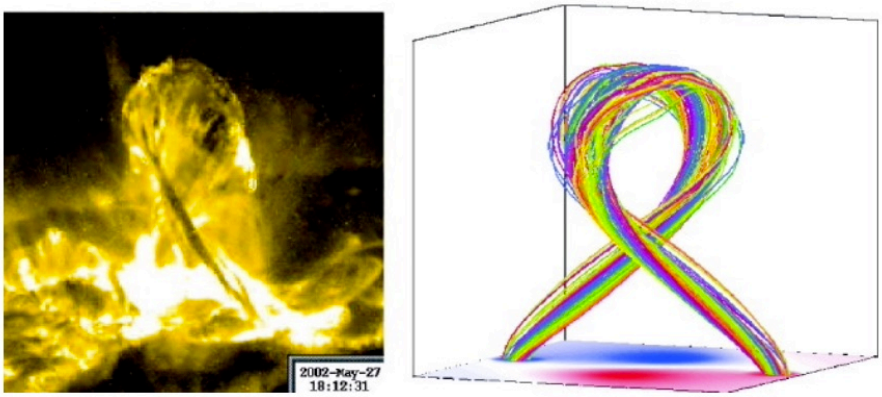

Figure 1.10: Schematics of the kink instability. Left figure is an erupting MFR observed with *TRACE* in 195 Å. Right figure show a kink-unstable MFR in numerical simulation. From Török & Kliem (2005).

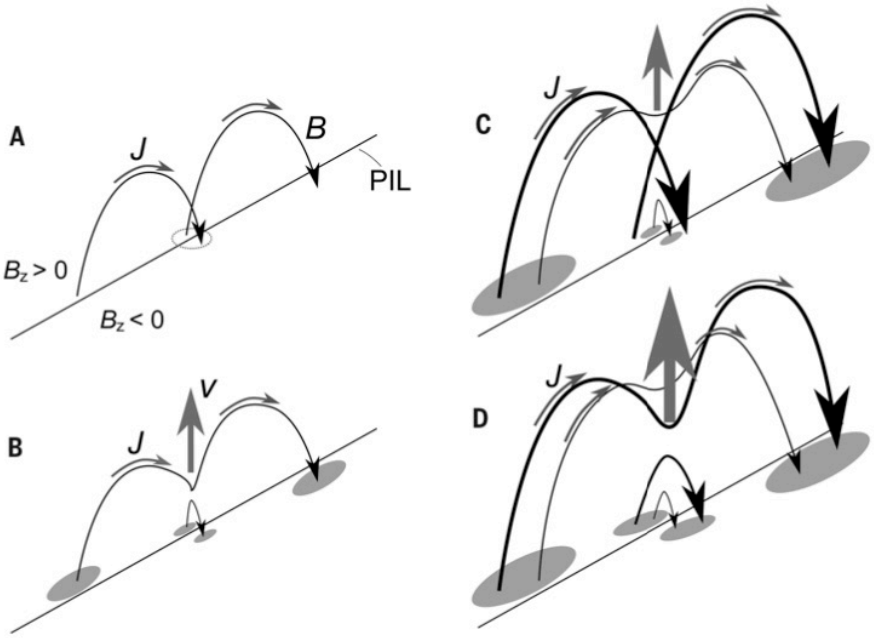

Figure 1.11: Schematics of the double-arc instability. Panels A, B, C, and D show a temporal evolution of the formation and eruption process of MFRs. Original figure can be found in Kusano et al. (2020).

1.3.4 Acceleration mechanism of erupting magnetic flux ropes

The candidates of an acceleration mechanism of erupting MFRs are the followings: magnetic breakout (Antiochos et al., 1999; Karpen et al., 2012), the torus instability (TI: Kliem & Török, 2006), and magnetic reconnection (Jiang et al., 2021).

In Figure 1.12, we display schematics of the magnetic breakout. There is a two-step reconnection in magnetic breakout; one is breakout reconnection which takes place above MFRs to reduce the magnetic pressure on MFRs (see panels (a) and (b) in Figure 1.12), the other is flare reconnection which occurs below MFRs (see panel (c) in Figure 1.12).

Regarding the TI, we consider the force balance between the magnetic tension force which suppresses MFRs and the hoop force which pushes MFRs upward by interaction between the external field and the electric current of MFRs (Priest, 2014). We often use the decay index (n) as a proxy of the TI which is defined as follows:

$$n = -\frac{z}{|\boldsymbol{B}|}\frac{\partial|\boldsymbol{B}|}{\partial z}, \tag{1.6}$$

where z represents a radial direction and $\boldsymbol{B}$ is an external magnetic field. The critical value of the decay index ($n_{\rm crit}$) is thought to be $n_{\rm crit} = 1.5$ or below (Jing et al., 2018). In Figure 1.13, we show an example of an MFR and the decay index distribution in the

vertical cross-section. As presented in the Figure, the MFR locates at the region with a high decay index value of $n > 1.0$, and the MFR has upward velocity, $i.e.$, the MFR is erupting via the TI. In Figure 1.14, we show a statistical study of the MHD instabilities of the TI and the KI (Jing et al., 2018). In the case of ejective events, both the magnetic twist and the decay index have their peak in between 0.5 and 1.0, and in the case of confined events, both of them are below the case of ejective events.

The last candidate is one-step magnetic reconnection which takes place below MFRs (Jiang et al., 2021). They performed an MHD simulation and successfully produced an eruption without magnetic breakout or the TI. In Figure 1.15, we display the temporal evolution of an erupting MFR in 2D view.

In Table 1.1, we summarized data-based MHD simulation studies of large-scale solar flares with MFR eruptions. All the studies use NLFFF as the initial conditions of the simulation. In the table, we show the suggested MFR acceleration mechanisms in each study. Regarding an X2.2 flare in AR NOAA 11158 and an X2.1 flare in AR NOAA 11283, all the studies concluded that the TI played a key role in MFR eruption (Inoue et al., 2014a, 2015; Jiang et al., 2013, 2018). However, regarding an X3.1 flare in AR NOAA 12192, Inoue et al. (2016) reported that the mechanism was the TI, and Jiang et al. (2016) and Prasad et al. (2018) presented that the magnetic breakout-like reconnection, null point reconnection (NPR) played a key role in an eruption. In addition, regarding an X9.3 flare in AR NOAA 12673, Inoue et al. (2018b) pointed out that the TI was the acceleration mechanism of the MFR, and Inoue & Bamba (2021) extended the scenario into the combination of successive X2.2 and X9.3 flare in the AR. As we describe, there are still only a few studies of data-based MHD simulation that pointed out the acceleration mechanism of MFRs in actual ARs.

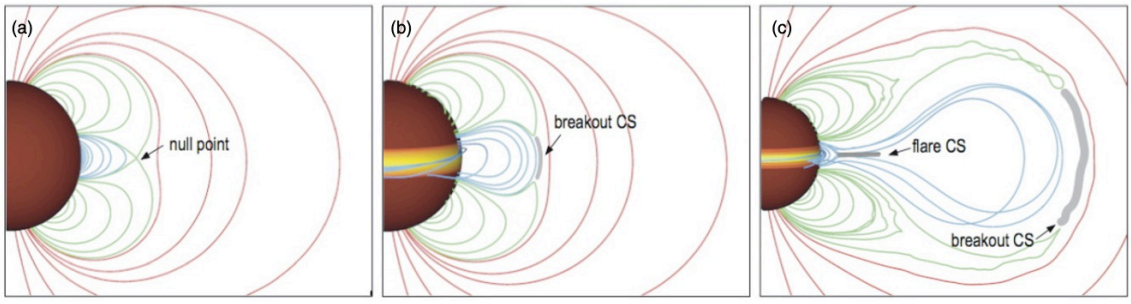

Figure 1.12: Schematics of the magnetic breakout. Panels (a), (b), and (c) show a temporal evolution of the breakout process. In breakout reconnection red and blue lines reconnect and form green lines. Original figure can be found in Karpen et al. (2012).

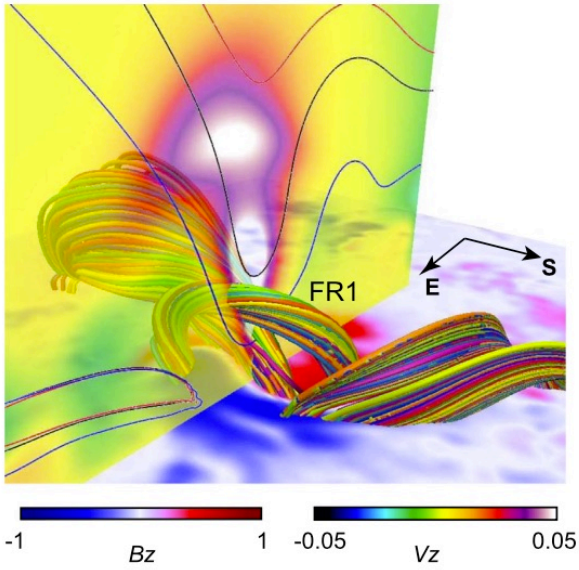

Figure 1.13: An MFR of AR NOAA 12673. Background red and blue color show radial component of the photospheric magnetic field. Colored lines represent the MFR. Vertical velocity is shown in the vertical cross-section. The blue, black, and red lines in the same cross-section correspond to the contours of decay index values of $n = 1.0$, 1.5, and 1.7, respectively. Figure is from Inoue et al. (2018b).

Table 1.1: MFR acceleration mechanisms suggested from data-based MHD simulation studies of flares larger than *GOES* X1 class

NOAA AR #	Year & Month	*GOES* class	Paper	the TI [1]	NPR [2]
11158	2011 Feb.	X2.2	Inoue et al. (2014a)	○	-
			Inoue et al. (2015)	○	-
11283	2011 Sep.	X2.1	Jiang et al. (2013)	○	-
			Jiang et al. (2018)	○	-
12192	2014 Oct.	X3.1	Inoue et al. (2016)	∗	-
			Jiang et al. (2016)	-	○
			Prasad et al. (2018)	-	○
12673	2017 Sep.	X9.3	Inoue et al. (2018b)	○	-
			Inoue & Bamba (2021)	○	-
12887	2021 Oct.	X1.0	Yamasaki et al. (2022a) [3]	∗	-

[1] The torus instability. Symbols of ○ and ∗ represent the scenario with TC reconnection which form MFRs and without TC reconnection, respectively.

[2] Null point reconnection.

[3] We introduce the detail in Chapter 4 of this thesis.

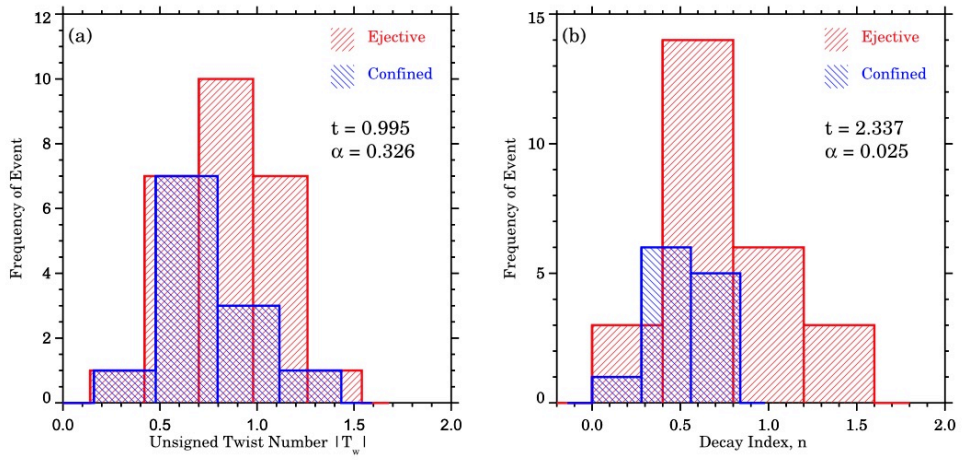

Figure 1.14: Histograms of (a) magnetic twist (T_{w}) and (b) the decay index (n). Red and blue correspond to ejective and confined events, respectively. Original figure can be found in Jing et al. (2018).

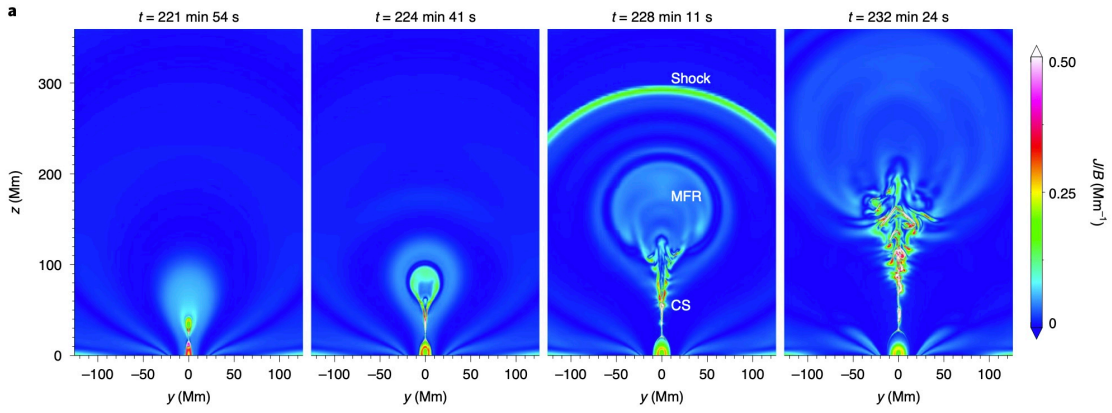

Figure 1.15: Temporal evolution of an MFR eruption. Evolution of the electric current density normalized by the magnetic field strength ($|\boldsymbol{J}|/|\boldsymbol{B}|$) are presented. From Jiang et al. (2021).

1.4 Solar filaments

1.4.1 Overview

Solar filaments (or solar prominences if we observe them on off-limb) are the cool and dense plasma clouds in the hot corona. The typical temperature and the density of filaments are 10^4 K and 10^9 cm^{-3}, respectively (Parenti, 2014; Okada et al., 2020). It is widely accepted that the plasma materials of filaments are suspended by a bundle of twisted magnetic field lines, MFRs (Xu et al., 2012; Gibson, 2018). They sometimes appear in solar ARs and sometimes in quiescent regions. The former is called AR filaments, and the latter is called quiescent (QS) filaments. Both the AR and QS filaments are usually observed above polarity inversion lines (PILs: Babcock & Babcock, 1955). In Figure 1.16, we show an example of solar filaments. In panels (a) and (b), we display an image obtained from Hα (6563 Å) observation and an image of Stokes V/I signals from the photosphere which corresponds to the line-of-sight component of the photospheric magnetic field. In the Figure, we can clearly find that the location of the filament is above the polarity inversion line in the photosphere.

Fine structures of solar filaments have been investigated for more than several decades (see Bommier & Leroy, 1998; Zirker et al., 1997; Martin, 1998; Pevtsov et al., 2003). In Figure 1.16 (a), we can find small threads in the filament body, and they are oriented in the same direction. It is now well known that the fine structures that appear in filaments in the northern and southern hemisphere show "dextral" and "sinistral" configurations, respectively. The "dextral" and "sinistral" configurations represent the clockwise and anticlockwise directions in the transverse component of the filaments' magnetic field from the axial direction of the filament body (see bottom cartoons in Figure 1.16). These fine structures are thought to be formed by following the magnetic field which suspend plasma materials of solar filaments.

Regarding the magnetic field configuration of solar filaments, there are two classical models proposed by Kippenhahn & Schlüter (1957) (normal polarity model) and Kuperus & Raadu (1974) (reverse polarity model). It is still under urgement between these two types and there are a number of observational studies that investigated the magnetic field configuration of solar filaments. For QS filaments, Bommier & Leroy (1998), Bommier et al. (1994), Martínez González et al. (2015), and Wang et al. (2020) reported that the configuration was reverse polarity. For AR filaments, Xu et al. (2012) reported that the configuration was reverse polarity while Sasso et al. (2014) and Yokoyama et al. (2019) proposed that the configuration was normal polarity. To clarify the magnetic field configuration of solar filaments, we need to obtain spatially resolved vector magnetic field of solar filaments and the photosphere.

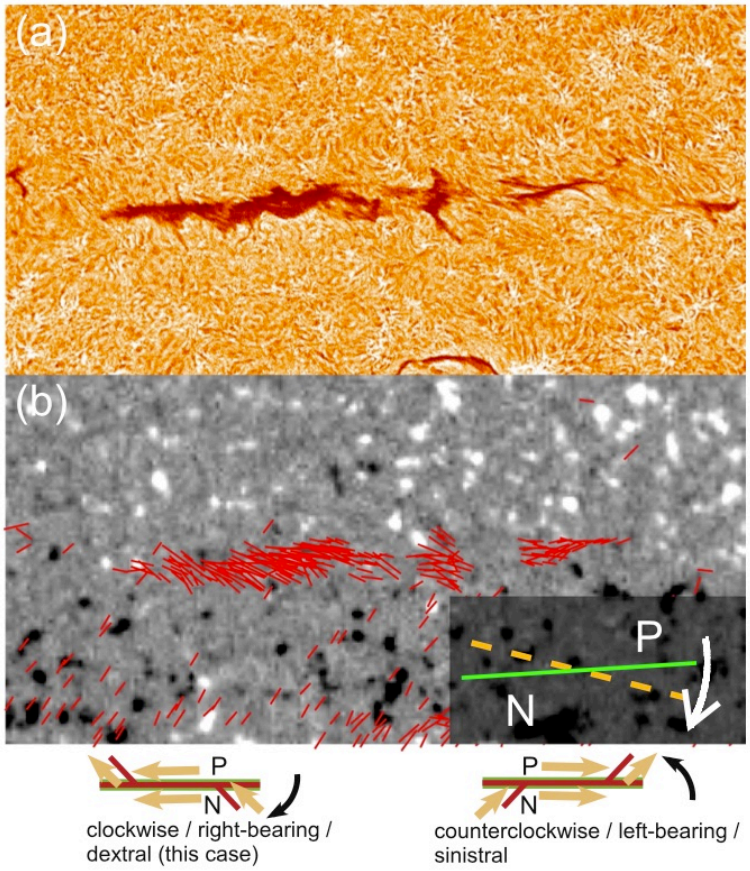

Figure 1.16: (a) Hα observation of a solar filament. (b) Background grayscale show Stokes V/I signal from photosphere which correspond to the line-of-sight component of the photospheric magnetic field. Red lines show directions of transverse component of the filament magnetic field. Bottom two cartoons represent the "dextral" and "sinistral" configuration of fine structure of solar filaments, respectively. From Hanaoka & Sakurai (2017).

1.4.2 Magnetic field observation: the photosphere

To obtain the vector magnetic field of the solar atmosphere, detecting the Zeeman effect (Zeeman, 1897) with spectro-polarimetric observation is one of the strongest methods. In presence of magnetic field, degeneracies of atomic levels are resolved and sub-levels appear. Some emissions from transitions between upper sub-levels and a lower ground level are resulting in a split of spectral lines. The split width can be determined by the following equation:

$$\Delta\lambda_B = \frac{e}{4\pi m_\mathrm{e} c^2}\lambda_0^2(M_\mathrm{u}g_\mathrm{u} - M_\mathrm{l}g_\mathrm{l})|\boldsymbol{B}|, \tag{1.7}$$

where $\Delta\lambda_B$ is a splitting width, e is an elecric charge, m_e is a mass of an electron, c is the light speed, λ_0 is the center wavelength of the considering spectral line, $M_\mathrm{u,l}$ and $g_\mathrm{u,l}$ correspond to magnetic quantum numbers and the Landé factors of uppler- and lower-

levels, respectively, and $|\boldsymbol{B}|$ is a magnetic field strength. If we adopt conditions of $g_{\rm u} = g_{\rm l} \equiv g$ and $M_{\rm u} - M_{\rm l} = 1$, then the splitting width can be written as follows:

$$\Delta\lambda_B = 4.67 \times 10^{-13} \lambda_0^2 g |\boldsymbol{B}|. \tag{1.8}$$

Here we note that the $\Delta\lambda_B$ and $\boldsymbol{B}$ shown above are in Å and in Gauss, respectively. Appearance of the Zeeman effect in spectral lines differes not only by the field strength but also by the angle between the magnetic field and the line-of-sight directions. In the case of a longitudinal magnetic field which is parallel to the line-of-sight direction,*i.e.*, the longitudinal Zeeman effect, the profile of circular polarization can be described as follows:

$$\varepsilon_V = \frac{h\nu}{4\pi} N_{\rm u} A_{\rm ul} \frac{1}{2} \left(\phi_{\sigma+} - \phi_{\sigma-}\right) \cos\theta, \tag{1.9}$$

where h is the Planck constant, ν is frequency of the light, $N_{\rm u}$ and $A_{\rm ul}$ are the population of upper level and the Einstein A coefficient of upper to lower levels, respectively. θ is the inclination angle between the line-of-sight and the magnetic field directions. $\phi_{\sigma\pm}$ correspond to Voigt functions centered at the wavelength of $\lambda_0 \pm \Delta\lambda_B$, and they are called σ components. In the case of magnetic field with a transverse component with respect to the line-of-sight direction, *i.e.*, the transverse Zeeman effect, the profile of linear polarization can be described as follows:

$$\varepsilon_Q = \frac{h\nu}{4\pi} N_{\rm u} A_{\rm ul} \frac{1}{2} \left(\phi_\pi - \frac{\phi_{\sigma+} + \phi_{\sigma-}}{2}\right) \sin^2\theta \cos 2\chi, \tag{1.10}$$

where ϕ_π is a Voigt function at the wavelength of λ_0, and it is called as π component. χ represents the azimuthal angle of the transverse component of the magnetic field. By observing the polarization profiles of the spectral lines, we can diagnose the vector magnetic field by using the relation shown in equations (1.9) and (1.10).

One of the most representative lines which have sensitivity in the photospheric magnetic field via the Zeeman effect is the Fe I 6302 Å line. This line has the Landé factor of 2.50. The Solar Optical Telescope (SOT: Tsuneta et al., 2008; Suematsu et al., 2008; Shimizu et al., 2008; Ichimoto et al., 2008) onboard the *Hinode* satellite (Kosugi et al., 2007) observes this line. The Tandem Etalon Magnetograph (TEM: Nagata et al., 2014; Yamasaki et al., 2022b) of the Solar Magnetic Activity Research Telescope (SMART: UeNo et al., 2004) at Hida observatory also observes this line. The other famous line is the Fe I 6173 Å line which has the Landé factor of 2.50. The Helioseismic and Magnetic Imager (HMI: Scherrer et al., 2012) onboard the *Solar Dynamics Observatory* (*SDO*: Pesnell et al., 2012) observes this line.

1.4.3 Magnetic field observation: the chromosphere

There are several spectral lines which have sensitivity in the chromosphere. In Table 1.2, we summarized the line information: the wavelength, the effective Landé factor, and the

detectable magnetic field strength of a line-of-sight component via the longitudinal Zeeman effect with the polarimetric sensitivity of 10^{-4}. The formation heights of some of these lines are displayed in Figure 1.17. Since the ultraviolet lines are strongly absorbed in the Earth's atmosphere, for the Mg II h & k (2803 and 2796 Å) and the Lyα (1216 Å) lines observations we need to go to space (cf. Ishikawa et al., 2017).

Among the lines in Table 1.2, the He I 10830 Å is one of the most suitable lines for magnetic field detection of solar dark filaments (Hanaoka & Sakurai, 2017). This is because the line is formed in the upper chromosphere, and the line is optically thin (see Figure 1.17). In addition, there is the Si I 10827 Å line, which is sensitive to the photospheric magnetic field, near the He I 10830 Å line. In Figure 1.18, we display the Grotorian diagram of the He I atom. As shown in the Figure, the He I 10830 Å line is the triplet including the transitions of $3P_0 \rightarrow 3S_1$ (10829.08 Å), $3P_1 \rightarrow 3S_1$ (10830.25 Å), and $3P_2 \rightarrow 3S_1$ (10830.34 Å).

In the case of anisotropically illuminated plasmas, the population imbalance of sub-levels appears and results in scatter polarization, which only appears in linear polarization. The maximum polarization signals of scatter polarization for the representative lines of chromospheric observations are presented in the last column of Table 1.2. If magnetic field exist, the scatter polarization signal is depolarized according to the direction of magnetic field, and this is called the Hanle effect (Hanle, 1924). The formula which represents the maximum magnetic field strength ($B_{\rm crit}$ in Gauss) to which the Hanle effect can be sensitive is given as follows:

$$B_{\rm crit} \quad = \quad \frac{A_{\rm ul}}{g} 10^{-6}, \tag{1.11}$$

where g is the Landé factor, $A_{\rm ul}$ represents the Einstein A coefficient (see also Trujillo Bueno et al., 2002). The advantage of using the Hanle effect for the vector magnetic field diagnostics is that the relatively weak field can be detected. However, polarization signals by the Hanle effect saturate around $B_{\rm crit}$ (e.g. ~ 8 Gauss in the case of He I 10830 Å). In contrast, the longitudinal and the transverse Zeeman effects allow us to detect the field strength of more than 10 and 200 Gauss, respectively in the He I 10830 Å line with polarimetric sensitivity of $\sim 10^{-4}$. Therefore, the combination of the Zeeman and the Hanle effect is a powerful method to analyze a wide-range vector magnetic field.

Table 1.2: Spectral lines which have sensitivity in choromospheric magnetic field (Courtesy of Prof.Ichimoto)

Line	Wavelength [Å]	Effective Landé factor ($g_{\rm eff}$)	Detectable $B_{\rm l}$ [1] [Gauss]	Scatter polarization [%]
He I	10830	multi [2,3]	~ 10	0.35
Ca II	8542	1.10	32	0.02
Hα	6563	multi [2]	140	-
Na I D	5896	1.33	10	0.0
	5890	1.17	12	0.5
He I D3	5876	multi [2]	-	-
Mg I	5172	1.75	14	0.25
Hβ	4861	multi [2]	97	-
Ca II H	3968	1.33	97	0.0
K	3933	1.17	130	0.5
Mg II h	2803	1.33	97	0.0
k	2796	1.17	130	0.5
Lyα	1216	multi [2]	-	-

[1] By observing the longitudinal Zeeman effect with the polarimetric sensitivity of 10^{-4}.

[2] There are multiple values in one line.

[3] $g_{\rm eff} = 2.00$ for $3P_0 \rightarrow 3S_1$, $g_{\rm eff} = 1.75$ for $3P_1 \rightarrow 3S_1$, $g_{\rm eff} = 1.25$ for $3P_2 \rightarrow 3S_1$

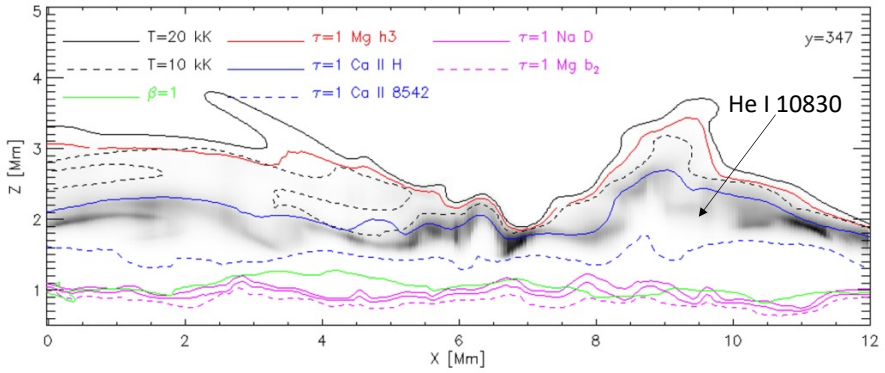

Figure 1.17: Formation heights of spectral lines which have sensitivity in choromospheric magnetic field. Black solid and dashed lines correspond to the temperature contours of 20 kK and 10 kK, respectively. Green solid line correspond to the height where the plasma $\beta = 1$. Red solid line, blue solid line, blue dashed line, pink solid line, and pink dashed line represent the formation heights of the Mg II h line, the Ca II H line, the Ca II (8542 Å) line, the Na I D line, and the Mg I triplet b2 line, respectively. Grey-scale rendering show the contribution function of the He I 10830 Å. From de la Cruz Rodríguez & van Noort (2017).

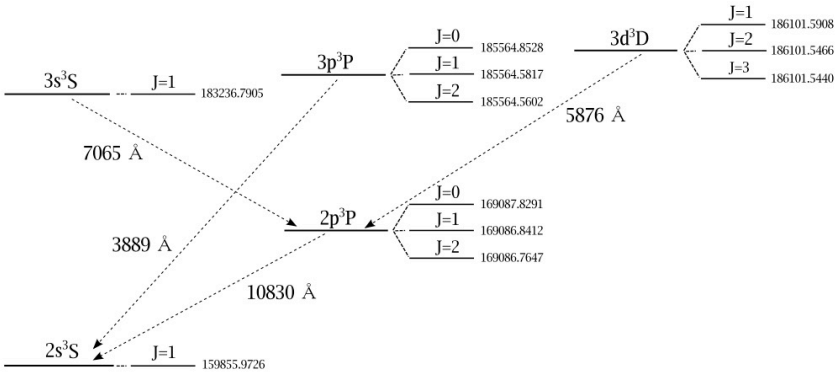

Figure 1.18: Grotorian diagram of the He I line. From Asensio Ramos et al. (2008).

1.5 Aim of this thesis

As we presented in Section 1.2, solar flares are the energetic explosive phenomena that sometimes cause serious effects on the Earth and interplanetary space by accompanying CMEs and SEPs. Since the core structure of CMEs are thought to be MFRs or solar filaments, it is improtant to clarify the formation process and the acceleration mechanism of MFRs in 3D view. In Section 1.3, we presented that one of the most powerful methods to investigate MFRs in ARs is a NLFFF extrapolation. In addition to them, as we described in Section 1.4, diagnostics of magnetic field configuration of solar filaments by direct observation is important.

The aims of this thesis are follows:

- To comprehensively understand the formation process of MFRs in a flare-productive AR (presented in Chapter 2).
- To clarify the acceleration mechanism of an erupting MFR (presented in Chapter 3).
- To observationally investigate the magnetic field configuration of MFRs which support solar dark filaments (presented in Chapter 4).

In Chapter 2, we performed a NLFFF modeling and reconstructed 3D coronal magnetic field above a flare-productive AR NOAA 12673 of 2017 September and investigated the evolution process of MFRs in the AR for more than 2 days before the onset of the X9 flare, which was the largest flare observed in the AR. In Chapter 3, we elaborated on a data-based MHD simulation of X1 flare observed in an AR NOAA 12887 of 2021 October with an extrapolated NLFFF as an initial condition and investigated the acceleration mechanism of an MFR which produced the X1 flare. In Chapter 4, we developed a spectro-polarimeter of the Domeless Solar Telescope at Hida Observatory and performed spectro-polarimetric observations in the He I 10830 Å line on 8 solar dark filaments, and diagnosed not only the magnetic field strength but also the magnetic field configuration of the filaments.

CHAPTER 2

Evolution of the Non-potential Magnetic Field in the Solar Active Region 12673 Based on a Nonlinear Force-Free Modeling

In this chapter, we focus on AR NOAA 12673 of 2017 September. By using a nonlinear force-free field modeling, we clarify the formation process of MFRs in the flare-productive AR. In addition, we discuss a relation between the formation of MFRs and an onset mechanism of an M5.5 flare which was observed 2 days before an X9.3 flare, which was the largest flare observed in the targeting AR.

2.1 Introduction

As we presented in Section 1.2, solar flares are widely considered to be releases of the magnetic energy accumulated in the solar corona. They are often observed in solar active regions (ARs) where the magnetic fields are highly deviated from the potential magnetic field that corresponds to the lowest energy state (see Section 1.3 and Priest & Forbes, 2002). Shearing and converging motions of the photosphere highly deform the coronal magnetic field, resulting in accumulated free magnetic energy. As introduced in Section 1.3, magnetic flux rope (MFR), which is a bundle of helical magnetic field lines, is formed in the lower corona via flux emergence, photospheric motions, and reconnection (van Ballegooijen & Martens, 1989; Okamoto et al., 2008; Filippov et al., 2015; Cheng et al., 2017). Since the MFR accumulates the free magnetic energy, it becomes a source of solar eruptions. The eruption of the MFR drives magnetic reconnection, which plays an important role in the energy release of the solar flares (Shibata & Magara, 2011), and coronal mass ejections (CMEs; Chen, 2011; Schmieder et al., 2015).

AR 12673 came at the end of August 2017 and was the most flare-productive AR in solar cycle 24. It produced many M-class flares and several X-class flares from September 2 to 10, among which an X9.3 flare was the largest, and produced a geo-effective CME (Yan et al., 2018; Shen et al., 2018; Chertok et al., 2018; Soni et al., 2020). AR 12673, at first, appeared as a monopole sunspot observed at the east solar limb in August 29. On September 3 and 4, two dipoles emerged beside the pre-exisiting sunspot, and the AR evolved into the complex δ sunspots (Yang et al., 2017). During the sunspot evolution in the AR, the negative polarity strongly intruded into the neighboring positive polarity before the X2.2 flare (Bamba et al., 2020), therefore this intrusion would play an important role in causing the X-flares. While these studies have been done, Inoue et al. (2018b) performed the data-constrained magnetohydrodynamics simulation focusing on X-class flares observed in September 6, and proposed that the erupting magnetic flux is formed by reconnection between twisted field lines existing above PIL before the flares.

As we mentioned above, many studies focus on the evolution of the AR and the onset mechanisms and dynamics of the X2.2 and X9.3 flares in terms of observational and numerical approaches. However, the overall evolution of the 3D magnetic field in this AR and flare activities before the ocurrence of the X-class flares are not investigated well. In this study, we investigate the evolution of the 3D magnetic field using a nonlinear force-free field (NLFFF) extrapolated from the photospheric magnetic field, and discuss the initiation of M-class flares observed before September 6. We focus on the M5.5 flare observed at 20:30 UT on September 4. Since this flare produced a geo-effective CME, our study is important also for the space weather forecaset. We eventually discuss a relationship between the M-class flare activities and the X-class flares which come later.

The rest of this paper is structured as follows: the observations and methods of analysis are described in Section 2.2, results are presented in Section 2.3, and important discussions arising from our findings are summarized in Section 2.4.

2.2 Methods

2.2.1 Observation

As is shown in the $GOES$ X-ray flux profile in Figure 2.1 (a), AR 12673 produced 12 M-class flares between 2017 September 4 and 5, prior to X9.3 on September 6 (Yang et al., 2017). In Figure 2.1 (b), we show the extreme ultraviolet image of the whole Sun on September 6 12:11 UT in 171Å observed by the Atmospheric Imaging Assembly (AIA; Lemen et al., 2012) on board the $Solar\ Dynamics\ Observatory$ (SDO; Pesnell et al., 2012). In the figure, AR 12673 is highlighted by the white box. Figure 2.1 (c) shows the photospheric vector magnetic field of AR 12673, observed at 18:00 UT on September 4 taken by the Helioseismic and Magnetic Imager (HMI; Scherrer et al., 2012) on board the SDO. Details of the vector magnetic field data reduction and other related information about HMI data products can be found in Hoeksema et al. (2014) and Bobra et al. (2014). In this image, which was taken approximately 2 hours before the M5.5 flare, 3 polarity inversion lines (PILs) and the sheared magnetic field lines along PILs can be identified.

2.2.2 Nonlinear force-free field extrapolation

Current observations cannot measure the coronal magnetic field directly. In order to obtain 3D magnetic fields in the corona, we performed a nonlinear force-free field extrapolation (Wiegelmann & Sakurai, 2012; Inoue, 2016; Guo et al., 2017). NLFFF extrapolations are carried out under the following assumptions: the plasma β in the solar corona is small (0.01-0.1), thus the gas pressure and gravity can be neglected to the Lorentz Force. The time scale of photospheric motions are much longer than that of the Alfven time scale, which characterizes the response time of the coronal magnetic field, so that the coronal magnetic field approximately evolves under a quasi-static state. Therefore, the evolution of the coronal magnetic field can be approximated by a series of NLFFF. In this study, we set the observed photospheric vector magnetic fields, which are preprocessed according to Wiegelmann et al. (2006), as the bottom boundary condition and calculated the 3D coronal magnetic fields to satisfy the force-free state. The extrapolation is performed using the following procedure: we first calculate the 3D potential field from the vertical component of the observed photospheric magnetic field according to Sakurai (1982). Next, we change the horizontal component of the bottom boundary from the potential field to the observed magnetic field, after that the horizontal components perfectly fit to the observed magnetic field. We continue the calculation of the coronal magnetic field with the fixed boundary condition until the field converges to the state with the minimum deviation from the force-free state. In this study, to obtain the force-free field, we employ the MHD relaxation method developed by Inoue et al. (2014b) and Inoue (2016). We solved the following

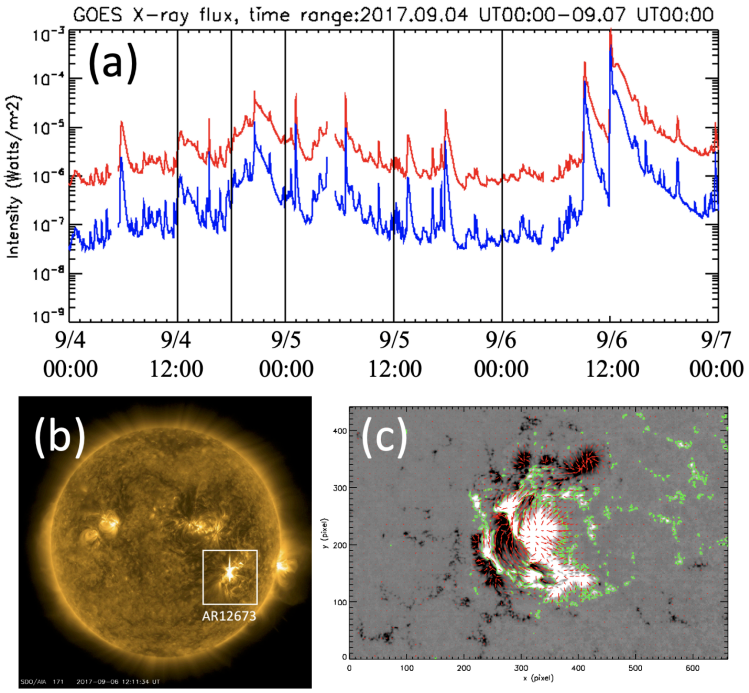

Figure 2.1: (a) Time profile of the soft X-ray flux between 2017 September 4 and 7 measured by the *GOES* 13 satellite. Red and blue lines correspond to the solar X-ray emission in the $1-8$Å and $0.5-4.0$Å passbands, respectively. Several M-class and X-class flares were observed in this AR. (b) Extreme-UV image of whole Sun observed at 171Å at the time of September 6 12:11 UT when the X9.3 flare was occurring. The white box shows the location of AR 12673. (c) Photospheric vector magnetic field taken at September 4 18:00 UT. Background gray scale and red arrows show the vertical and the horizontal component of the magnetic field respectively. Green lines show the PIL.

equations:

$$\rho = |\boldsymbol{B}|, \tag{2.1}$$

$$\frac{\partial \boldsymbol{v}}{\partial t} = -(\boldsymbol{v}\cdot\boldsymbol{\nabla})\boldsymbol{v} + \frac{1}{\rho}\boldsymbol{J}\times\boldsymbol{B} + \nu\boldsymbol{\nabla}^2\boldsymbol{v}, \tag{2.2}$$

$$\frac{\partial \boldsymbol{B}}{\partial t} = \boldsymbol{\nabla}\times(\boldsymbol{v}\times\boldsymbol{B} - \eta\boldsymbol{J}) - \boldsymbol{\nabla}\phi, \tag{2.3}$$

$$\boldsymbol{J} = \boldsymbol{\nabla}\times\boldsymbol{B}, \tag{2.4}$$

$$\frac{\partial \phi}{\partial t} + c_{\rm h}^2\boldsymbol{\nabla}\cdot\boldsymbol{B} = -\frac{c_{\rm h}^2}{c_{\rm p}^2}\phi, \tag{2.5}$$

where ρ, $\boldsymbol{B}$, $\boldsymbol{v}$, $\boldsymbol{J}$, and ϕ are plasma pesudo-density, magnetic flux density, velocity, electric current density, and a conventional potential to reduce errors derived from $\boldsymbol{\nabla}\cdot\boldsymbol{B}$ (Dedner et al., 2002). The pseudo-density in equation (2.1) is assumed to be propotional to $|\boldsymbol{B}|$. The Alfven velocity is uniform for the density model $\rho \propto |\boldsymbol{B}|^2$. In these equations, the length, magnetic field, density, velocity, time, and electric current density are normalized by $L^* = 240.0$ Mm, $B^* = 3000$ G, $\rho^* = |B^*|$, $V_{\rm A}^* \equiv B^*/(\mu_0\rho^*)^{1/2}$, where

μ_0 is the magnetic permeability, $\tau_{\rm A}^* \equiv L^*/V_{\rm A}^*$, and $J^* = B^*/\mu_0 L^*$, respectively. In equation (2.2), ν is a viscosity fixed at 1.0×10^3. The coefficients $c_{\rm h}^2, c_{\rm p}^2$ in equation (2.5) are fixed to the constant values 0.04 and 0.1. The resistivity in equation (2.3) is given as $\eta = \eta_0 + \eta_1 |\boldsymbol{J} \times \boldsymbol{B}||\boldsymbol{v}|^2/|\boldsymbol{B}|^2$, where $\eta_0 = 5.0 \times 10^{-5}$ and $\eta_1 = 1.0 \times 10^{-3}$ in non-dimensional units. As for the choice of these parameters, see Inoue (2016). The second term of the resistivity is introduced to accelerate the relaxation to the force-free state, particularly in regions of weak field.

We use the photospheric magnetic field obtained at 2017 September 4 00:00 UT, 12:00 UT, 18:00 UT, September 5 00:00 UT, 12:00 UT, and September 6 00:00 UT. In Figure 2.1 (a), we indicate the time of each NLFFF calculation with vertical black solid lines. Figure 2.2 shows the 3D coronal magnetic field in (a), the current density obtained from the NLFFF extrapolation in (c) and AIA images in 131 Å and 304 Å, respectively in (b) and (d) at 18:30 UT on September 4. In the figures, the extrapolated field lines match those inferred from the AIA 131 Å image and also the distribution of the current density is in good agreement with the intensity of the AIA 304 Å image. Therefore, we conclude that the NLFFF extrapolation reproduces the observed field lines well.

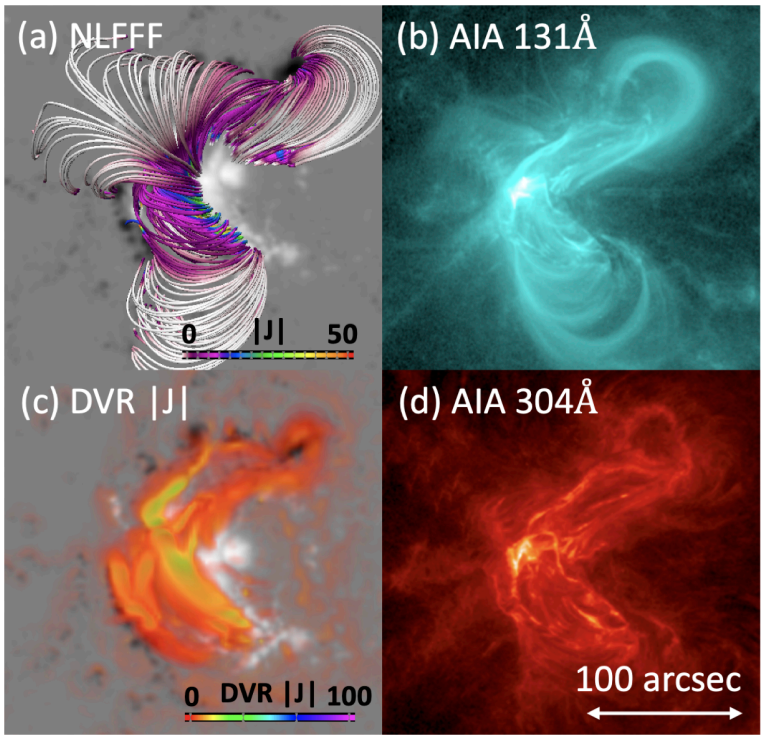

Figure 2.2: (a) Three-dimensional coronal magnetic field strucuture obtained from the NLFFF extrapolation at 18:30 UT on September 4. This time is approximately 2 hours before the M5.5 flare. (b) AIA 131 Å image taken at 18:30 UT on September 4. (c) The electric current distribution calculated from the NLFFF extrapolation at 18:30 UT on September 4. (d) AIA 304 Å image taken at 18:30 UT on September 4.

2.3 Results

2.3.1 Temporal evolution of the NLFFF between September 4 00:00 UT and September 6 00:00 UT

2.3.1.1 Temporal evolution of the photospheric and coronal magnetic fields

We first show the temporal evolution of the photospheric magnetic field in Figures 2.3 (a)-(c) and the MFRs obtained from the NLFFF extrapolations are shown in Figures 2.3 (d)-(f). At September 4 00:00 UT, the highly twisted field lines come up according to the photospheric motion. Furthermore, at 18:00 UT which is approximately 150 minutes before the M5.5 flare peak time, we found an MFR along each of the PILs. In order to identify these three MFRs, we name MFR A, B, and C as indicated in Figure 2.3 (e) and use them in the rest of this paper. MFR A, which exists at the PIL on the west side of the AR, where the X-class flares were observed on September 6 (Liu et al., 2019), was already formed at 18:00 UT September 4. Although the MFRs B and C still exist on September 6, they look to be relaxed compared to those in September 4. Therefore, we suggest that these MFRs are involved in causing the M-class flares.

2.3.1.2 Temporal evolution of the magnetic twist

We employ the magnetic twist, introduced by Berger & Prior (2006), Inoue et al. (2011), and Liu et al. (2016) in this study because it is a convenient value to measure the twist of the field lines in each magnetic field line quantitatively. The magnetic twist is defined as

$$T_{\rm w} = \int_L \frac{\mu_0 \boldsymbol{J}_{\parallel}}{4\pi \boldsymbol{B}} dl = \int_L \frac{\boldsymbol{\nabla} \times \boldsymbol{B} \cdot \boldsymbol{B}}{4\pi B^2}\, dl. \tag{2.6}$$

We calculated the magnetic twist for each field line obtained from the NLFFF.

Figure 2.4 shows the temporal evolution of the magnetic twist mapped on the photosphere. According to the Figures 2.3 and 2.4, the MFRs A and C are characterized by the negative twist, while the MFR B has positive twist. The value of positive twist peaks at 00:00 UT on September 5, after which it seems to decrease. This result indicates that MFR B are formed at the site between the PILs where the MFRs A and C reside.

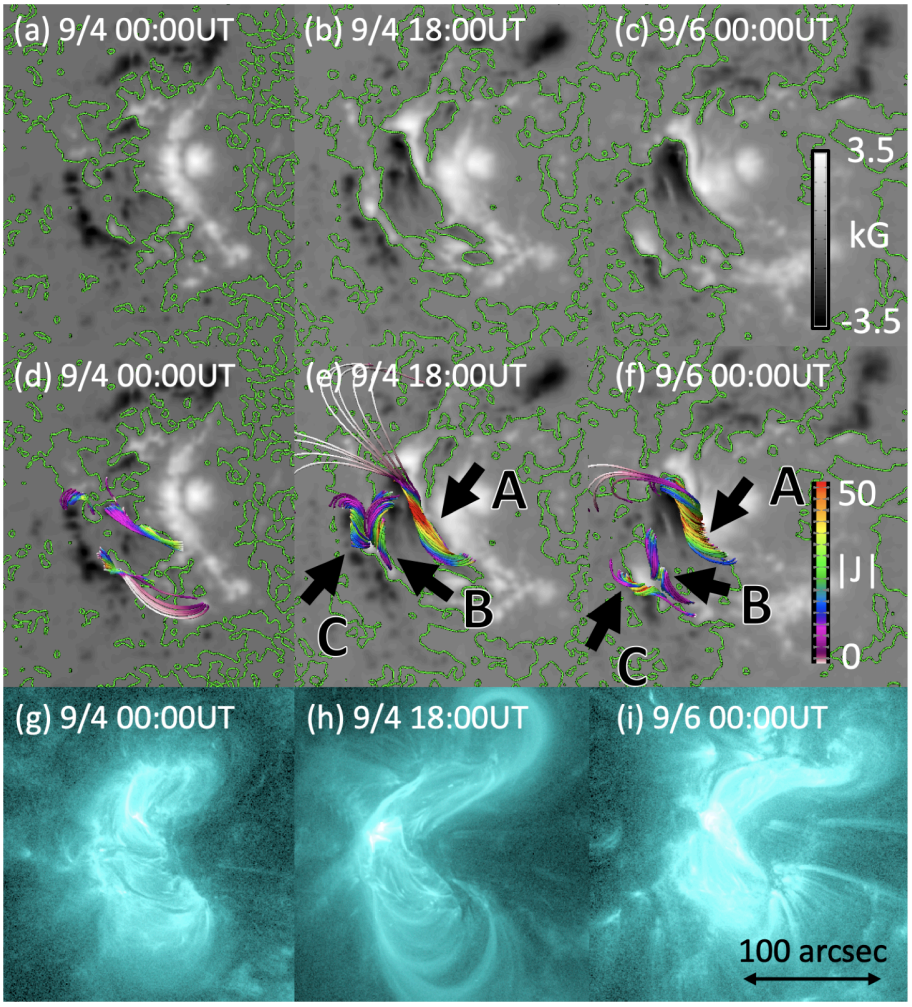

Figure 2.3: Upper panels (a), (b), and (c) show the temporal evolution of the vertical component of the photoshperic magnetic field. Background gray scale and green contour correspond to the vertical magnetic field at the photosphere and PILs, respectively. Middle panels (d), (e), and (f) show the temporal evolution of the MFRs. The color of field lines correspond to the electric current density. Lower panels (g), (h), and (i) shows the EUV 131 Å images observed by the SDO/AIA.

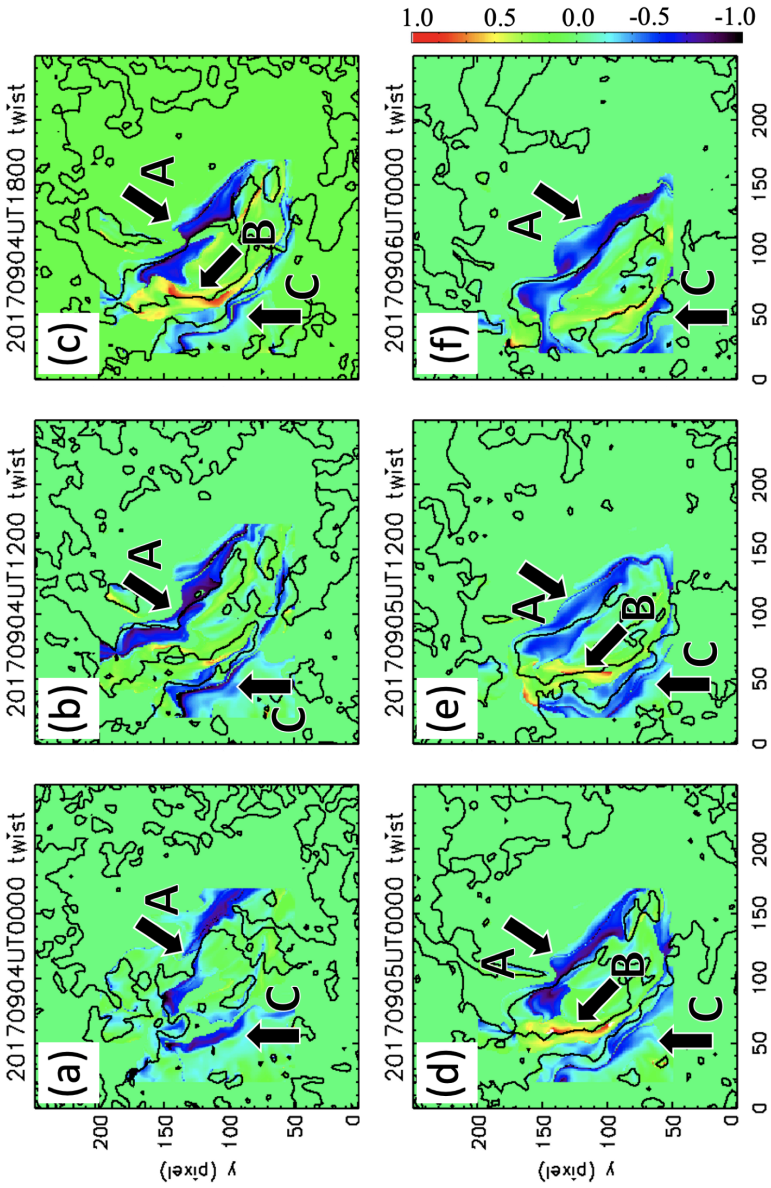

Figure 2.4: Temporal evolution of the magnetic twist of field lines calculated from September 4 00:00 UT to September 6 00:00 UT. Magnetic twist is calculated from each field line and mapped on the photosphere. The color scale represents the amplitude of magnetic twist but the positive and negative colors correspond to left- and right-handed twist. The black lines correspond to the PILs.

To understand the evolution of the magnetic field more quantitatively, we plot the unsigned magnetic flux as follows,

$$F_+(t) = \int_{B_z(t)>0} B_z(t)\, dS, \tag{2.7}$$

$$F_-(t) = \int_{B_z(t)<0} B_z(t)\, dS, \tag{2.8}$$

$$F_{\rm tot}(t) = F_+(t) + |F_-(t)|. \tag{2.9}$$

Figure 2.5 (a) shows the result of the temporal evolution of the flux, F_+, F_-, and $F_{\rm tot}$ respectively. According to the Figure 2.5 (a), both positive and negative magnetic flux increase from September 4 00:00 UT to September 5 00:00 UT and decrease from September 5 12:00 UT to September 6 00:00 UT. These results are consistent with the temporal evolution of the net flux reported by Vemareddy (2019).

Next, we calculated the twist flux, $\tau_\pm$, defined as followings,

$$\tau_+(t) = \int_{T_w(t)>0.35} |B_z(t)| \cdot T_w(t)\, dS, \tag{2.10}$$

$$\tau_-(t) = \int_{T_w(t)<-0.35} |B_z(t)| \cdot T_w(t)\, dS. \tag{2.11}$$

This value is a proxy of strength of a MFR. Figure 2.5 (b) shows the temporal evolution of τ_+ and τ_-. The evolution of τ_- clearly shows a rapid evolution within a day and keeps a high value until September 6. However, although τ_+ also grows within a day, it takes the peak at September 5 00:00 UT, and decreases after that. We also compare the temporal evolution of τ_+ with the $GOES$ soft X-ray profiles in Figure 2.5 (c). The evolution of τ_+ well captures the evolution of the $GOES$ flux as shown in a period from September 4 to 6. In addition, we show the AIA 1600 Å image, the spatial distributions of force-free alpha, and the magnetic twist around 20:30 UT on September 4, when τ_+ increases, in Figures 2.6 (b), (c), and (d), respectively. Here we note that force-free alpha (α) was calculated with the photospheric vector magnetic field obtained with the HMI according to $\alpha = (\nabla \times \boldsymbol{B})_z / B_z$. In the figures, we can clearly see that the sign of force-free alpha and the magnetic twist show the similar distribution. Especially, around the MFR B, both force-free alpha and the magnetic twist have positive sign. Additionally, the enhancement of AIA 1600 Å was observed at the site of the MFR B. These results, from both modeling and observations, suggest that the evolution of the MFR B having the positive twist is closely related to the occurrence of the successive M- and C-class flares.

2.3.1.3 Temporal evolution of the AIA 1600Å observations along each PIL

In this section, we analyze the AIA 1600 Å image to identify the location of the flares. From the GOES plot, we see that 5 flares greater than M2.0-class were observed from

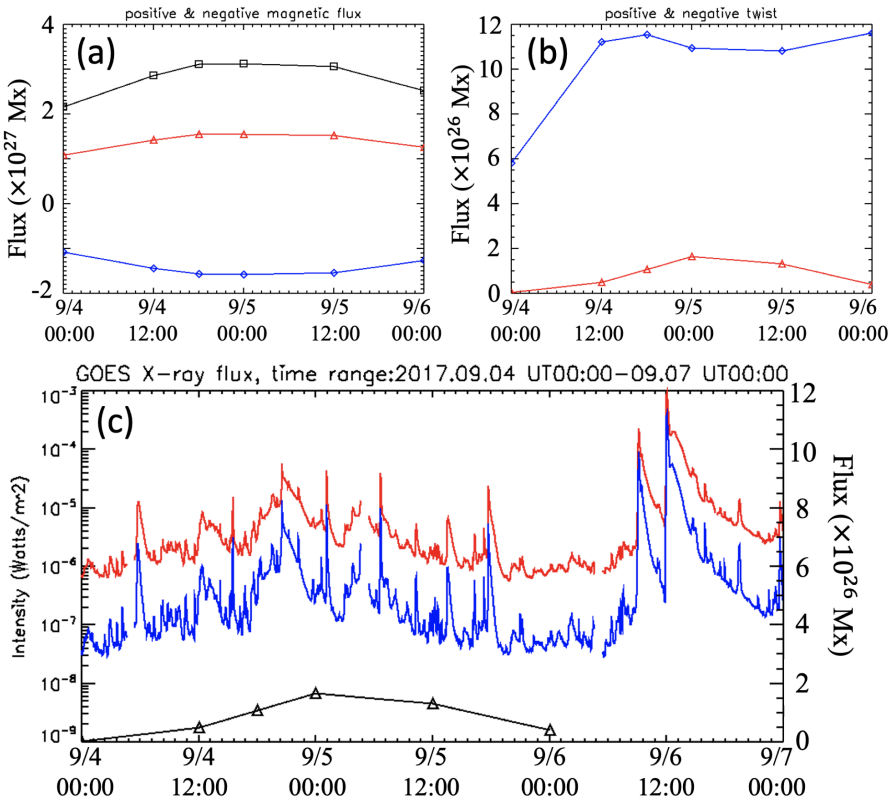

Figure 2.5: (a) Temporal evolution of the magnetic flux in AR 12673. Red, blue, and black symbols represent positive, negative, and total unsigned magnetic flux respectively. (b) Temporal evolution of $\tau_{\pm}$ which are defined in equations (2.10) and (2.11), respectively. τ_{+} and τ_{-} are represented in red and blue, respectively. (c) Temporal evolution of τ_{+} is plotted over the evolution of the *GOES* X-ray flux which is same as Figure 2.1 (a).

September 4 18:00 UT to September 6 00:00 UT. We show the results from three of them: M5.5 flare observed at 20:30 UT September 4, M4.2 flare observed at 01:05 UT September 5, and M2.3 flare observed at 17:40 UT September 5. We divided the flaring region into three areas along three PILs which are surrounded by squares as shown in Figures 2.7 (a), (c), and (e). We measure the intensity of AIA 1600 Å at each box. The results are shown in Figures 2.7 (b), (d), and (f). The first two M-class flares obviously occur on PIL B located in the center, i.e., the MFR B having positive twist would cause these flares. Therefore, we can suggest that the M5.5 flare is mainly driven by the MFR having positive twist. Regarding the last M-flare, the intensity is not only observed at the same PIL but also at the PIL C located in the east. Interestingly, the AIA intensity profile at PIL A located in west was quiet during this period. The MFR residing there produced the successive X-class flares later. This result suggests that the MFR can accumulate the free energy during this period without being interrupted.

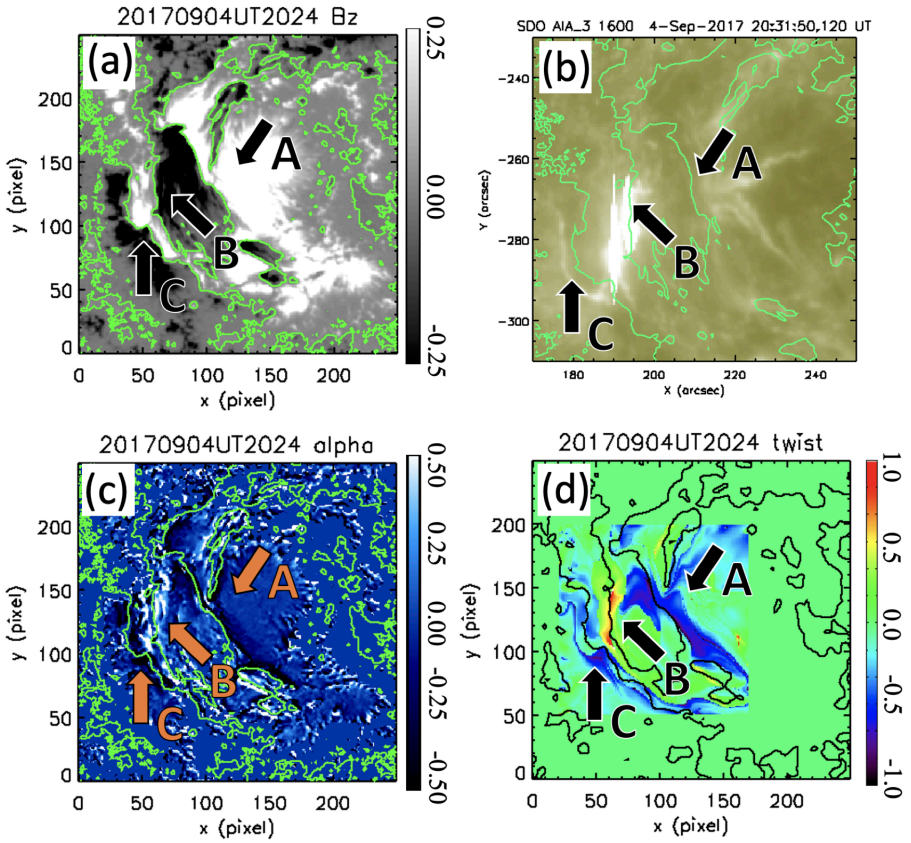

Figure 2.6: (a) Photospheric magnetic field strength at 20:24 UT on September 4, green contour represents the PIL. (b) AIA 1600 Å image at 20:31 UT on September 4 during the M5.5 flare. (c) Distribution of force-free alpha map calculated from the observed vector magnetic field at 20:24 UT on September 4, green contour is same as (a). (d) Spatial distribution of the magnetic twist at 20:24 UT on September 4, black contour represents the PIL.

2.3.2 Magnetic field structure which produced the M5.5 flare

As shown in Figure 2.5 (c), the temporal evolutions of *GOES* X-ray flux and the magnetic flux of the MFR dominated by the positive twist, τ_+, seem to have a good correlation with each other. This result suggests the formation of the MFR B, having positive twist, closely relates to the occurrence of M- and C-class flares. However, the exact trigger mechanism of these flares is not yet clear. Therefore, we investigate the initiation, in particular, focusing on the M5.5 flare which is the largest flare among multiple M-flares observed from September 4 to 6, and also produced a geo-effective CME.

2.3.2.1 Comparison between NLFFF and the AIA 1600 Å image before the M5.5 flare

Figures 2.8 (a) and (b) show the evolution of the flare ribbons observed in the beginning phase of the M5.5 flare. The initial brightenings of the flare observed at 20:30 UT occur at the three locations indicated by red arrows in the white square shown in Figure 2.8 (a). These are enhanced on the both sides of the eastern PIL and central PIL, respectively. However, in the early phase of the flare (at 20:37 UT), the two flare ribbons grow on both side of the center PIL as shown in Figure 2.8 (b). Figure 2.9 (a) shows a close-up of the AIA 1600 Å image at 20:30 UT in which the initial brightenings of the M5.5 flare are found. In Figure 2.9 (b), we traced the field lines from the region where the initial brightenings are enhanced, i.e., these field lines shown in orange are related to the onset of the M5.5 flare. Figure 2.9 (c) shows field lines that form the three MFRs in addition to the field lines shown in Figure 2.9 (b). It is found that the MFRs are covered with the orange lines. For a better understanding of the field configuration, we produced Figure 2.9 (d) in which the field lines are traced only in the $x-z$ plane at $y = 0.5$, and on which the current density $|\boldsymbol{J}|$ is displayed with colors. The regions of enhanced current $|\boldsymbol{J}|$ correspond to the regions where the MFRs exist. We also found that a magnetic null point exists above MFR B.

2.3.2.2 Decay index distribution above the MFRs

We further plot the decay index n, which is a proxy of the torus instability (Kliem & Török, 2006), in Figure 2.10. The decay index n is defined as $n = -(z/|\boldsymbol{B}_{\mathbf{ex}}|)(\partial|\boldsymbol{B}_{\mathbf{ex}}|/\partial z)$ where $\boldsymbol{B}_{\mathbf{ex}}$ denotes the horizontal component of the external field. Here we asume that the external field is the potential field. According to the figure, since the MFRs A and C reside outside of the region that satisfies $n > 1.5$, we suggest that these MFRs are stable to the torus instability. However, MFR B is located in the region where the decay index n is larger than 1.5.

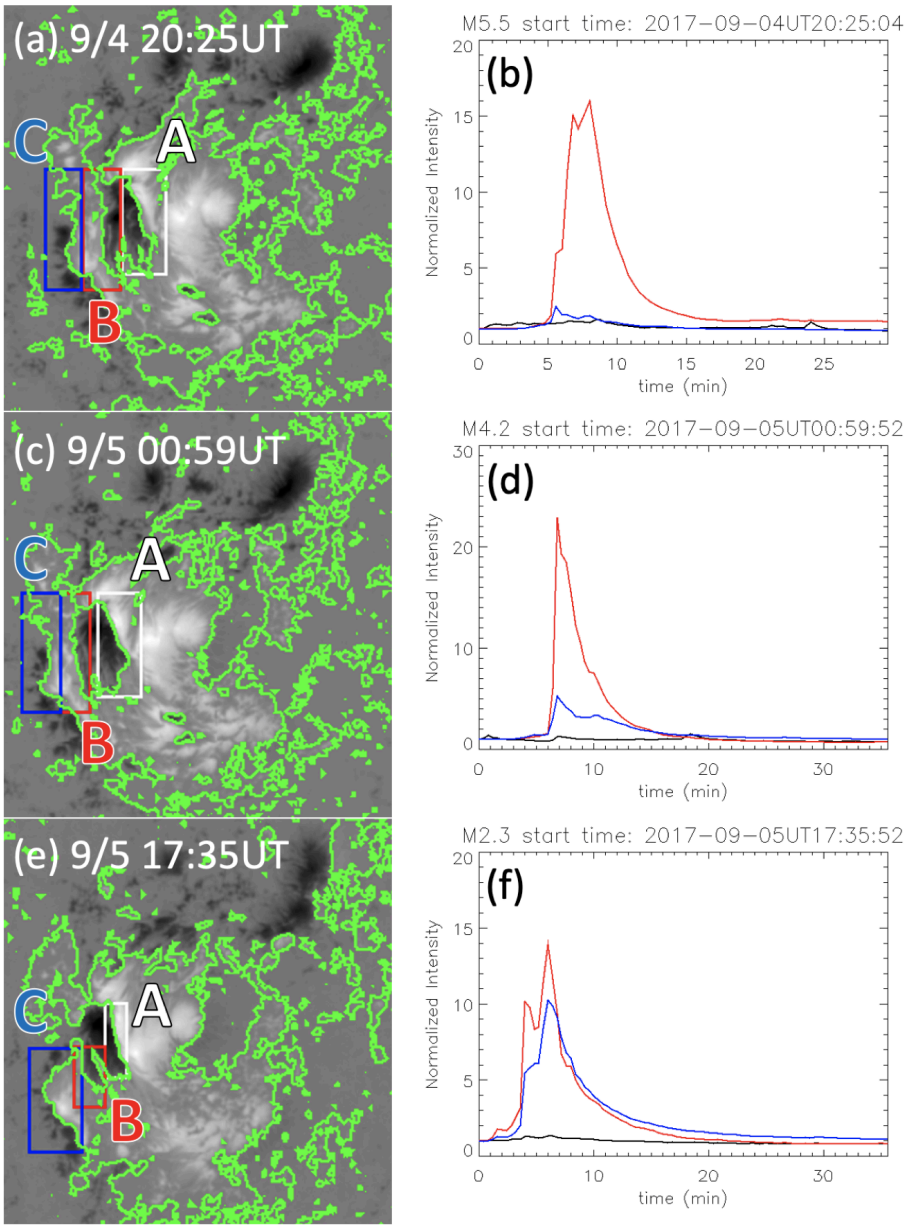

Figure 2.7: Left three panels (a), (c), and (e) show the HMI magnetic field strength in grayscale, and PILs with green lines. These are observed at 04:24 UT September 4, 01:00 UT, and 17:36 UT September 5, respectively. Right three panels (b), (d), and (f) show the temporal evolution of intensity of the AIA 1600 Å, which is integrated in each box normalized by the intensity at the start time during the solar flares. Each red, blue, and black line is calculated in each integration area in red , blue, and white box respectively, shown in left panels.

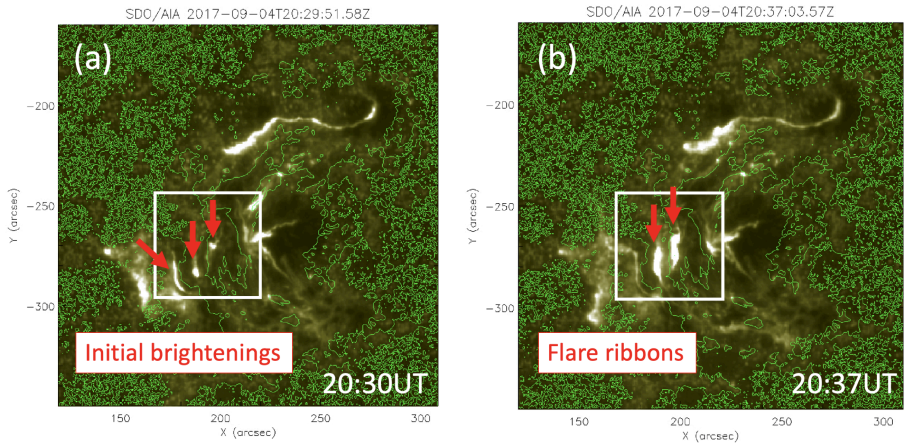

Figure 2.8: (a) AIA 1600 Å image when the M5.5 flare started at September 4 20:30 UT where the green lines correspond to the PILs. (b) Flare ribbons of M5.5 flare observed at September 4 20:37 UT in AIA 1600 Å image.

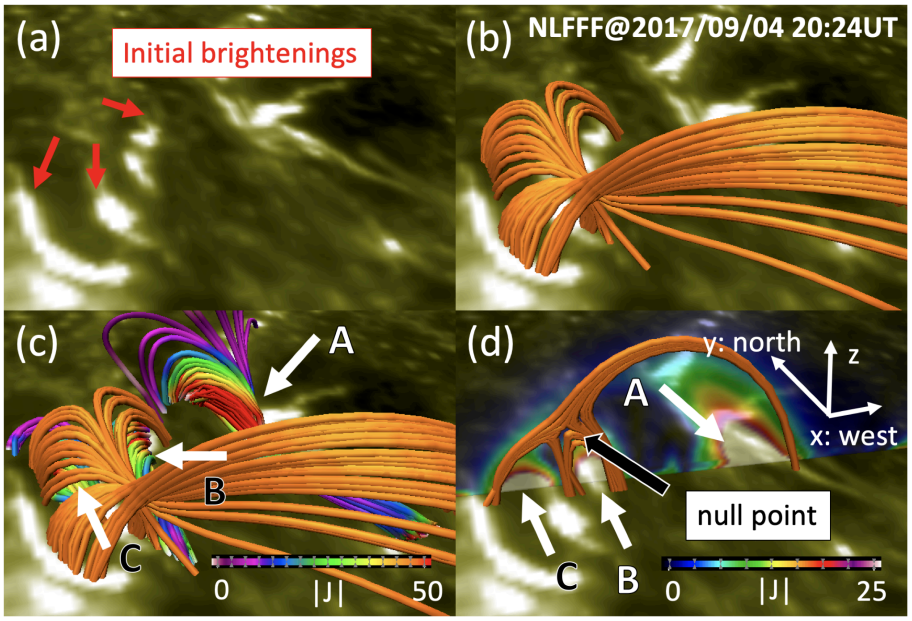

Figure 2.9: (a) AIA 1600 Å image at the beginning of the M5.5 flare. Red arrows indicate the brightening associated with initiation of the M5.5 flare. (b) The field lines obtained from the NLFFF extrapolation using the HMI data at 20:24 UT on September 4, are traced from the three brightening regions indicated by arrows shown in (a). (c) Three MFRs plotted together with the field lines shown in (b). (d) The field lines surrounding the MFRs, which correspond to those shown in (b), and they are traced in $x - z$ plane where $y = 0.5$. The distribution of electric current density in the same plane.

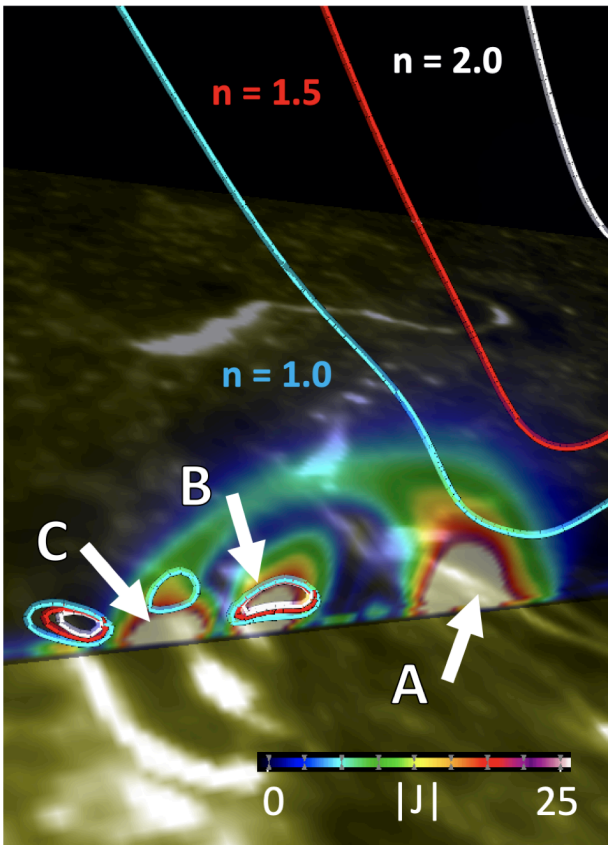

Figure 2.10: The contour of the decay index, $n = 1.0$, 1.5, and 2.0 are shown in blue, red, and white, respectively on the $x - z$ plane at $y = 0.5$, on which the distribution of electric current density is displayed. The electrical current distrubution is the same as in Figure 2.9.

2.4 Discussion & Summary

In this study, in order to clarify the evolution of the 3D magnetic field and flare activities observed in AR 12673, we analyzed the temporal evolution of the 3D magnetic field structure based on the time series of the NLFFFs from September 4 00:00 UT to 6 00:00 UT. We calculated the magnetic twist from each NLFFF, and consequently, found that three MFRs are formed above three PILs in parallel before the M5.5 flare, observed at 18:30 UT on September 4. Interestingly one MFR (MFR B) locating in the center has positive helicity while the other two (MFRs A and C) have negative helicity. From our detailed analysis, the evolution of the magnetic flux of MFR B has a good correlation with the $GOES$ flux evolution while the M- and C-class flares were observed. Therefore, we suggest that these flares were driven by the formation of the MFR B. We further analyzed the 3D magnetic structure in vicinity of the three MFRs. We found a magnetic null above MFR B at 20:24 UT on September 4. Vemareddy (2019) also reported that a magnetic null was formed in a similar location at 18:30 UT on September 4. Since the AIA 1600 Å image shows intensity enhancements in the beginning of the M5.5 flare where the footpoints of the magnetic field lines including magnetic null are anchored, we suggest that null point reconnection possibly helps to accelerate the MFR B. Furthermore, as shown in Figure 2.10, we found that MFR B would be unstable to the torus instability. Inoue et al. (2018a) showed that MFRs can be accelerated even in an isolated area where the decay index n has high value to drive the instability. Therefore, in this case, the torus instability possibly pushed the MFR B and enhanced the reconnection at the magnetic null. Namely, the interaction between the torus instability and reconnection might be important driving the eruption.

Figure 2.11 schematically describes a scenario for the M5.5 flare obtained from our study. When the positive twisted MFR B is formed at the site between the MFRs A and C, it pushes the pre-existing magnetic field upward which drives the reconnection at the null point. The null point reconnection is able to remove the magnetic field surrounding the MFR B, consequently, the MFR B can easily escape from the lower corona resulting in the eruption. However, reconnected field lines would suppress the instabilityof neighboring MFRs A and C. Therefore, only MFR B would escape from the lower corona.

However, we confirmed that the AIA 1600 Å brightening is relatively weak above the PIL located on the west side of the AR, compared to those located in the middle and east side. The MFR A located above the PIL in west causes successive X-class flares on September 6 (Hou et al., 2018; Inoue et al., 2018b; Mitra et al., 2018). Therefore, we suggest that MFR A can accumulate the enough free magnetic energy to produce the X-flares as a result of photospheric motions without being disturbed. In addition, at the west-side PIL the intruding motion of the negative peninsula toward the neighboring positive was observed before the X2.2 flare (Bamba et al., 2020). Taking into account our results, this intrusion

would be important to break the equilibrium of the MFR A, resulting in triggering the X-flares.

According to our study, we suggest that not only the properties of the MFRs but also the 3D magnetic topology overlying the MFR is important to understand the onset of solar flares. Therefore, we consider that this information should be taken into account when considering future flare prediction schemes.

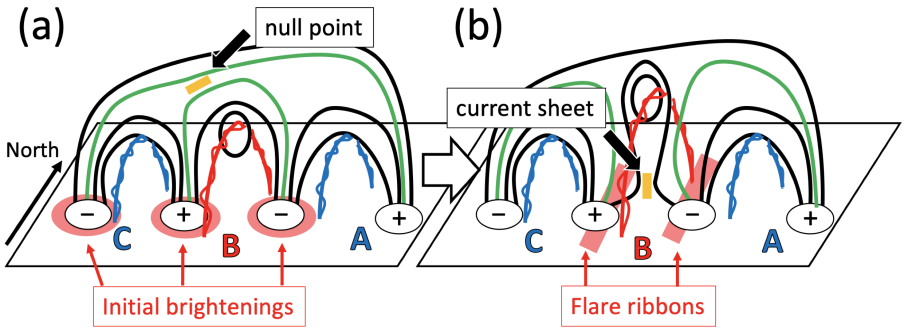

Figure 2.11: The schematic of the magnetic field structure before and after the M5.5 flare. Red and blue twisted lines represent the MFRs A, B, and C. The red and blue represent the sign of the helicity where the red and blue correspond to positive and negative, respectively. Green lines show the coronal magnetic field lines, which experience the reconnection at the magnetic null point in the early phase of M5.5 flare. Yellow line shows the current sheet. Red arrows in (a) indicate the location of initial brightenings, and those in (b) indicate the location of the flare ribbons.

CHAPTER 3

A Data-constrained Magnetohydrodynamic Simulation of the X1.0 Solar Flare of 2021 October 28

In Chapter 2, we investigated the formation process of MFRs and the relation between MFR formation and the onset of flares in the flare-productive AR. In this chapter, we focus on AR NOAA 12887, and we extend the comprehension of the dynamics of MFRs into erupting phase by using an approach of data-based magnetohydrodynamic simulation.

3.1 Introduction

As introduced in Section 1.2, solar flares are the rapid energy release phenomena in solar atmosphere (Priest & Forbes, 2002). The energy source of solar flares is widely considered as magnetic energy accumlated in solar active regions (ARs; Toriumi & Wang, 2019). Some of the free magnetic energy are converted into kinetic energy of erupting plasmas through magnetic reconnection (Coppi & Friedland, 1971; Spicer, 1982; Shibata & Magara, 2011). These erupting plasmas are often observed as filament eruptions in the Hα line (Parenti, 2014; Seki et al., 2017, 2019). Solar filaments are cool and dense plasma compared to the surrounding plasma, they are widely considered to be supported by helical coronal magnetic field structure, magnetic flux ropes (MFRs; see Section 1.3; Xu et al., 2012; Hanaoka & Sakurai, 2017; Gibson, 2018).

Chintzoglou et al. (2019) proposed that emerging dipole flux become strongly sheared due to photospheric motion and result in the formation of a bundle of helical magnetic field lines. Yan et al. (2016) presented an observation that magnetic reconnection between pre-existing sheared magnetic arcades forms MFRs. This process is consistent with the tether-

cutting reconnection scenario by Moore et al. (2001) and the flux-cancellation model by van Ballegooijen & Martens (1989). In solar eruptions, several triggering processes are proposed, for instance, the MHD instability such as the kink instability (Fan & Gibson, 2003; Török & Kliem, 2004) and double-arc instability (Ishiguro & Kusano, 2017; Kusano et al., 2020), or magnetic reconnection (Moore et al., 2001; Antiochos et al., 1999). To accelerate the solar eruption, the torus instability (Kliem & Török, 2006) plays an important role.

As introduced in Section 1.3, to understand the initiation of MFR eruptions, three-dimensional (3D) coronal magnetic field provides crucial information because the free magnetic energy is released in the solar corona and topology of the coronal magnetic field changes associated with a flare. Observational limitation cannot allow us for direct observation of coronal magnetic field, and we need to extrapolate them by using a numerical technique such as potential field and nonlinear force-free field (NLFFF) modeling (Wiegelmann & Sakurai, 2012; Inoue, 2016). There are several studies using a time series of NLFFF to reveal the formation process of MFRs (Su et al., 2009; Savcheva & van Ballegooijen, 2009; Inoue et al., 2013; Kang et al., 2016; Kawabata et al., 2017; Muhamad et al., 2018; Yamasaki et al., 2021). However, NLFFF is assumed as an equilibirum state only considering Lorentz force balance, and we cannot discuss dynamical evolutions of 3D magnetic field during eruptive phase of flares. Since a data-constrained magnetohydrodynamic (MHD) simulation show time evolving MHD processes of the coronal magnetic field that are free from a force-free condition, we can extend our understanding to the dynamics of an erupting precess. Some of the previous studies on the data-constrained MHD simulations successfully produced the eruptions that are driven by a reconnection or instability and these results are in good agreement with observations (Jiang et al., 2013; Inoue et al., 2015, 2018b; He et al., 2020; Inoue & Bamba, 2021). Therefore, the data-based MHD simulation is helpful to understand dynamics of the coronal magnetic field in a realistic magnetic environment.

In this study, in order to understand the initiation and dynamics of the MFR eruption associated with X1.0 flare on October 28 2021, we performed a data-constrained MHD simulation using a NLFFF as the initial condition. The NLFFF is extrapolated with observed photospheric vector magnetic field at 14:00 UT October 28, which is 1.5 hours before the onset of the flare. The rest of this paper is structured as follows: the observations and methods of analysis are described in Sections 3.2 and 3.3, results are presented in Section 3.4, discussions on the eruption mechanism of the MFR are shown in Section 3.5, and our conclusions are summarised in Section 3.6.

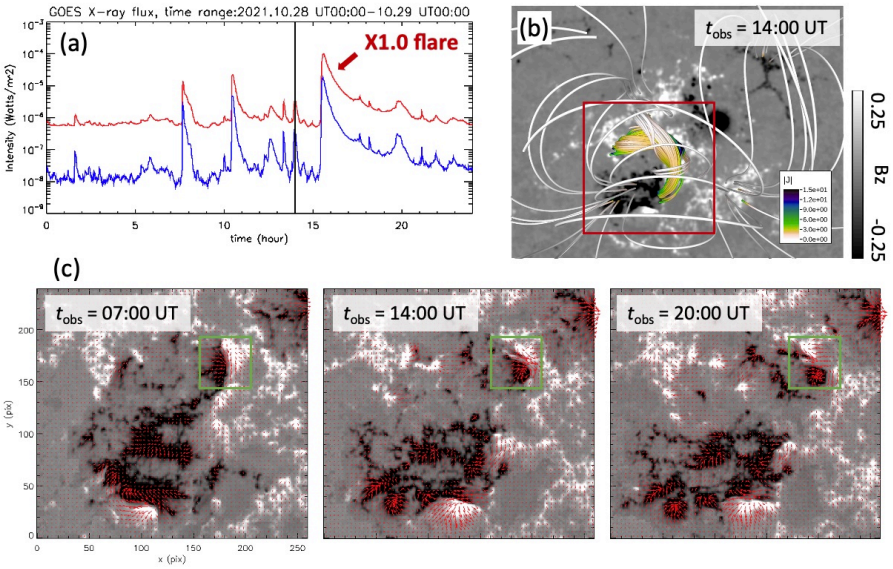

Figure 3.1: The 2021 October 28 flare in GOES soft X-ray lightcurves and HMI vector magnetograms. (a) Soft X-ray fluxes from the $GOES$ 13 satellite in the $1 - 8$Å (red) and $0.5 - 4.0$Å (blue) passband. The vertical black line shows the time of the initial condition set for the present simulation. (b) Radial component of the photospheric magnetic field in the AR 12887 at 14:00 UT on October 28. Color of the field lines represent the electric current density. (c) Temporal evolution of the photospheric vector magnetic field. Gray-scaled background and red arrows show the radial and horizontal component of the magnetic field, respectively. (An animation of the HMI photospheric magnetic field images is available. The duration of the animation is 4 seconds and it provides information of the temporal evolution of the photospheric vector magnetic field including an intruding motion of a negative patch into a positive patch from 00:00 UT to 23:48 UT 2021 October 28.)

3.2 Observation

The GOES class X1.0 flare occurred on 2021 October 28 in NOAA active region (AR) 12887. According to the *GOES* X-ray lightcurves in Figure 3.1 (a), the onset time was 15:17 UT and the soft X-ray flux reached its maximum at 15:35 UT. The black solid line at 14:00 UT indicates the time that we selected for calculating the bottom boundary to be used for the MHD simulation. Figure 3.1 (b) shows the radial magnetogram and the coronal magnetic field lines extrapolated with NLFFF around the AR 12887 at 14:00 UT. The photospheric vector magnetic field data are taken by the Helioseismic and Magnetic Imager (HMI; Scherrer et al., 2012) onboard the *Solar Dynamics Observatory* (*SDO*; Pesnell et al., 2012). The vector magnetograms which we use have been released as the Spaceweather HMI Active Region Patch (SHARP; Bobra et al., 2014) data series (hmi.sharp_cea_720s series). Details of the vector magnetic field data reduction and other related information about HMI data products can be found in Hoeksema et al. (2014) and Bobra et al. (2014). In Figure 3.1 (c), we show the temporal evolution of the photospheric vector magnetic field in the region of interest, which is the same as the region indicated by the red box in Figure 3.1 (b). Background grayscale and the red arrows show the radial and the horizontal component of the magnetic field, respectively. According to Figure 3.1 (c), we can find an intruding motion of the negative polarity towards the positive polarity on October 28 in the region indicated by the green box in the panels.

Figure 3.2 (a-c) show the temporal evolution of the Hα (6562.8 Å) images observed with the Global Oscillation Network Group (GONG; Harvey et al., 1996) around the AR 12887 during the X1.0 flare. Details of the instrument can be found in Harvey & GONG Instrument Team (1995). Figure 3.2 (d-i) show the temporal evolution of the 304 Å images observed by the Atmospheric Imaging Assembly (AIA; Lemen et al., 2012) on board the *SDO* during the X1.0 flare. Green and blue lines in panels (d-f) indicate the contours of 250 and -250 G of radial component of the photospheric magnetic fields observed by HMI, respectively. We can find the J-shaped dark filament in the early phase of the flare (Figure 3.2 (a,d,g)) and the erupting filament and the X-shaped flare ribbons in the main flare phase (Figure 3.2 (b,e,h)). The Hα flare ribbons last until the later phase of the flare (Figure 3.2 (c)). The post flare arcades can be seen in the 304 Å images (Figure 3.2 (f,i)).

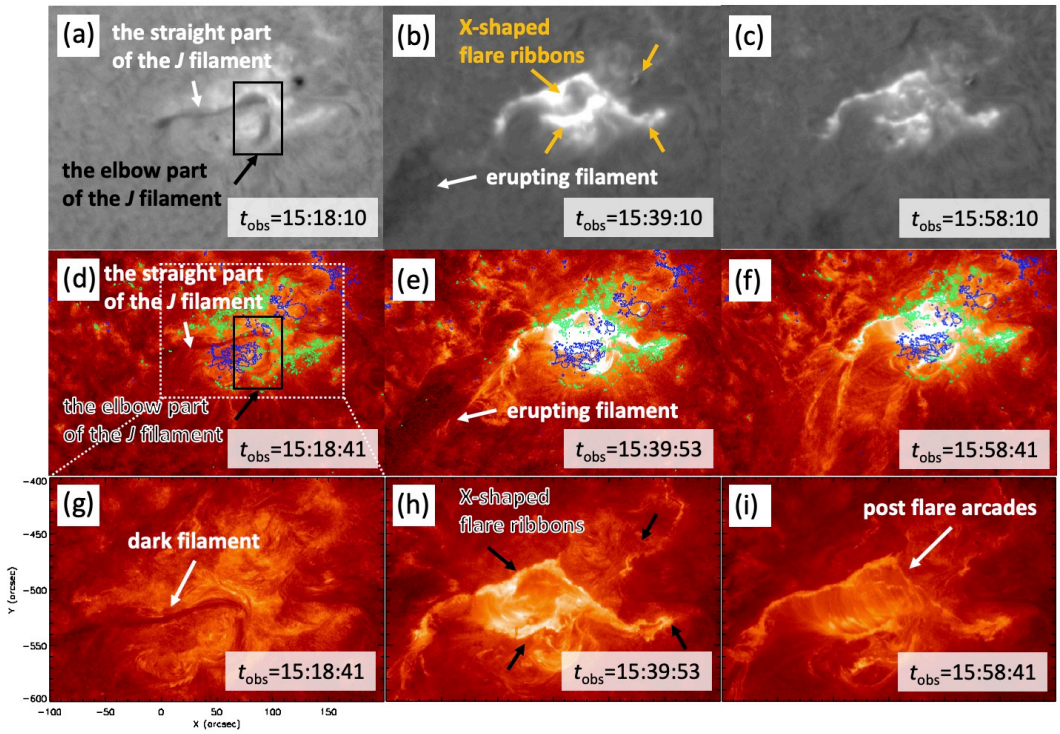

Figure 3.2: Temporal evolution of AR 12887 during the 2021 October 28 flare. (a-c) Hα (6562.8 Å) observation with GONG shows the flare ribbons and a dark filament that later erupts. (d-i) SDO/AIA 304 Å images show the flare loops, the erupting filament, and post-flare arcades. Green and blue lines in panels (d-f) indicate the contours of 250 and -250 G of radial component of the photospheric magnetic fields, respectively. (An animation of the AIA 304 images is available. The duration of the animation is 5 seconds and it provides information on the temporal evolution of dark filament eruption, flare enhacements, and post flare arcades from 15:00 UT to 16:00 UT 2021 October 28.)

3.3 Methods

We construct a nonlinear force-free field and then use it as the initial condition for the data-constrained MHD simulation. Once the 3D magnetic field is obtained, we calculate the magnetic twist number and the decay index to study the instability leading to eruption.

3.3.1 Nonlinear Force-Free Field Extrapolation

In order to perform the NLFFF extrapolation, we first calculate the potential field (Sakurai, 1982) which is used as the initial condition of the MHD relaxation (Inoue et al., 2014b; Inoue, 2016). We solve zero-beta MHD equations to obtain the force-free field because the gas pressure and gravity are neglected approximately compare to the magnetic pressure in the solar corona (Gary, 2001). We solve the following MHD equations,

$$\rho = |\boldsymbol{B}|, \tag{3.1}$$

$$\frac{\partial \boldsymbol{v}}{\partial t} = -(\boldsymbol{v}\cdot\boldsymbol{\nabla})\boldsymbol{v} + \frac{1}{\rho}\boldsymbol{J}\times\boldsymbol{B} + \nu_i\boldsymbol{\nabla}^2\boldsymbol{v}, \tag{3.2}$$

$$\frac{\partial \boldsymbol{B}}{\partial t} = \boldsymbol{\nabla}\times(\boldsymbol{v}\times\boldsymbol{B} - \eta_i\boldsymbol{J}) - \boldsymbol{\nabla}\phi, \tag{3.3}$$

$$\boldsymbol{J} = \boldsymbol{\nabla}\times\boldsymbol{B}, \tag{3.4}$$

$$\frac{\partial \phi}{\partial t} + c_{\rm h}^2\boldsymbol{\nabla}\cdot\boldsymbol{B} = -\frac{c_{\rm h}^2}{c_{\rm p}^2}\phi, \tag{3.5}$$

where the subscript i of ν and η corresponds to different values used in NLFFF and MHD. ρ, $\boldsymbol{B}$, $\boldsymbol{v}$, $\boldsymbol{J}$, and ϕ are plasma pesudo-density, magnetic flux density, velocity, electric current density, and a conventional potential to reduce errors derived from $\boldsymbol{\nabla}\cdot\boldsymbol{B}$ (Dedner et al., 2002). The pseudo-density in equation (3.1) is assumed to be proportional to $|\boldsymbol{B}|$. In these equations, the length, magnetic field, density, velocity, time, and electric current density are normalized by $L^* = 254.8$ Mm, $B^* = 3000$ G, $\rho^* = |B^*|$, $V_{\rm A}^* \equiv B^*/(\mu_0\rho^*)^{1/2}$, where μ_0 is the magnetic permeability, $\tau_{\rm A}^* \equiv L^*/V_{\rm A}^*$, and $J^* = B^*/\mu_0 L^*$, respectively. In equation (3.2), $\nu_{\rm NLFFF}$ is a viscosity fixed at 1.0×10^3. The coefficients $c_{\rm h}^2, c_{\rm p}^2$ in equation (3.5) are fixed to the constant values 0.04 and 0.1. The resistivity in equation (3.3) is given as $\eta_{\rm NLFFF} = \eta_0 + \eta_1|\boldsymbol{J}\times\boldsymbol{B}||\boldsymbol{v}|^2/|\boldsymbol{B}|^2$, where $\eta_0 = 5.0\times10^{-5}$ and $\eta_1 = 1.0\times10^{-3}$ in non-dimensional units. As for the boundary conditions, three components of the magnetic field are fixed at each boundary, while the velocity is fixed to zero and the von Neumann condition $\partial/\partial n = 0$ is imposed on ϕ during the iteration. Here we note that we fixed the bottom boundary according to

$$\boldsymbol{B}_{\mathbf{bc}} = \gamma\boldsymbol{B}_{\mathbf{obs}} + (1-\gamma)\boldsymbol{B}_{\mathbf{pot}}, \tag{3.6}$$

where $\boldsymbol{B}_{\mathbf{bc}}$ is the transversal component determined by a linear combination of the observed magnetic field ($\boldsymbol{B}_{\rm obs}$) and the potential magnetic field ($\boldsymbol{B}_{\mathbf{pot}}$). γ is a coefficient

in the range of 0 to 1. The value of the parameter γ is increased to $\gamma = \gamma + d\gamma$ if $R = \int |\boldsymbol{J} \times \boldsymbol{B}|^2 dV$, which is integrated over the computational domain, becomes smaller than a critical value which is denoted by $R_{\rm min}$ during the iteration. In this paper, we set $R_{\rm min}$ and $d\gamma$ the values of 5.0×10^{-3} and 0.02, respectively. When γ reaches to 1, $\boldsymbol{B_{bc}}$ is completely consistent with the observed data. Furthermore, we controll the velocity as follows. If the value of $v^*(= |\boldsymbol{v}|/|\boldsymbol{v_A}|)$ is larger than $v_{\rm max}$ (here we set to 0.04), then we modify the velocity from $\boldsymbol{v}$ to $(v_{\rm max}/v^*)\boldsymbol{v}$. We adopted these processes because they would help avoid a sudden jump from the boundary into the domain during the iterations.

3.3.2 Data-constrained MHD Simulation

Next we performed the MHD simulation using NLFFF as an initial condition. We name this simulation RUN A. The equations we solve are identical to those in the NLFFF extrapolation. However, the handling of the bottom boundary condition is different between the NLFFF extrapolation and the data-constrained simulation. In the data-constrained simulation, the bottom $B_{\rm x}$ and $B_{\rm y}$ follow an induction equation while the normal component is fixed with time. Although the boundary magnetic field evolve with time in a physically consistent manner, these evolutions are inconsistent with the observations (Inoue & Bamba, 2021). We set resistivity and viscosity as $\eta_{\rm MHD} = 1.0 \times 10^{-4}$ and $\nu_{\rm MHD} = 1.0 \times 10^{-3}$, respectively, which are different from those in the NLFFF. The coefficients $c_{\rm h}^2$ and $c_{\rm p}^2$ in equation (3.5) are fixed to the constant values 0.04 and 0.1, respectively.

For both calculations, the numerical domain has dimensions of $255 \times 195 \times 191$ Mm^3, or $1.00 \times 0.77 \times 0.75$ in non-dimensional units. The region is devided into $352 \times 270 \times 264$ grid points.

3.3.3 Analysis of Magnetic Fields

Once the 3D magnetic field is obtained, we calculate the magnetic twist number and the decay index to study the instability leading to eruption. The magnetic twist of each field line ($e.g.$ Inoue et al., 2011; Liu et al., 2016, etc.) is calculated using the following definition (Berger & Prior, 2006),

$$T_{\rm w} = \int_L \frac{\boldsymbol{\nabla} \times \boldsymbol{B} \cdot \boldsymbol{B}}{4\pi B^2}\, dl, \tag{3.7}$$

where dl is a line element. The decay index, n, the proxy criterion for the torus instability (Kliem & Török, 2006) is calculated as

$$n = -\frac{z}{|\boldsymbol{B_{ex}}|}\frac{\partial |\boldsymbol{B_{ex}}|}{\partial z} \tag{3.8}$$

Here $\boldsymbol{B}_{\mathbf{ex}}$ denotes the horizontal component of the external field, which is assumed to be the potential field in this study.

3.4 Results

3.4.1 Evolution of the MFR

In Figure 3.3, we display three snapshots of the MHD simulation to show temporal evolution of the coronal magnetic field. Figure 3.3 (a) and (d) show the initial condition of the simulation viewed in two different perspective angles. Figure 3.3 (b,e) and (c,f) show the magnetic field structure at 4.26 and $t = 10.2$ at the same angle as above, respectively. The colored field lines are selected in the criteria of strong twist built up during the evolution. For this purpose, we first calculated the magnetic twist of every field line starting from each pixel using equation (7), which yields a map of magnetic twist on the bottom boundary. We then select the regions with $T_{\mathrm{w}} > 1.0$ at the final time step ($t = 10.2$) of the simulation from which we perform the field line tracing. P1, P2, and P3 correspond to the footpoints of the pink, green, and yellow field lines in the regions of positive magnetic polarity, and N1, N2, N3 are their counterparts in the negative polarity. In our NLFFF, only the elbow part of the J-shaped dark filament located at the west side of the AR (Figure 3.2 (a)) could be well reconstructed by the yellow field lines in Figure 3.3. We think that this is because the straight part of the J-shaped filament formed at the east side of the AR was located above the relatively weak field region and failed to build a highly twisted structure. We define a bundle of field lines with $T_{\mathrm{w}} > 1.0$ as an MFR and that with $0 < T_{\mathrm{w}} < 1.0$ as a sheared magnetic arcade. In this definition, the yellow lines are identified with an MFR, and pink and green lines, a pair of sheared magnetic arcades at the initial time. In Figure 3.3 (c,f), we can see the MFR (yellow lines) undergo eruption and expansion. We suggest that the continuous magnetic reconnection taking place between the pink and green field lines led to the formation of magnetic loops below the MFR, see the online animation.

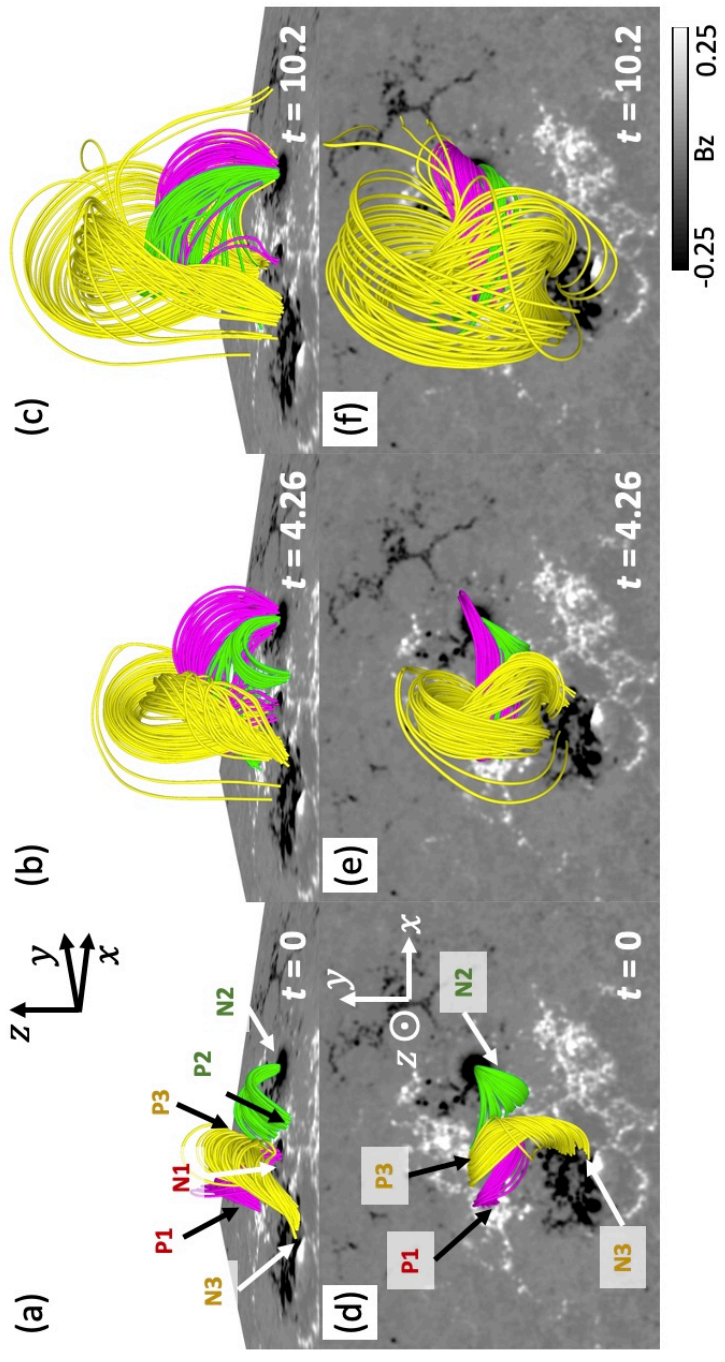

Figure 3.3: Three snapshots of the simulation of RUN A, showing temporal evolution of the coronal magnetic fields. (a) and (d) show top and side views of the 3D magnetic fields at $t = 0$. (b) and (e) show those at $t = 4.26$. (c) and (f) show those at $t = 10.2$. The pink, green, and yellow lines are the field lines with footpoints at P1-N1, P2-N2, and P3-N3, respectively. The yellow lines are identified as an MFR that erupts. (An animation of the RUN A simulation is available. The duration of the animation is 1 second and it provides information on the temporal evolution of the 3D magnetic field in our RUN A simulation including the MFR eruption and magnetic reconnection between pre-existing sheared magnetic arcades.)

3.4.2 Decay index distribution

In Figure 3.4 we plot the height distribution of the decay index calculated using equation (8) on a vertical $x-z$ plane at $y = 0.34$. Figure 3.4 (a) shows that the MFR (yellow lines) was already located in the region of high decay index $n > 2.0$ at the start. In panels (b) and (c), we plot, in azure color, the potential magnetic field lines surrounding the MFR in 3D and 2D, respectively. A magnetic null like region ($B \approx 0$) is found on the plane at a low latitude $z = 0.09$ (Figure 3.4 (c,d)). Since magnetic field rapidly decreases toward the null, a large value of the decay index was realized in the low latitude (Figure 3.4 (d)). We, therefore, expect that the MFR (yellow lines) could easily become unstable to the torus instability. In addition, as shown in panel (d), we find a torus stable region with $n < 1.3$ above the initial location of the MFR ($0.09 < z < 0.46$). Kliem et al. (2021) pointed out that in the case of such cubic functional decay index distribution, an eruption starts but fails because of torus stable region. However, some numerical studies reported that the MFRs could erupt if they were located at the torus unstable region in the initial condition (Inoue et al., 2018a; Zhong et al., 2021; Joshi et al., 2021). In such a case, even if the decay index above the MFRs is low enough to be torus stable, the MFRs could erupt. Our result supports the latter scenario.

3.4.3 Comparison of the flare ribbon structures of observation and simulation

Figure 3.5 shows the flare ribbons observed in Hα and EUV (a-c) and calculated from the MHD model (d) in the main phase of the flare. The Hα and EUV images show bright ribbons not only at two footpoints of the MFR (P3 and N3), but also at other four footpoints of sheared magnetic arcades formed below the MFR (P1, P2, N1, and N2) (Figure 3.5 (a-c)). The model flare ribbon (red features in Figure 3.5 (d)) is calculated simply based on the distance between two footpoints of a field line per pixel. Since the only way that this length changes significantly is via reconnection, we regard those regions as ribbons. Specifically those pixels where field lines with the distance changing by more than 3.6 Mm are marked red. These computed flare ribbons are found not only at the footpoints of the MFR, but also at the four footpoints of sheared magnetic arcades consistent with the observation. This result supports the scenario of the reconnection between two sheared magnetic arcades below the pre-existing MFR during the X1.0 flare.

Although the computed flare ribbons in the northern part of the AR fairly well agree with the observed ribbons in both location and intensity, those in the southern part of the AR do not. The observed ribbon in the location of $-540'' < y < -530''$ is barely predicted by the model, while the observed ribbon in $-560'' < y < -550''$ is very weak compared with the model prediction. We consider two possibilities for the partial success of our

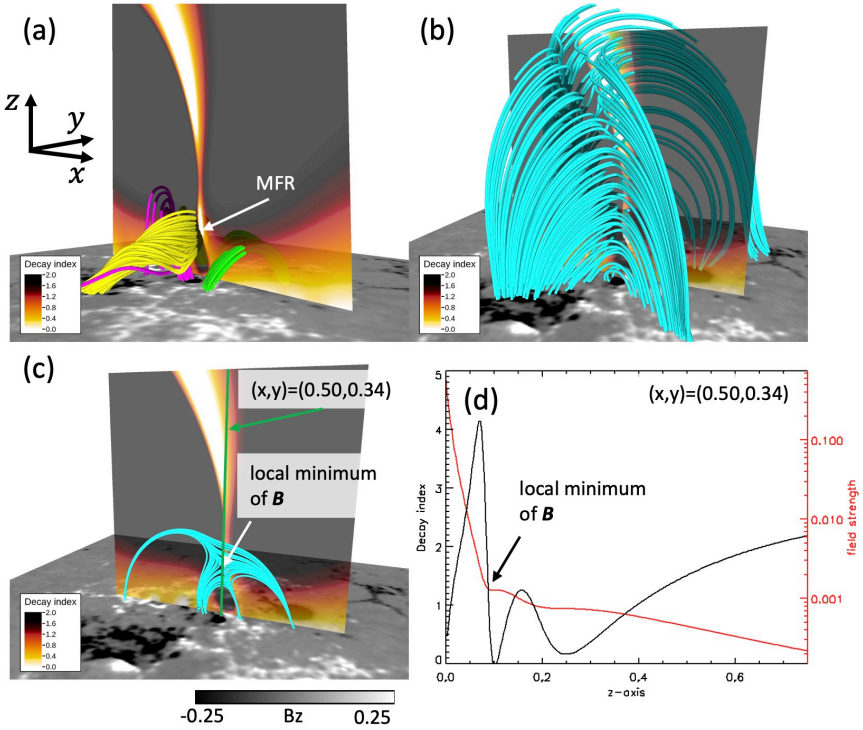

Figure 3.4: Decay index distribution in 3D. (a) The index is plotted in vertical cross section of x–z plane at $y = 0.34$. The initial magnetic field lines ($t = 0$) in the simulation are plotted with the same color convention as used in Figure 3 (b). (b) Azure lines are the potential field lines surrounding the MFR. (c) The field lines of the potential field are projected on the x–z plane at $y = 0.34$. The green line is the vertical line of $(x, y) = (0.50, 0.34)$ selected for plotting 1D distribution of the decay index and the magnetic field strength in (d).

ribbon prediction. One is that our model prediction for flare ribbons is designed mainly for location but not intensity, and our criterion for ribbons based on the field line length change does not work well for the southern ribbons. The other possibility is that the topology of the magnetic field in the southern area is not correctly reproduced under the NLFFF extrapolation to limit the accuracy of our ribbon prediction in that area.

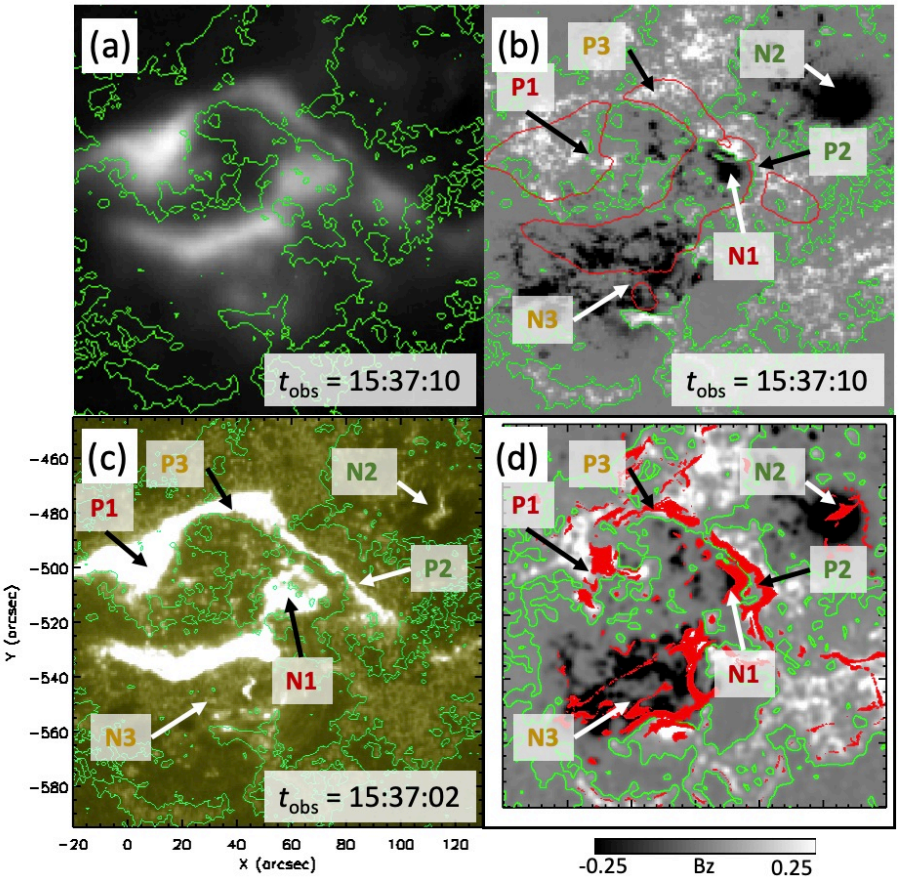

Figure 3.5: Observed and computed flare ribbons. Green lines in all the panels show the polarity inversion lines. (a) Flare ribbons in the GONG Hα line image at 15:37:10 UT. (b) The radial component of the photospheric magnetic field overlaid with the enhanced Hα intensity as red contours at 15:37:10 UT. (c) Flare ribbons in the AIA 1600 Å channel at 15:37:02 UT. (d) The computed flare ribbons from the MHD simulation of RUN A (red) plotted over the magnetogram (grayscale).

3.5 Discussion

The results of simulation RUN A indicate two possibilities for the driving mechanism of the MFR eruption. One is the torus instability of the MFR (Figure 3.4). According to the result of the statistical study of an eruption mechanism done by Jing et al. (2018), the decay index value of $n > 2.0$ is large enough to produce eruptions via torus instability. The other possibility is that the MFR is pushed upward by the magnetic loops formed by the magnetic reconnection between two sheared magnetic arcades below the pre-existing MFR (Figure 3.3). This process can also drive the MFR eruption. The newly formed loops are created through the reconnection, therefore it can be interpreted that the reconnection drives the MFR eruption.

In order to find out which process is essential for the eruption of the MFR, we conduct another MHD simulation named RUN B. To clarify what role is played by the reconnection under the erupting filament, we halt the motion in the specific region where strong current density is formed; it lies between the sheared field lines in pink and green (see orange box in Figure 3.6 (b)). This process is expected to partially suppress the magnetic reconnection between two sheared magnetic arcades. We thus prevent in this experiment, the large loops from forming that is suspected to push the erupting MFR.

In Figure 3.6, we compare the field lines found in simulation RUN A with those in RUN B. The same color code is used for both. The results of RUN B show how the field line structure differs when the reconnection between pink and green lines is suppressed. However, the MFR with yellow lines moved upwards in RUN B as well as in RUN A (Figure 3.6 (a,b)). Therefore, the MFR can ascend without being pushed up by the large arcade.

Figure 3.7 compares simulation RUN B with RUN A in terms of the vertical velocity (V_z) and normalized current density, $|\boldsymbol{J}|/|\boldsymbol{B}|$. The distribution of V_z in an x-z plane is plotted at $y = 0.34$ at a time in the early phase, $t = 0.85$, for both simulations. RUN A shows that the enhanced upward V_z extends down to a lower height than in RUN B (Figure 3.7 (a,b)). In RUN A, the MFR and the newly formed magnetic loops exist in the region of enhanced velocity, whereas, in RUN B, the velocity is enhanced only in the location of the MFR. The height-variation of V_z plotted in Figure 3.7 (c) clearly shows that the velocity is much more enhanced when the reconnection between the sheared field lines is allowed.

In a region of strongly enhanced $|\boldsymbol{J}|/|\boldsymbol{B}|$, the magnetic field topology may change rapidly and thus it could be a boundary between two topologically different regions. For instance, the region indicated by the white arrow in Figure 3.7 (d,e) can indicate a boundary between the MFR and the overlying field lines, thus roughly the edge of the MFR. In Figure 3.7 (f), we show the one-dimensional plot of $|\boldsymbol{J}|/|\boldsymbol{B}|$. The edge of the MFR in RUN A is higher than that in RUN B, while V_z of RUN A is still larger than that of RUN B. These results

suggest that the MFR could erupt even without being pushed by the magnetic loops newly formed below the MFR. However, the push-up from below can be important to help the acceleration of the MFR. And according to the results of the observed and the computed flare ribbons, they were observed not only at the two footpoints of the erupting MFR but also at the four footpoints of the reconnecting pre-existing magnetic arcades, the scenario of RUN A is more consistent with the observation rather than RUN B.

As shown in Figure 3.6, observation supports the scenario with magnetic reconnection between pink and green field lines. By comparing the photospheric magnetic field structure before and after the X1.0 flare, intruding motion of the negative polarity (N1 in Figure 3.5) into the positive polarity (P2 in Figure 3.5) was observed at the location where we found the magnetic reconnection in RUN A (see the green box of Figure 3.1 (c)). Inoue & Bamba (2021) pointed out that the intruding motion can be a trigger of magnetic reconnection concerning to the MFR eruption. We suggest that the intruding motion we found in this case of X1.0 flare could be a trigger of the magnetic reconnection.

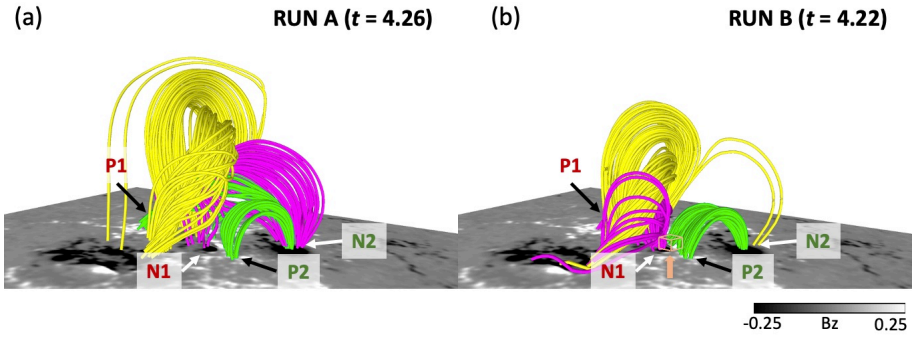

Figure 3.6: Comparison of magnetic fields in RUN A and RUN B. The magnetic fields at $t = 4.26$ in RUN A (a) and those at $t = 4.22$ in RUN B (b). The same color convention as in Figure 3 is used to identify the three groups of field lines. Orange box indicated by orange arrow in (b) shows the region where we set the velocity to zero in RUN B. It lies in $0.45 \leq x \leq 0.54$, $0.31 \leq y \leq 0.40$, and $0.02 \leq z \leq 0.06$, satisfying $|\boldsymbol{J}| \geq 10$.

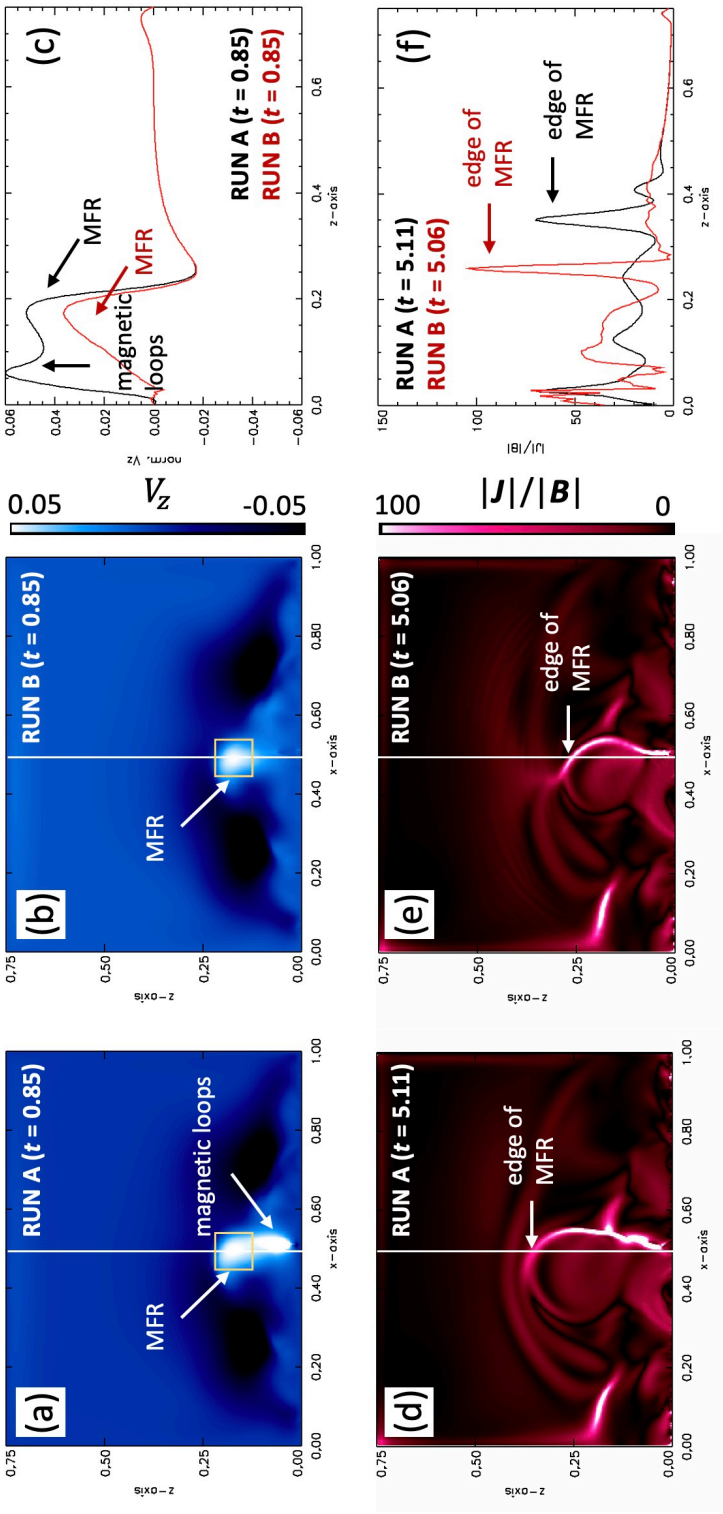

Figure 3.7: Comparison of RUN A and RUN B in terms of the vertical velocity, V_z (a–c) and current density normalized by magnetic field, $|\boldsymbol{J}|/|\boldsymbol{B}|$ (d–f). (a,b) show 2D distribution of V_z in a vertical $x-z$ plane at $y = 0.34$, obtained from RUN A and RUN B at $t = 0.85$, respectively. (c) shows their 1D distributions at the location of $(x, y) = (0.50, 0.34)$ indicated by the white line marked in other panels. Likewise, (d, e) show the 2D distribution, and (f), the 1D distribution of $|\boldsymbol{J}|/|\boldsymbol{B}|$ obtained from RUN A at $t = 5.11$ and RUN B at $t = 5.06$, respectively. Regions of enhanced $|\boldsymbol{J}|/|\boldsymbol{B}|$ are regarded as edges of the MFR.

3.6 Conclusion

We presented a data-constrained MHD simulation to understand the formation and erupting process of an MFR associated with the X1.0 flare that occurred on 2021 October 28, which is characterized by an X-shaped flare ribbon and a nearly circular J-shaped filament. Our simulation is meant to reproduce the observed MFR eruption with the shape of the filament and the ribbons as constraint. According to the initial condition obtained from a nonlinear force-free field extrapolation, the MFR was initially in a region of sufficient decay index. Therefore the MFR could erupt under the torus instability alone. However, we found that the magnetic reconnection between two sheared magnetic arcades took place under the pre-existing MFR during the erupting phase of the MFR, and paid attention to the possible role of this reconnection of the underlying loops in facilitating the eruption of the MFR.

By performing an experimental simulation in which this reconnection is suppressed, we found that the MFR is still able to erupt but at a reduced speed. The MFR erupts faster when the large magnetic loops form underneath. The reconnection of the magnetic loops formed below the MFR is thus essential for accelerating the MFR. In addition, this reconnection cannot be overlooked because flare ribbons were observed not only at the footpoints of MFR but also at those of the newly formed magnetic loops during the filament eruption. From these results, we propose that the initial driving mechanism of the filament eruption associated with this GOES X1.0 flare was facilitated by the combined action of the torus instability and the formation of the magnetic loops through the reconnection below the pre-existing MFR. A similar idea was presented by Inoue et al. (2018b).

This event produced a strong CME which has been well studied in many papers (Xu et al., 2022; Hou et al., 2022; Papaioannou et al., 2022; Li et al., 2022). It is thus of new interest how this MFR grows into the CME, although the present simulation domain is not large enough to fully trace the MFR in a long range. It is also worthwhile to investigate how the pre-erupting MFR is formed. We plan to address these issues in future with an extended time coverage.

CHAPTER 4

Magnetic Field of Solar Dark Filaments Obtained from He I 10830 Å Spectro-polarimetric Observation

In Chapters 2 and 3, by using numerical approaches such as nonlinear force-free field modeling and magnetohydrodynamic simulation, we investigated the dynamics of the evolution of the magnetic field of MFRs. In this chapter, we perform direct observation of the magnetic field of solar dark filaments which are the cool and dense plasmas suspended by MFRs. We discuss not only the estimated field strength but also the magnetic field configuration of the observed filaments.

4.1 Introduction

As we presented in Section 1.4, solar dark filaments (or prominences seen on the solar limb) are cool ($\sim 10^4$ K) and dense ($> 10^9$ cm^{-3}) plasma suspended in the hot ($> 10^6$ K) corona. They are supported by a bundle of twisted coronal magnetic field or magnetic flux ropes (MFRs: Xu et al., 2012; Gibson, 2018). Some of the dark filaments are located in quiet region, and some are in active region. The former filaments are often called as quiescent (QS) filaments, and the latter are called as active region (AR) filaments. Both of the QS and AR filaments locate above the polarity inversion lines (PILs: Babcock & Babcock, 1955). The filaments sometimes become unstable and erupt into the interplanetary space, and solar flares are simultaneously observed (Priest & Forbes, 2002). A unified model of filament eruptions and solar flares are reviewed in Shibata & Magara (2011). The eruptive solar flares are sometimes accompanied by the coronal mass ejections (CMEs), and the filaments are observed as a core structure of the CMEs (Parenti, 2014).

As introduced in Section 1.3, to understand the formation process and the evolution of MFRs in ARs, a number of authors investigated the three-dimentional (3D) coronal magnetic field by using an extrapolation of the nonlinear force-free field (NLFFF: Inoue et al., 2013; Kang et al., 2016; Kawabata et al., 2017; Muhamad et al., 2018; Yamasaki et al., 2021). In some cases, the NLFFF are used for initial conditions to investigate the dynamics of the erupting MFRs with a magnetohydrodynamic simulation (Jiang et al., 2013; Inoue et al., 2015, 2018; Inoue & Bamba, 2021; Yamasaki et al., 2022a). However, the NLFFF approximation is not necessarily valid for the lower layer of the solar atmosphere such as the photosphere or low chromosphere. This is because the magnetic pressure is not sufficiently higher than the gas pressure at these heights (Gary, 2001), $i.e.$, the assumption of the force-free is not valid. Kawabata et al. (2020) reported that the shear angle ($i.e.$, angle from the potential field) of the horizontal magnetic field at the height of chromosphere reproduced with the NLFFF was smaller than that determined from observations. Yelles Chaouche et al. (2012) performed two NLFFF extrapolations using observed photospheric and chromospheric magnetic field in dark filament regions independently, and by comparing the results of these two extrapolations they found that the difference in magnetic field structure that supports the filament plasmas; they found highly twisted field lines with more than one turn in the extrapolation from photosphere, but they only found less twisted field lines in the extrapolation from chromosphere. This result suggests that the NLFFF only using a photospheric magnetogram is not suitable for reconstructing filaments' magnetic field. Thus, direct observations of the magnetic field of the dark filaments are important to understand the structure and the mechanism of instability of the dark filaments.

In Table 4.1, we summarized the previous results on the magnetic field of dark filaments and prominences from spectro-polarimetric observations. Regarding QS filaments, most of the studies suggest that the field strength is of the order of 10 Gauss (Leroy et al., 1983, 1984; Bommier et al., 1986, 1994; Casini et al., 2003; Orozco Suárez et al., 2014; Martínez González et al., 2015). Wang et al. (2020) reported the field strength of an erupting QS filament was smaller than 100 Gauss. Regarding AR filaments, some of the previous studies suggest that the field strength is $100 - 800$ Gauss (Xu et al., 2012; Kuckein et al., 2009; Sasso et al., 2011, 2014). However, Díaz Baso et al. (2016) pointed out that the observed Stokes profiles from the AR filaments can be explained with a field strength of 10 Gauss in the filament if contaminations of observed spectra by the radiation from the background active region with 600 Gauss.

Besides the field strength of QS and AR filaments, two types of the magnetic field configuration of the filaments are proposed. One is the normal polarity model (Kippenhahn & Schlüter, 1957). In this model, the shear direction of the magnetic field of the filaments is the same as the shear direction of the ambient magnetic field inferred from the photo-

spheric magnetic field (see Figure 4.1 (a), (c), and (d)). The other model is the reverse polarity model (Kuperus & Raadu, 1974). In this model, the shear direction of the magnetic field of the filaments is opposite to the shear direction of the ambient magnetic field (see Figure 4.1 (b), (d), and (e)). For QS filaments, Bommier & Leroy (1998) performed a spectro-polarimetric observation of an off-limb prominence in He I D3 line and found that the magnetic field structure was reverse polarity (see also Bommier et al., 1994). Martínez González et al. (2015) performed a spectro-polarimetric observation of an off-limb prominence in He I 10830 Å, and they also reported that the structure was the reverse polarity. Wang et al. (2020) obtained the vector magnetic field of an erupting filament and reported that the magnetic field structure was reverse polarity during the eruption process. For AR filaments, Xu et al. (2012) suggested that the magnetic field structure was normal polarity by using a simultaneous observation of He I 10830 Å and Si I 10827 Å lines. Sasso et al. (2014) analyzed the vector magnetic field of filament and concluded that the magnetic field topology was reverse polarity configuration. Yokoyama et al. (2019) studied the photospheric vector magnetic field in a filament channel and suggested that the field configuration was reverse polarity.

Diagnostics of the magnetic field structure of the solar filaments require vector magnetic field information. Spectro-polarimetric observation of the absorption line of the He I 10830 Å is one of the most powerful methods to quantitatively obtain the magnetic field of the solar filaments (Hanaoka & Sakurai, 2017). This line is sensitive to magnetic field not only through the Zeeman effect (Zeeman, 1897) but also through the Hanle effect (Hanle, 1924). From the Zeeman effect in this line, the longitudinal components of 10 Gauss and transverse components of 200 Gauss are detectable at a sensitivity of 0.03% in polarimetric measurements. In contrast, the Hanle effect diagnostics allow us to deduce relatively weak field of $0.1 - 100$ Gauss. In this study, to clarify not only the magnetic field strength of the filaments but also the magnetic field configuration, we performed a spectro-polarimetirc observation in He I 10830 Å line targeting dark filaments located in quiet regions.

The rest of this paper is structured as follows; the observation is introduced in Section 4.2, the analysis is described in Section 4.3, results are presented in Section 4.4, discussions on our findings are given in Section 4.5, and the summary of this study is in Section 4.6.

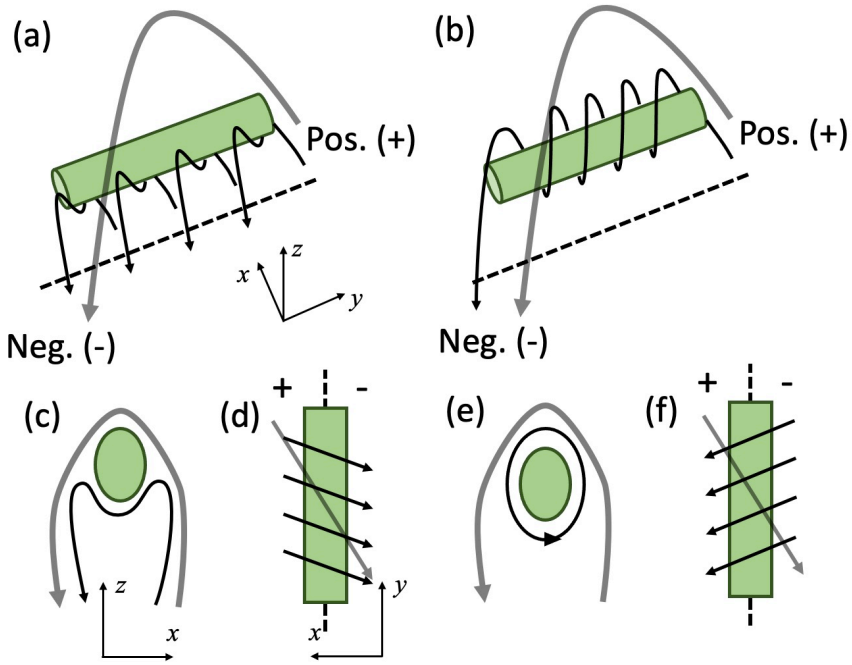

Figure 4.1: Cartoons of two types of prominence models. Green cylinder, black solid lines, gray line, black bashed lines represent the prominence plasmas, magnetic field lines of a filament, a global magnetic field, and polarity inversion line, respectively. (a) Normal polarity model in 3-dimensional view, (b) Reverse polarity model in 3D view, (c) cross section in x-z plane of normal polarity model, (d) cross section in x-y plane of normal polarity model, (e) cross section in x-z plane of reverse polarity model, (f) cross section in x-y plane of reverse polarity model. Here z-axis is the normal to the solar surface and y-axis is along the magnetic neutral line.

Table 4.1: Past observational works on filament(/prominence) magnetic field

Paper	Filament type	Field strength [Gauss]	Normal pol. (K-S model)	Reverse pol. (K-R model)
Wang et al. (2020)	QS	< 100	-	○
Casini et al. (2003)	QS	$10 - 70$	-	-
Orozco Suárez et al. (2014)	QS	~ 25	-	-
Martínez González et al. (2015)	QS	< 20	-	○
Bommier et al. (1986)	QS	$2 - 20$	-	-
Leroy et al. (1984)	QS	$5 - 10$	-	-
Bommier et al. (1994)	QS	7.5	-	○
Leroy et al. (1983)	QS	6 [1]	-	-
Bommier & Leroy (1998)	QS	-	-	○
Xu et al. (2012)	AR	$600 - 800$	○	-
Kuckein et al. (2009)	AR	< 500	-	-
Sasso et al. (2011)	AR	$100 - 250$	-	-
Sasso et al. (2014)	AR	~ 100	-	○
Díaz Baso et al. (2016)	AR	~ 10	-	-
Yokoyama et al. (2019)	AR	-	-	○ [2]

[1] Their target was a polar crown.

[2] By photospheric magnetic field observation below dark filaments.

4.2 Observation

Observation was performed by using the newly installed spectro-polarimeter on the Domeless Solar Telescope (DST: Nakai & Hattori, 1985) at Hida Observatory (Ichimoto et al., 2022). The polarimeter consisting of a rotating super achromatic waveplate and a polarizing beam splitter is located just behind the slit of the spectrograph, and it provides efficient modulations for two orthogonally polarized spectra on detectors in wavelength range of $5000 - 11000$ Å. In our observation in He I 10830 Å, polarimetric sensitivity of 3×10^{-4} was achieved in a few second with a near-infrared (NIR) camera, the Goldeye G033 SWIR (640×512 pixels), (Yamasaki et al., 2022c, see).

Using the spectro-polarimeter, we performed the observations of 8 dark filaments (DFs) on 2022 Apr 9, 2022 Jun 4, 2022 Aug 11, and 2022 Aug 24 JST (see Table 4.2). Hereafter, we use filament IDs shown in Table 4.2 to identify each of the target filaments. He I 10830 Å and Si I 10827 Å lines were taken with the NIR camera with an exposure time of 15 msec for each frame. We obtained 200 frames in 3 sec for each slit position with 1.0 Hz modulation by the rotating waveplate. The slit width and length were 0.1 and 20 mm, corresponding to $0''.64$ and $128''$ on the solar image, respectively. Spatial sampling along the slit is $0''.43$ pixel^{-1}, and the spectral sampling is 29 mÅ pixel^{-1} while scan step was $1''.38$. Fields-of-view along the slit direction (X) and the scan direction (Y) for each observation is given in Table 4.2.

The 8 observational targets are indicated on the full disk Hα solar images taken by the Solar Dynamics Doppler Imager (SDDI: Ichimoto et al., 2017) on the Solar Magnetic Activity Research Telescope (SMART: UeNo et al., 2004) in Figures 4.2, 4.3, 4.4, and 4.5 (a). In addition, we also show full disk images of the photospheric magnetic field taken by the Helioseismic and Magnetic Imager (HMI: Scherrer et al., 2012) onboard the *Solar Dynamics Observatory* (*SDO*: Pesnell et al., 2012) in Figures 4.2, 4.3, 4.4, and 4.5 (b). From the photospheric magnetogram and the Hα images, we identified that the DF1, DF3, and DF7 locate in plage regions, the DF2, DF4, DF5, and DF6 locate in quiet regions, and the DF8 locate near an active region.

Geometrical height of the target filaments is an important parameter for a correct evaluation of the magnetic field by using the Hanle effect. In our study, we estimated the heights of the targets using the SMART-SDDI images days prior or posterior to the DST spectro-polarimetric observation at which they were off-limb prominences. The adopted heights for each filament are shown in Table 4.2.

Table 4.2: Observational targets

ID	Observation date	Scan time in UT (start-end)	Position [1] r	p	i	X [2] [″]	Y [2] [″]	Height [″]
DF1 [3]	2022 Apr 8	23:34:41-23:42:36	11’ 16”	95° 23’	76° 30’	128	166	25
DF2	2022 Apr 9	00:37:28-00:45:23	13’ 31”	11° 47’	39° 36’	128	166	17
DF3 [3]	2022 Apr 9	01:40:53-01:48:48	10’ 28”	78° 58’	39° 25’	128	166	21
DF4	2022 Apr 9	02:15:46-02:29:00	13’ 27”	219° 48’	39° 10’	128	276	23
DF5	2022 Apr 9	03:02:31-03:09:06	6’ 35”	327° 57’	326° 04’	128	138	29
DF6	2022 Jun 4	05:42:41-05:49:16	9’ 34”	204° 30’	50° 16’	128	138	18
DF7 [3]	2022 Aug 11	06:25:28-06:35:22	11’ 34”	302° 50’	343° 43’	128	207	15
DF8 [4]	2022 Aug 24	00:57:59-01:04:34	9’ 30”	359° 27’	10° 41’	128	138	19

[1] The position parameters of r, p, and i represent the heliocentric distance, polar angle measured from the geographic north, and inclination angle of the slit of spectrograph from the geographical N-S direction, respectively.

[2] X is the field view along the slit common for all the targets and Y is the scanning range.

[3] Targets locate above plage regions (see Figure 4.2 for DF1 and DF3 and Figure 4.4 for DF8).

[4] One footpoint of the filament is connected to an active region (see Figure 4.5).

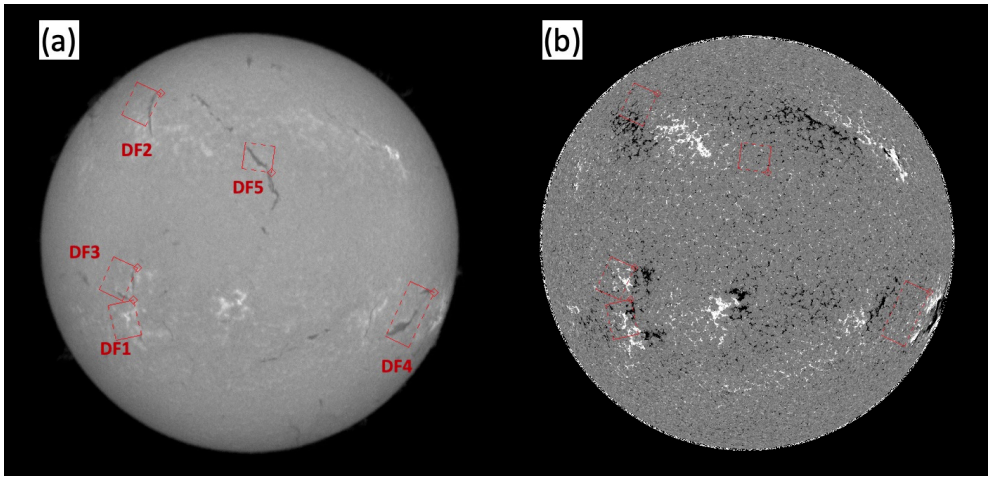

Figure 4.2: Location of the observational targets taken on 2022 Apr 9. (a) Hα line center image taken by the SMART-SDDI. (b) Photospheric magnetogram taken with SDO-HMI. Greyscale show the radial component of the magnetic field. White and black correspond to the field strength of -50 and 50 Gauss, respectively. Red line rectangles show the field-of-view of the target DF regions. Solid and dashed lines represent slit and scan directions, respectively. Diamond symbol represents the origion of the field of view.

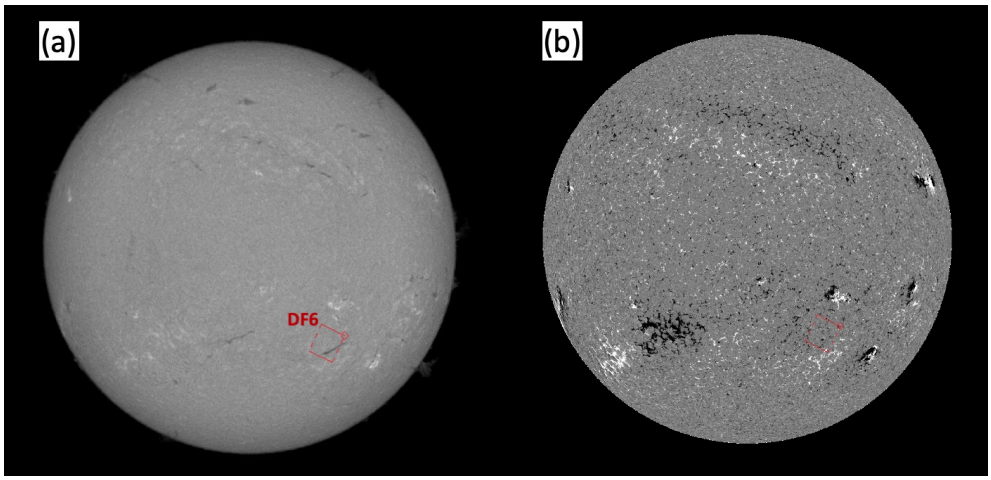

Figure 4.3: Location of the observational targets taken on 2022 Jun 4. Format of this figure is same as that of Figure 4.2.

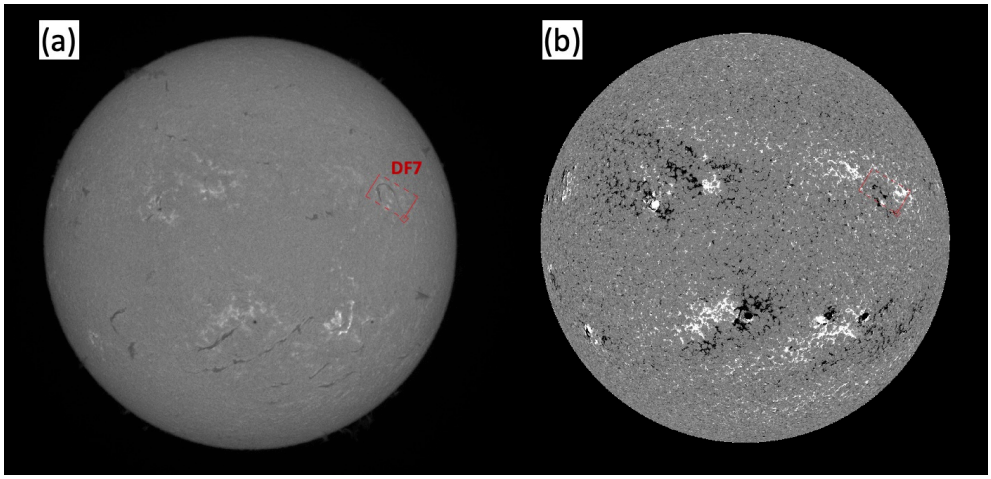

Figure 4.4: Location of the observational targets taken on 2022 Aug 11. Format of this figure is same as that of Figure 4.2.

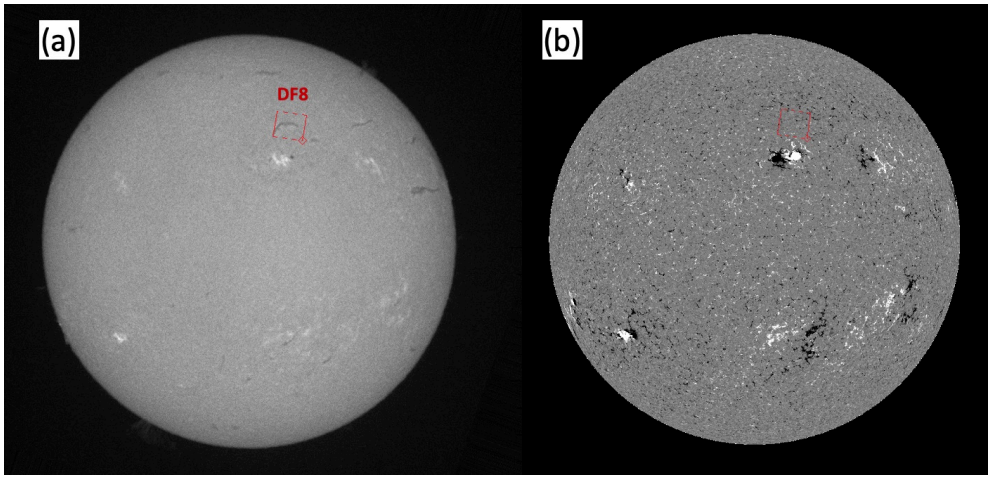

Figure 4.5: Location of the observational targets taken on 2022 Aug 24. Format of this figure is same as that of Figure 4.2.

4.3 Analysis

4.3.1 Data reduction and calibration

The obtained spectral data were reduced with dark frame subtraction and flat-fielding. The orthogonally polarized spectra recorded simultaneously by the NIR camera were aligned after correcting the distortion of spectral images by referring to 5 hair lines imaged on the spectra taken after the observation sequence (see Figure 4.6). Then we performed polarization demodulation for each set of 200 images, and combined them to obtain Stokes I, Q, U, and V spectrum. Regarding the calibration of the instrumental polarization of the DST, we referred to Anan et al. (2018). For an initial guess of the Müller matrix of the DST, we used the data obtained by Anan et al. (2012). Further adjustment of the matrix is done by making the Zeeman signals in Si I 10827 Å line to be symmetric (Q and U) or anti-symmetric (V) in a sunspot observed before or after the filament observation. After polarization calibration, we removed artificial fringe pattern in Stokes Q, U, and V spectra by subtracting periodic component in dispersion direction. For more details of the calibration procedure, see Ichimoto et al. (2022).

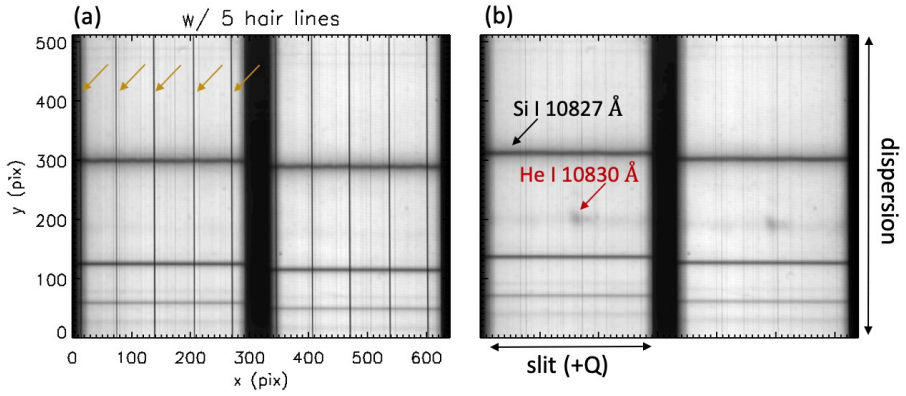

Figure 4.6: (a) Example of a calibration data with 5 hair lines. Yellow arrows indicate the hair lines. (b) Example of an observed raw spectra. Black and red arrows indicate the Si I 10827 Å and the He I 10830 Å lines, respectively. Horizontal and vertical axes correspond to the slit and dispersion directions, respectively. The slit direction defines the $+Q$ axis.

4.3.2 Stokes Inversions

4.3.2.1 Coordinate system

In our study, we use two different coordinate systems as given in Asensio Ramos et al. (2008): the local frame at the target region on the sun and the observer's frame. Figure

4.7 show these coordinate systems. The vectors $\boldsymbol{e_{x,y,z}}$ are the unit vectors of the cartesian coordinate in local frame, and the vectors $\boldsymbol{e_{tx,ty,l}}$ are the unit vectors of the cartesian coordinate in observers' frame where $\boldsymbol{e_{tx}}$, $\boldsymbol{e_{ty}}$, and $\boldsymbol{e_l}$ represent the slit, scan, and line-of-sight directions, respectively. We denote the vector magnetic field ($\boldsymbol{B}$) in the local frame as $B_{x,y,z}$. By using the field strength ($|\boldsymbol{B}|$), the inclination (θ) and the azimuth (ϕ) of the magnetic field in the local coordinate, we can describe each of the magnetic field components as follows:

$$\begin{aligned} B_x &= |\boldsymbol{B}| \sin\theta \cos\phi, \\ B_y &= |\boldsymbol{B}| \sin\theta \sin\phi, \\ B_z &= |\boldsymbol{B}| \cos\theta. \end{aligned}$$

In this paper, we call B_x and B_y as the $horizontal\ component$ and B_z as the $vertical\ component$ of the magnetic field, respectively. We denote the magnetic field in the observer's frame as $B_{tx,ty,l}$. The relation between the magnetic field components in the local frame and the observer's frame is given by

$$\begin{aligned} B_{tx} &= B_y \sin\gamma + (B_x \cos\psi - B_z \sin\psi)\cos\gamma, \\ B_{ty} &= B_y \cos\gamma - (B_x \cos\psi - B_z \sin\psi)\sin\gamma, \\ B_l &= B_z \cos\psi + B_x \sin\psi, \end{aligned}$$

where γ is the angle between $\boldsymbol{e_{tx}}$ and the direction of solar radius ($\boldsymbol{e'_z}$), and ψ is the angle between $\boldsymbol{e_z}$ and $\boldsymbol{e_l}$ (see Figure 4.7). In this paper, we call B_{tx} and B_{ty} as the $transverse\ component$ and B_l as the $longitudinal\ component$, respectively.

4.3.2.2 Stokes inversion

To deduce the photospheric vector magnetic field, we applied the Milen Eddington inversion to the full Stokes profiles of Si I 10827 Å line. The inversion code includes 8 physical parameters: the magnetic field strength, the inclination and azimuth of the magnetic field vector in observer's frame, the line of sight velocity, the turbulent velocity, the damping constant of the line, the continuum intensity, and the ratio of the opacities in line center and continuum.

To obtain the magnetic field in the filaments, we performed the Stokes inversion for full Stokes profiles of He I 10830 Å by using the HAZEL code developed by Asensio Ramos et al. (2008). This inversion code takes into account not only the Zeeman effect but also the atomic polarization. The HAZEL obtains 8 physical parameters from the fitting of observed Stokes profiles, $i.e.$, the magnetic field strength ($|\boldsymbol{B}|$), the inclination (θ) and azimuth (ϕ) of the magnetic field vector with respect to the local vertical, the optical thickness (τ), the Doppler velocity ($v_{\rm doppler}$), the turbulent velocity ($v_{\rm turb}$), the line damping

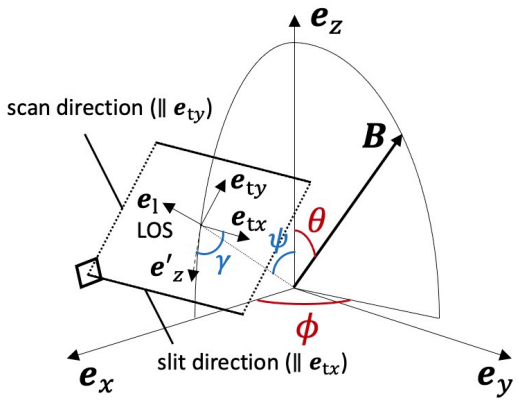

Figure 4.7: Definition of the coordinate systems in the local frame and the observer's frame. The vectors $\boldsymbol{e_x}, \boldsymbol{e_y}$, and $\boldsymbol{e_z}$ correspond to the cartesian coordinate units in local frame. θ and ϕ represent the inclination and azimuth angles of the magnetic field vector, $\boldsymbol{B}$ with respect to the local frame coordinate system. The vectors $\boldsymbol{e_{tx}}, \boldsymbol{e_{ty}}$, and $\boldsymbol{e_l}$ correspond to cartesian coordinate units in observers' frame where $\boldsymbol{e_l}$ is in line-of-sight. γ represents the angle between $\boldsymbol{e_{tx}}$ and the direction of solar radius ($\boldsymbol{e'_z}$). ψ is the angle between $\boldsymbol{e_z}$ and $\boldsymbol{e_l}$. Diamond symbol represents the origin of the field of view. Solid and dashed lines correspond to the slit and scan directions, respectively.

(a), and the filling factor (ff). To prevent unexpected results due to the Van-Vleck ambiguity (Landi Degl'Innocenti & Landolfi, 2004; Asensio Ramos et al., 2008), we performed the fitting for 3 different ranges of the inclination angle separately. They are referred to "case A" for $0°.0 < \theta < 54°.74$, "case B" for $54°.74 < \theta < 125°.26$, and "case C" for $125°.26 < \theta < 180°.0$ in this paper. Regarding the other physical parameters, we set the range into $0.0 < |\boldsymbol{B}| < 500.0$ Gauss, $0°.0 < \phi < 360°.0$, $0.1 < \tau < 5.0$, $-20.0 < v_{\rm doppler} < 20.0$ km/s, $3.0 < v_{\rm turb} < 15.0$ km/s, $0.0 < a < 1.0$, and fixed $ff = 1.0$. Regarding the height of the dark filaments, we used the values shown in Table 4.2.

4.4 Results

4.4.1 Stokes signals

In Figure 4.8, we show the distribution of the Stokes signals in DF2. All the Stokes signals are normalized by the contiuum intensity. Panel (a) displays the intensity at the line center of He I 10830 Å, where we can identify the target filament as a dark structure. The blue symbol in panel (a) indicates the location of the pixel for which Stokes profiles are shown in Figure 4.9. Green contour shows the border of the filament determined from the Stokes

I map and represents the mask for the target region. Regarding the linear polarization signals of Stokes Q and U, we display the integrated values in range of ± 0.25 Å around the line center. We find negative and positive signals of up to $\sim 0.5\%$ through the filament body in Stokes Q and U, respectively (see panels (b) and (c) in Figure 4.8). Regarding the circular polarization signal of Stokes V, we display the value of the subtraction of the red wing at $+0.25$ Å and blue wing at -0.25 Å. We find positive signals through the filament body (see panel (d) in Figure 4.8).

Black symbols in Figure 4.9 shows the observed Stokes profiles around He I 10830 Å at the cyan pixel shown in Figure 4.8 (a). In Figure 4.9, we find -0.3% of the Stokes Q signal, 0.2% of Stokes U signal, and $\pm 0.05\%$ of Stokes V signal in observed profiles. Regarding the linear polarization signals, the main and sub components of the Stokes Q and U show the opposite sign, suggesting that these signals are caused by the Hanle effect (Trujillo Bueno et al., 2002). Regarding the circular polarization signal, both main and sub components show the anti-symmetric profiles, suggesting that this signal is caused by the longitudinal Zeeman effect. The colored solid curves with red, green, and blue show the fitting results from the HAZEL inversion for the "case A", "case B", and "case C", respectively. As shown in panel (a), all the cases successfully fit the observed intensity profile. Regarding the fittig of Stokes Q and U profiles shown in panels (b) and (c), we find similar synthetic profiles in all the three cases. However, for the fitting of Stokes V profile in panel (d), while the "case B" and "case C" with green and blue lines show similar profiles that well fit the observation, the "case A" with red line shows siginificant difference from the other two cases. The physical parameters at the pixel of interest obtained from the inversion for three cases are summarized in Table 4.3. These results suggest that there are two plausible solutions; $i.e.$, the "case B" and "case C", due to the Van-Vleck ambiguity. To show the goodness of the fitting among these three cases through the filament body, we show the χ^2 distributions for three cases in Figure 4.10. As we can clearly find, the "case A" is the worst fitting among them, and the "case B" and "case C" show similar χ^2 distributions for the whole dark filament body.

Table 4.3: Inversion results for three cases at the pixel of interest

	$\lvert\boldsymbol{B}\rvert$ [Gauss]	θ [deg]	ϕ [deg]	τ	$v_{\rm turb}$ [km/s]	a	ff [1]
"case A"	4.0	24.1	168.3	0.80	5.0	0.76	1.0
"case B"	18.4	99.7	310.0	0.80	5.0	0.74	1.0
"case C"	14.0	156.4	336.8	0.79	5.0	0.76	1.0

[1] Filling factor was set to 1 for all the cases.

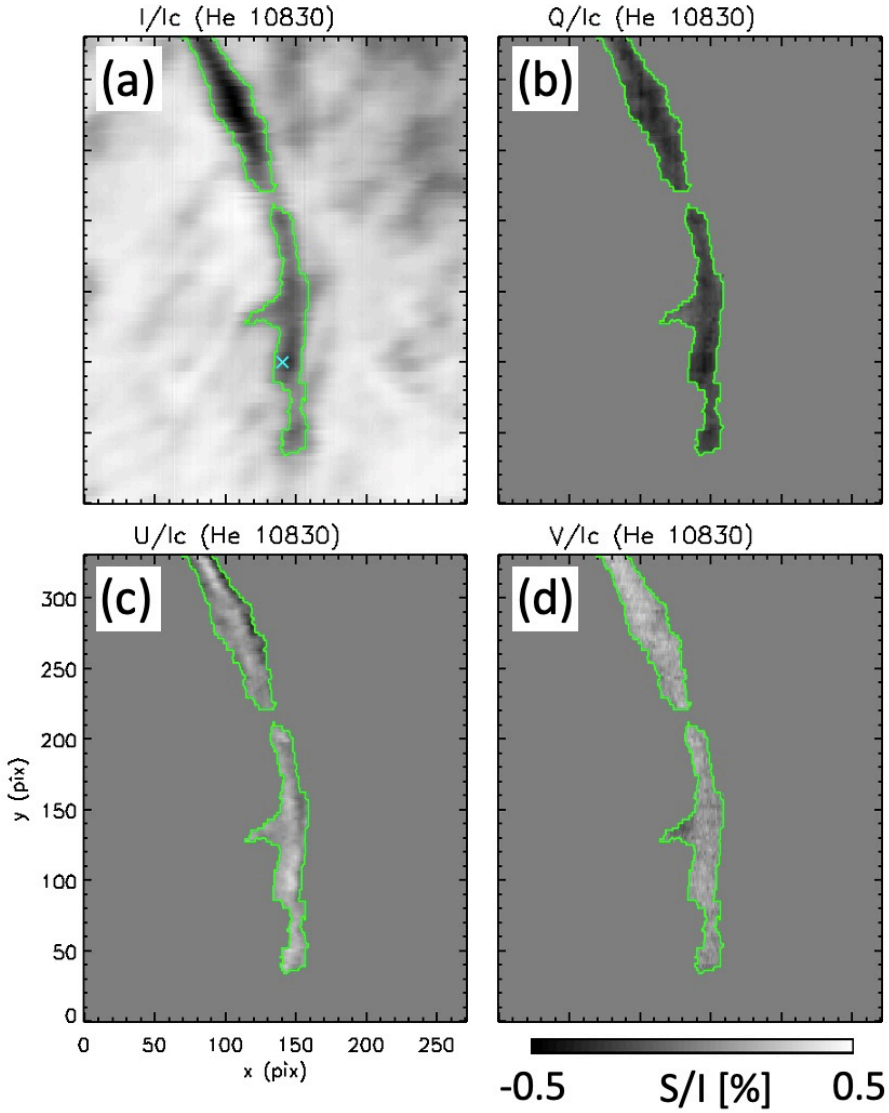

Figure 4.8: Distribution of Stokes signal for DF2. (a) Stokes I image at the line center of He I 10830 Å. Blue cross symbol in the panel shows the location of the pixel of interest. (b,c) Stokes Q and U integrated values in a range of ± 0.25 Å around the line center of He I 10830 Å and normalized by continuum intensity. (d) Stokes V image made from subtraction of red (0.25 Å) and blue (-0.25 Å) wing normalized by continuum intensity. Green contour show the mask for the target dark filament region.

4.4.2 Inversion results

Under the assumption that, in the filaments, the strength of the horizontal magnetic field is superior to the vertical component, we adopted the inversion result from "case B", in which we performed the inversion with the inclination angle ristriction of $54°.74 < \theta < 125°.26$, as our solution. In Figure 4.11, we show the distributions of the vector magnetic field in

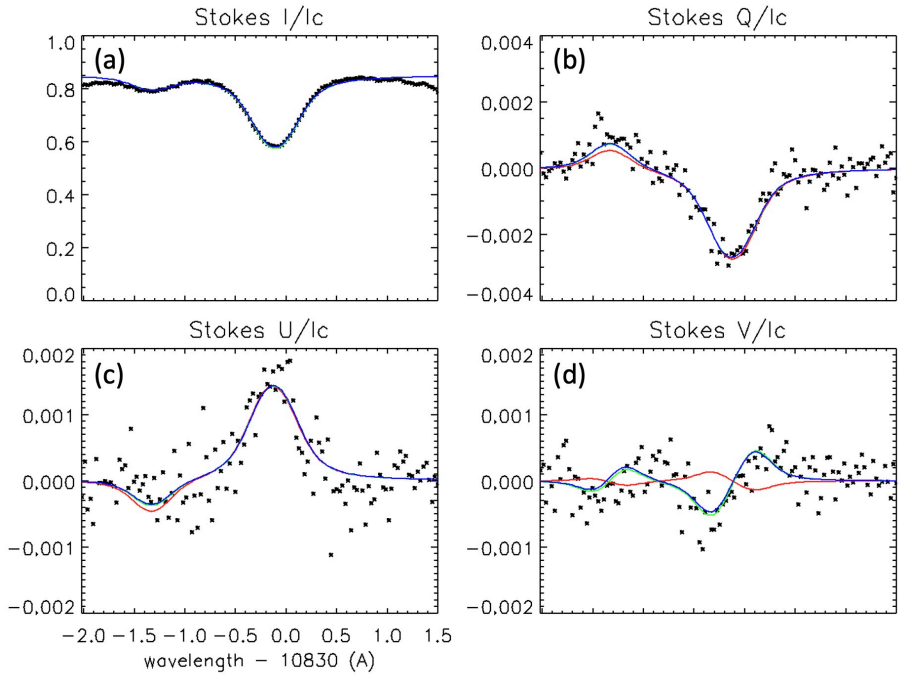

Figure 4.9: Stokes profiles of I, Q, U, and V at pixel of interest of DF2 (see the red symbol in Figure **??** (a)). Black symbols show the observational data. Red, green, and blue solid lines show the fitting results for "case A", "case B", "case C", respectively.

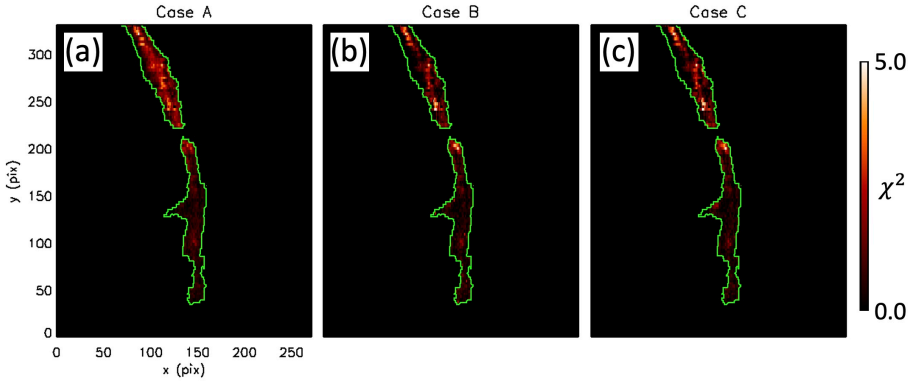

Figure 4.10: χ^2 value distribution for three individual inversions. (a) "case A", (b) "case B", (c) "case C". Green contour show the region of dark filament body.

the observer's frame obtained from the "case B" inversion.

Taking into account the projection effect and the sign of the longitudinal magnetic field in observer's frame (B_l), we solved the 180 degree ambiguity problem. As shown in panel (b) of Figure 4.11, B_l has a positive trend through the filament body. Therfore, the direction of the axial magnetic field of the filament is expected to be the direction towards us, $i.e.$, from solar limb to disk center. In this way, we determined the direction of the transverse

magnetic field in observer's frame ($\boldsymbol{B_t}$) as shown in red arrows in panel (a) of Figure 4.11. We performed the same analysis for all the targets, and the results are summarized in Table 4.4. Here we note that the obtained magnetic field is more or less uniform in major part of the filament body and the values of the longitudinal component (B_l), the field strength ($|\boldsymbol{B}|$), the inclination angle (θ), the azimuth angle (ϕ), and the optical thickness (τ) shown in Table 4.4 are the median values in the dark filament region.

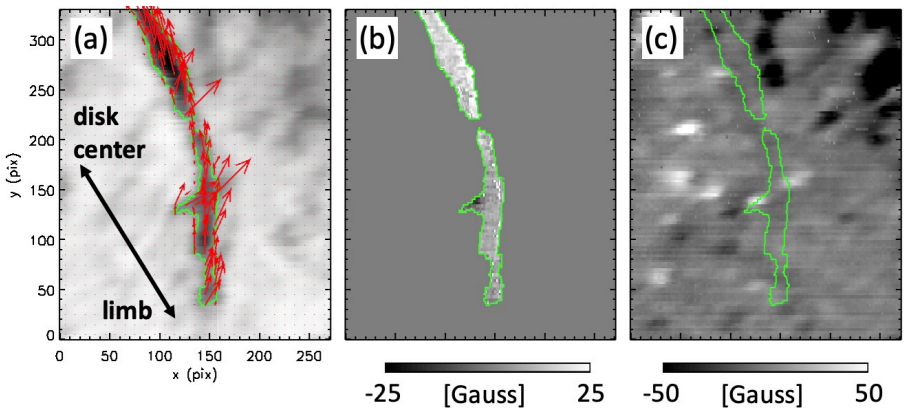

Figure 4.11: Vector magnetic field for DF2. (a) Horizontal magnetic field vector in observer's frame with red arrows are overplotted on Stokes I image at the line center of He I 10830 Å. (b) Longitudinal magnetic field in observer's frame. Green contour show the mask for the target dark filament region. (c) Line-of-sight component of the photospheric magnetic field obtained from Si I 10827 Å line observation. White- and black-colored region correspond to positive and negative polarity regions, respectively.

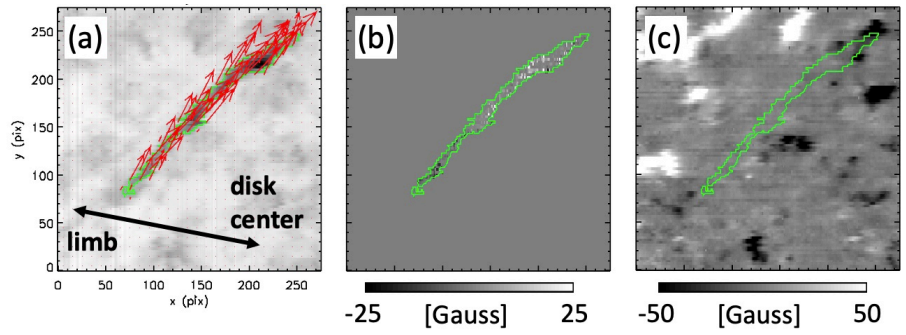

Figure 4.12: Vector magnetic field for DF6. (a) Horizontal magnetic field vector in observer's frame are overplotted with red arrows on Stokes I image at the line center of He I 10830 Å. (b) Longitudinal magnetic field in observer's frame. Green contour show the mask for the target dark filament region. (c) Line-of-sight component of the photospheric magnetic field obtained from Si I 10827 Å line observation. White- and black-colored region correspond to positive and negative polarity regions, respectively.

4.4.3 Magnetic field configuration

To clarify the type of magnetic field configuration of the filaments, we compared the direction of the transverse magnetic field ($\boldsymbol{B_t}$) in the filaments and the direction of the global magnetic field expected from the photospheric magnetic field. In Figure 4.11, we show the vector magnetic field of the filament and the line-of-sight component of the photospheric magnetic field obtained from the Si I 10827 Å line. As shown in panel (a), the direction of the transverse component of the magnetic field of the target filament is left-to-right direction as a whole. On the other hand, as shown in panel (c), photosphere in the left side and the right side of the filament have positive and negative polarities, respectively, $i.e.$, the global and the filament body magnetic field directions are the same. Thus, we suggest that the magnetic field configuration of this target, DF2, can be interpretted as the normal polarity model.

Furthermore, in Figure 4.11 (b), we can find that the left and right sides of the filament body show a hint of negative and positive polarities, respectively, and they are opposite signs from the underlying photosphere. This result also supports that the filament is trapped in the dip of the normal-polarity magnetic field structure (see Figure 4.1 (c)).

In Figure 4.12, we show an example of our target that has reverse polarity configuration. In panel (a), we display the transverse component of the magnetic field in the filament body with red arrows. In panel (c), the line-of-sight component of the photospheric magnetic field obtained from Si I 10827 Å is shown. Taking into account both the transverse component of the filament's magnetic field and the photospheric magnetic field, we can find that the former is in direction from bottom to top and the latter is in direction from top to bottom in the field-of-view, respectively. This means that this filament has reverse polarity configuration. Here we note that the 180 degree ambiguity of this sample has been also solved by the method that we introduced in Section 4.4.2.

Performing the same analysis for the other 6 targets, we found 6 out of 8 targets were the normal polarity (DF1, DF2, DF3, DF4, DF5, and DF8) and 2 out of 8 targets were the inverse polarity (DF6 and DF7). The results are summarized in the last column of Table 4.4.

Table 4.4: Magnetic field parameters and magnetic field configuration of the targets (θ and ϕ in local frame)

ID	$\lvert B_l \rvert$ [Gauss]	Field strength ($\lvert \boldsymbol{B} \rvert$) [Gauss]	Inclination (θ) [deg]	Azimuth (ϕ) [deg]	Optical thickness (τ)	Magnetic field configuration [1]
DF1 [2]	1	35	63	232	0.63	N
DF2	15	26	99	316	0.61	N
DF3 [2]	3	21	69	234	0.70	N
DF4	2	8	105	285	0.76	N
DF5	7	11	80	193	0.49	N
DF6	1	17	88	269	0.58	R
DF7 [2]	15	17	114	262	0.53	R
DF8 [3]	8	10	70	281	0.45	N

[1] "N" and "R" represent the normal and reverse polarity models, respectively.

[2] Targets locate above plage regions.

[3] One footpoint of the filament is connected to an active region.

4.5 Discussion

4.5.1 Magnetic field in local frame

As we presented in Table 4.4, we found that the field strength ($|\boldsymbol{B}|$) of our target filaments are in a range of $8 - 35$ Gauss. These results are consistent with the previous studies on quiescent filaments (see Table 4.1).

In the case of DF1, DF3, DF7, and DF8 which located above plage regions or near an active region, the inclination angles deviated more than 19° from 90°. Díaz Baso et al. (2016) suggests that the magnetic field obtained from He I 10830 Å may includes background effect if the filament is located above strong field regions (see also Díaz Baso et al., 2019a,b). Since plage regions have relatively strong field, the field inclination of the filaments in plage regions may be affected by the photospheric magnetic field.

4.5.2 Stokes signals vs. Magnetic field strength in observer's frame

In Figure 4.13, we plot the Stokes signal expected from the Zeeman and the Hanle effects against the magnetic field strength together with our observational results. Solid lines show the synthetic results obtained from HAZEL forward calculation. In the calculation, we assumed the position of the filament at disk center, and we adopted typical values of the physical parameters obtained from our inversion, $i.e.$, optical depth of 0.6, turbulent velocity of 5.0 km/s, damping constant of 0.8, and the filling factor of 1.0. Red, green, and black solid lines show the linear polarization signals of the Hanle effect, the transverse Zeeman effect, and sum of the Hanle and the Zeeman effects, respectively, against the strength of transversal magnetic field. Blue solid line shows the circular polarization signal of the longitudinal Zeeman effect against the strength of longitudinal magnetic field. Blue and orange symbols show the linear and circular polarization signals against the transversal and longitudinal components of magnetic fields obtained in this study for the 8 filaments.

Regarding the linear polarization, most of the orange symbols follow the red solid line rather than the green line. This suggests that the linear polarization signals are mainly caused by the Hanle effect in the filaments. Regarding the circular polarization, most of blue symbols follow the blue solid line. This suggests that the observed circular polarization signals are well explianed with the Zeeman effect.

Since the linear polarization signal caused by the Hanle effect in the He I 10830 Å line saturates ~ 8 Gauss (Trujillo Bueno et al., 2002), we need to estimate the field strength above ~ 8 Gauss from the circular polarization produced by the Zeeman effect (see red and blue solid lines in Figure 4.13). In Table 4.4, we also show the longitudinal component of the magnetic field ($B_{\rm l}$), which were estimated from the Zeeman signals observed in the

Stokes V profiles. They are found to be in range of $1 - 15$ Gauss. Previous researches that evaluated the magnetic field strength of the dark filament only by the Zeeman effect in the circular polarization (Leroy et al., 1983, 1984) may led to the underestimation of the field strength.

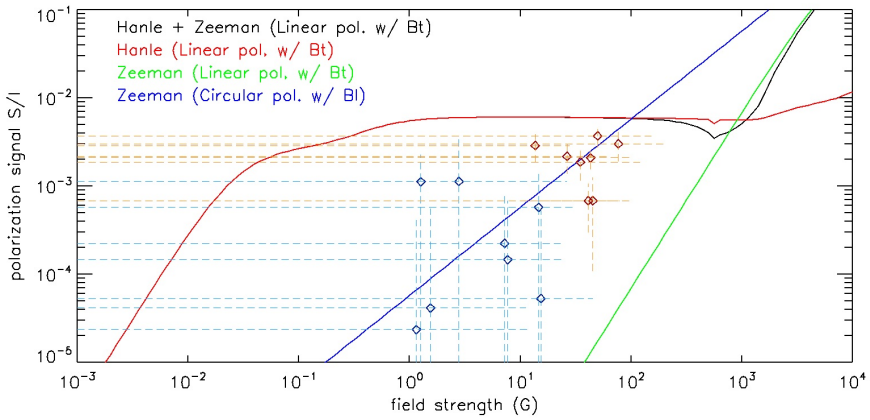

Figure 4.13: Stokes signal vs. Magnetic field strength. Red and green solid lines show the linear polarization signals with transverse magnetic field by the Hanle effect and by the Zeeman effect obtained from the synthetic profiles, respectively. Blue solid line shows the circular polarization signals with longitudinal magnetic field by the Zeeman effect obtained from the synthetic profiles. Black solid line show the sum of red and green solid lines. Blue and orange diamonds represent the transverse components with linear polarization signals and the longitudinal components with the circular polarization signals from our observations, respectively. Dashed lines represent the 1σ errors.

4.5.3 Magnetic field configuration of the filaments

As we presented in Table 4.4, we found that 6 out of 8 target DFs have normal polarity configuration (DF1, DF2, DF3, DF4, DF5, and DF8) and 2 out of 8 targets have reverse polarity configuration (DF6 and DF7). For other 6 samples besides DF2 and DF6, we display the results in Appendix. We could not find any correlations between the field configuration and field strength nor between the field configuration and the location of filaments, $i.e.$, if the target locates in a plage or in a quiet region. According to the previous research, Bommier & Leroy (1998) performed a polarimetric observation in the He I D3 5876 Å line and reported that the 264 out of 296 QS filaments have reverse polarity in their magnetic field configuration. This result is contradictory to the result in this study. By observing an off-limb prominence with He I 10830 Å line, Martínez González et al. (2015) also reported that the magnetic field configuration of a QS prominence was the reverse polarity model. One possible reason of the different tendency in the magnetic field configuration with respect to the location of the DFs found in our study and previous

works is that the difference in heights of the target DFs. Leroy et al. (1984) reported that prominences taller than 40" tend to have reverse configuration and shorter than 40" tend to have normal configuration (see also Engvold et al., 2019). Although our target DFs are not in active regions, the heights of majority are comparable to the height of typical AR filaments ($< 30\,''$). We suppose that some of our dark filaments were located in a remnant of active region and it is unclear if they can be classified as a quiescent filament.

4.6 Summary

We performed spectro-polarimetric observations in He I 10830 Å by using the updated spectro-polarimeter on the DST at Hida Observatory to clarify the magnetic field strength and the magnetic field configuration of dark filaments. The Stokes inversion of He I line was performed for 8 dark filaments with the HAZEL code. As a result of our analysis, we found that the field strength varies in a range of $8-35$ Gauss and that 6 out of 8 targets have the normal polarity configuration (Kippenhahn & Schlüter, 1957) and 2 out of 8 have the reverse polarity configuration (Kuperus & Raadu, 1974). We found a hint of side by side difference in the longitudinal component of magnetic field in DF2 and suggested that this signal may imply the dip of magnetic field in normal polarity configuration. However, such feature is not clear in other 7 filaments. We feel that observations with higher accuracy and higher spatial resolution are required to get a concrete picture of the field topology of the dark filaments.

CHAPTER 5

Concluding remarks

5.1 Conclusions

Taking into account all the findings of each Chapter, we summarize the conclusions of this thesis as follows:

(i) The formation process of MFRs was coupled with the flare activity in the AR. We found multiple MFRs formed more than 2 days before the onset of the X9.3 flare in AR NOAA 12673. We also found an enhancement and a reduction of magnetic twist at two footpoints of one MFR before and after the successive M class flares which took place 1 day before the X9.3 flare, respectively. However, the other MFR which produced the X9.3 flare remained for 2 days. By analyzing the 3D coronal magnetic field, we concluded that the MFR was suppressed by the newly formed coronal magnetic loops by reconnection of M class flares (Chapter 2).

(ii) The distribution of the twist flux, which is a multiplication of the magnetic flux and the magnetic twist of each field line, well represents the footpoints of MFRs. By comparing the integrated twist flux over the AR to the $GOES$ soft X-ray flux during the flare activity for several days, we found a good correlation with each other (Chapter 2).

(iii) The combination of the null point reconnection above the MFR and the TI played key roles to disrupt the equilibrium of MFR. We found an enhancement of EUV 1600 Å at the footpoints of ambient field lines which include the null point, and we also found that the MFR existed at the region with high decay index ($n > 1.5$) in the preflare phase of the M5.5 flare (Chapter 2).

(iv) ARs with quadrupole configurations tend to have a magnetic null point above the AR. The decay index value below the null point reaches high enough to the theoretical

threshold of the TI. If MFRs exist below the null point, MFRs have the potential to erupt by the TI and the null point reconnection (Chapters 2 and 3).

(v) The acceleration mechanism of the MFR of the eruptive X1.0 flare in AR NOAA 12887 was the combination of the TI and the push-up motion by the newly formed magnetic arcade below the erupting MFR. In addition, by performing the hypothetical simulation with reconnection suppression, we also concluded that the MFR can erupt without the push-up motion (Chapter 3).

(vi) The magnetic field strength of dark filaments which are the plasmas suspended by MFRs was in a range of $8 - 35$ Gauss (Chapter 4).

(vii) The magnetic field configuration of MFRs can be both the normal polarity and the reverse polarity. We found 6 normal-polarity dark filaments and 2 reverse-polarity dark filaments in our observed 8 targets (Chapter 4).

5.2 Future perspective

For future work, we will resolve the plasma dynamics not only in the photosphere and the corona but also in the chromosphere in ARs by using both the approaches of observation and numerical modeling. The numerical methods we used in this thesis, especially for Chapters 2 and 3, were based on the force-free approximation. Although the NLFFF extrapolation is a powerful method to investigate the 3D coronal magnetic field, it is not suitable for the lower layers of the solar atmosphere such as the photosphere and the lower chromosphere. This is because, in the photosphere or in the lower chromosphere, gas pressure is comparable to magnetic pressure, $i.e.$, $\beta \sim 1$ (see Figure 1.2 in Section 1.1). Yelles Chaouche et al. (2012) and Kawabata et al. (2020) also pointed out a gap between the magnetic field of NLFFF and that of direct observations. To overcome this problem, we need to solve gas pressure and gravity terms simultaneously in the EOM (see eq. (1.1)). This is called non-force-free field (NFFF) modeling and the basic development of an extrapolation code is now ongoing (Miyoshi et al., 2020). However, in their method, they put a pressure scale height by assuming that the temperature profile in the solar atmosphere depends only on the height. If we determine the scale height based on observations, we can improve the NFFF modeling method.

Diagnostics of the magnetic field and the other physical parameters such as the temperature and the density through the photosphere to the corona including the chromosphere with a high spatial resolution are also important to investigate the fine structures of MFRs and the ambient magnetic field structure surrounding MFRs. We display a schematic that represents the connection of the magnetic field through the solar atmosphere in Figure 5.1.

The Daniel K. Inouye Solar Telescope (DKIST: Rimmele et al., 2020) has the DL-NIRSP and the Cryo-NIRSP. By using these instruments, we can perform spectro-polarimetric observations in the lines which have sensitivity in the chromospheric magnetic field with the spatial resolution of $\sim 0.1''$ ($= 70$ km). Direct observation of solar dark filaments with these instruments will improve our study presented in Chapter 4. Although the instruments are ground-based, they could diagnose the temperature range of $5 \times 10^3 - 10^4$ K which corresponds to the photosphere to the upper chromosphere. In the middle of the 2020s, the Solar-C (Shimizu et al., 2020) will be launched, which can obtain spectroscopic data in EUV from the lower chromosphere to the corona seamlessly with a high spatial resolution of $\sim 0.4''$ ($= 300$ km). This instrument has the capability of observing the temperature range of $10^4 - 10^7$ K which corresponds to the upper chromosphere to the corona. In terms of the solar flare study, by using the improved NFFF extrapolation with the observation of the DKIST, the Solar-C, and other new instruments will lead us to the comprehension of the dynamics of magnetic field through the solar atmosphere; we may find some evidence of the TC reconnection in the formation phase of MFRs, breakout current sheet in erupting phase of MFRs, or any other candidates that explain the dynamics of MFRs during solar flares well in the observation or in the modeled NFFF.

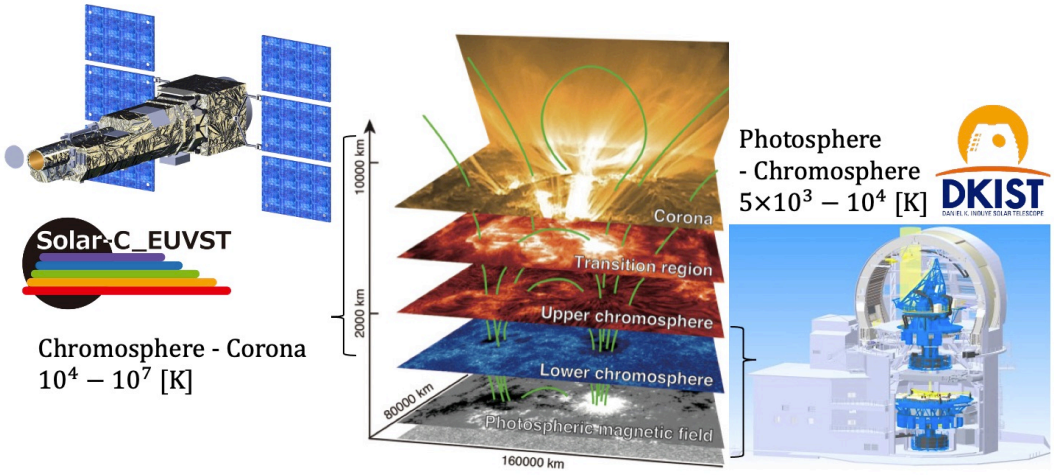

Figure 5.1: Connection of magnetic field through the solar atmosphere. Observation range with the Solar-C and the DKIST. For the image of the Solar-C and the middle figure © ISAS/JAXA. For the image of the DKIST © NSO.

APPENDIX A

Supplementary materials in Chapter 4

A.1 Magnetic field configuration for all the targets

In Figures A.1, A.2, A.3, A.4, A.5, and A.6, we display the magnetic field configuration for DF1, DF3, DF4, DF5, DF7, and DF8, respectively. Panels (a), (b), and (c) in each figure show transverse magnetic field vector in observer's frame with red arrows overplotted on Stokes I at the line center of He I 10830 Å, longitudinal magnetic field from He I 10830 Å, and line-of-sight component of the photospheric magnetic field from Si I 10827 Å, respectively. White- and black-colored region in panels (b) and (c) are positive and negative polarities, respectively. Green contour in all panels show the border of the target dark filament. Inversion results (median values in the filament) for these target DFs are listed in Table 4.4.

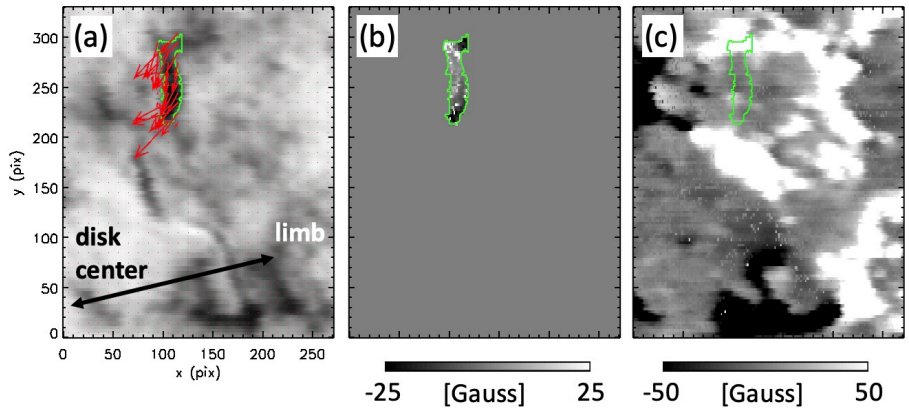

Figure A.1: Vector magnetic field for DF1. The formats of this figure is same as that of Figure 4.11.

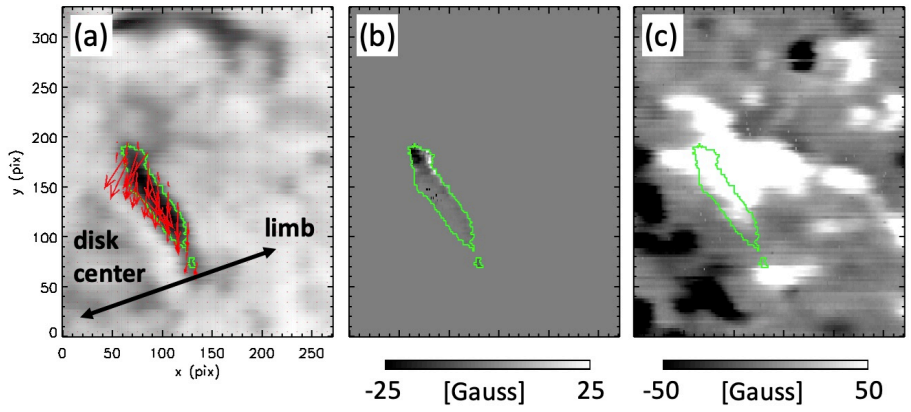

Figure A.2: Vector magnetic field for DF3. The formats of this figure is same as that of Figure 4.11.

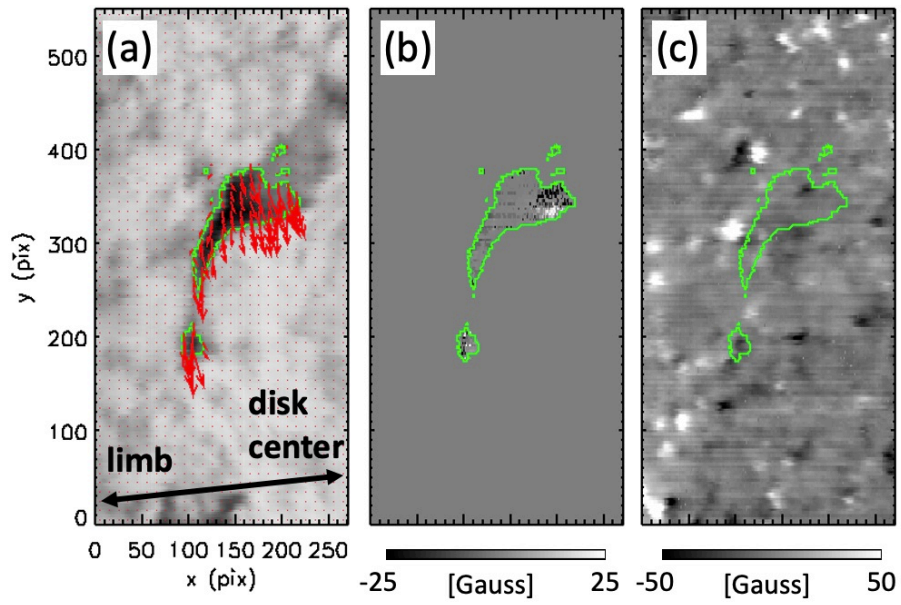

Figure A.3: Vector magnetic field for DF4. The formats of this figure is same as that of Figure 4.11.

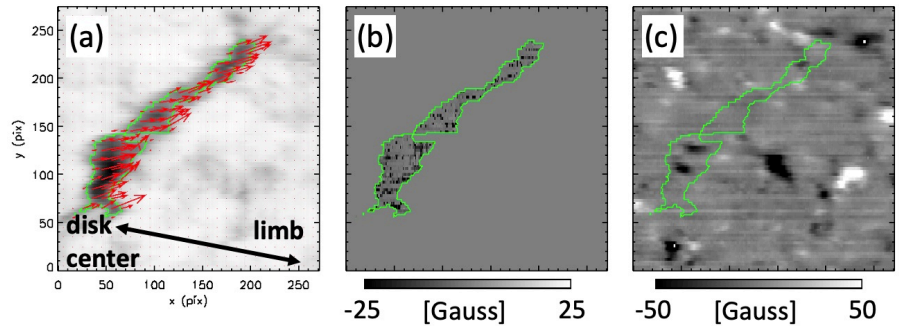

Figure A.4: Vector magnetic field for DF5. The formats of this figure is same as that of Figure 4.11.

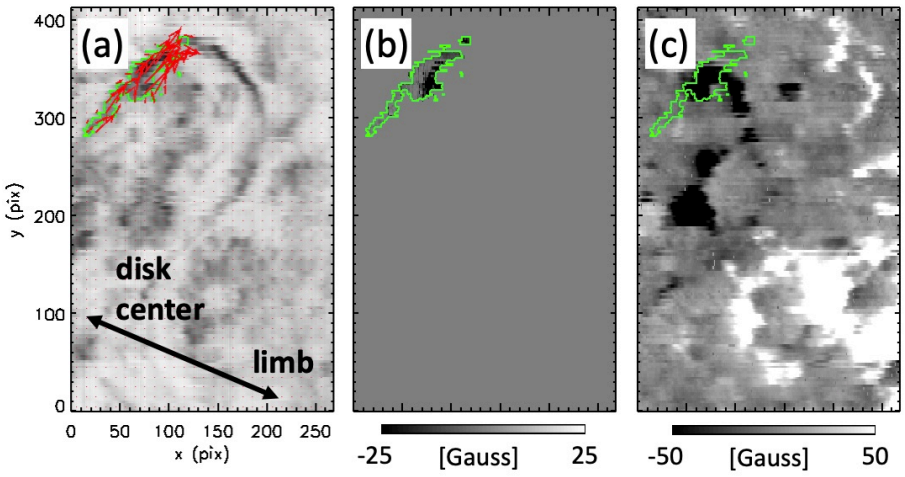

Figure A.5: Vector magnetic field for DF7. The formats of this figure is same as that of Figure 4.11.

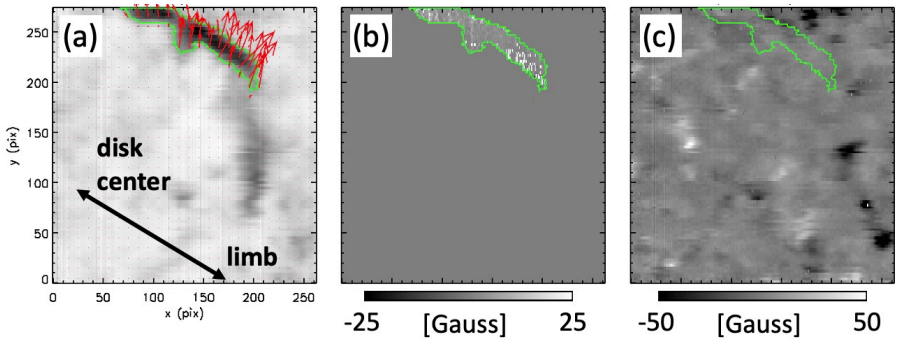

Figure A.6: Vector magnetic field for DF8. The formats of this figure is same as that of Figure 4.11.

Bibliography

Anan, T., Ichimoto, K., Oi, A., et al. 2012, in Society of Photo-Optical Instrumentation Engineers (SPIE) Conference Series, Vol. 8446, Ground-based and Airborne Instrumentation for Astronomy IV, ed. I. S. McLean, S. K. Ramsay, & H. Takami, 84461C, doi: 10.1117/12.925639

Anan, T., Huang, Y.-W., Nakatani, Y., et al. 2018, PASJ, 70, 102, doi: 10.1093/pasj/psy041

Antiochos, S. K., DeVore, C. R., & Klimchuk, J. A. 1999, ApJ, 510, 485, doi: 10.1086/306563

Asai, A., Yokoyama, T., Shimojo, M., et al. 2004, ApJ, 611, 557, doi: 10.1086/422159

Asensio Ramos, A., Trujillo Bueno, J., & Landi Degl'Innocenti, E. 2008, ApJ, 683, 542, doi: 10.1086/589433

Babcock, H. W., & Babcock, H. D. 1955, ApJ, 121, 349, doi: 10.1086/145994

Bamba, Y., Inoue, S., & Imada, S. 2020, ApJ, 894, 29, doi: 10.3847/1538-4357/ab85ca

Berger, M. A., & Prior, C. 2006, Journal of Physics A Mathematical General, 39, 8321, doi: 10.1088/0305-4470/39/26/005

Bobra, M. G., Sun, X., Hoeksema, J. T., et al. 2014, Solar Physics, 289, 3549, doi: 10.1007/s11207-014-0529-3

Bommier, V., Landi Degl'Innocenti, E., Leroy, J.-L., & Sahal-Brechot, S. 1994, SoPh, 154, 231, doi: 10.1007/BF00681098

Bommier, V., & Leroy, J. L. 1998, in Astronomical Society of the Pacific Conference Series, Vol. 150, IAU Colloq. 167: New Perspectives on Solar Prominences, ed. D. F. Webb, B. Schmieder, & D. M. Rust, 434

Bommier, V., Sahal-Brechot, S., & Leroy, J. L. 1986, A&A, 156, 79

Carmichael, H. 1964, in NASA Special Publication, Vol. 50, 451

Carrington, R. C. 1859, MNRAS, 20, 13, doi: 10.1093/mnras/20.1.13

Casini, R., López Ariste, A., Tomczyk, S., & Lites, B. W. 2003, ApJL, 598, L67, doi: 10.1086/380496

Chen, P. F. 2011, Living Reviews in Solar Physics, 8, 1, doi: 10.12942/lrsp-2011-1

Cheng, X., Guo, Y., & Ding, M. 2017, Science China Earth Sciences, 60, 1383, doi: 10.1007/s11430-017-9074-6

Chertok, I. M., Belov, A. V., & Abunin, A. A. 2018, Space Weather, 16, 1549, doi: 10.1029/2018SW001899

Chintzoglou, G., Zhang, J., Cheung, M. C. M., & Kazachenko, M. 2019, ApJ, 871, 67, doi: 10.3847/1538-4357/aaef30

Coppi, B., & Friedland, A. B. 1971, ApJ, 169, 379, doi: 10.1086/151150

de la Cruz Rodríguez, J., & van Noort, M. 2017, SSRv, 210, 109, doi: 10.1007/s11214-016-0294-8

Dedner, A., Kemm, F., Kröner, D., et al. 2002, Journal of Computational Physics, 175, 645, doi: 10.1006/jcph.2001.6961

Desai, M., & Giacalone, J. 2016, Living Reviews in Solar Physics, 13, 3, doi: 10.1007/s41116-016-0002-5

Díaz Baso, C. J., Martínez González, M. J., & Asensio Ramos, A. 2016, ApJ, 822, 50, doi: 10.3847/0004-637X/822/1/50

—. 2019a, A&A, 625, A128, doi: 10.1051/0004-6361/201834790

—. 2019b, A&A, 625, A129, doi: 10.1051/0004-6361/201834791

Engvold, O., Vial, J.-C., & Skumanich, A. 2019, The Sun as a Guide to Stellar Physics, doi: 10.1016/C2017-0-01365-4

Fan, Y., & Gibson, S. E. 2003, ApJL, 589, L105, doi: 10.1086/375834

Filippov, B., Martsenyuk, O., Srivastava, A. K., & Uddin, W. 2015, Journal of Astrophysics and Astronomy, 36, 157, doi: 10.1007/s12036-015-9321-5

Gary, G. A. 2001, SoPh, 203, 71, doi: 10.1023/A:1012722021820

Gibson, S. E. 2018, Living Reviews in Solar Physics, 15, 7, doi: 10.1007/s41116-018-0016-2

Guo, Y., Cheng, X., & Ding, M. 2017, Science China Earth Sciences, 60, 1408, doi: 10.1007/s11430-017-9081-x

Hanaoka, Y., & Sakurai, T. 2017, ApJ, 851, 130, doi: 10.3847/1538-4357/aa9cf1

Handy, B. N., Acton, L. W., Kankelborg, C. C., et al. 1999, SoPh, 187, 229, doi: 10.1023/A:1005166902804

Hanle, W. 1924, Zeitschrift fur Physik, 30, 93, doi: 10.1007/BF01331827

Harvey, J., & GONG Instrument Team. 1995, in Astronomical Society of the Pacific Conference Series, Vol. 76, GONG 1994. Helio- and Astro-Seismology from the Earth and Space, ed. R. K. Ulrich, J. Rhodes, E. J., & W. Dappen, 432

Harvey, J. W., Hill, F., Hubbard, R. P., et al. 1996, Science, 272, 1284, doi: 10.1126/science.272.5266.1284

He, W., Jiang, C., Zou, P., et al. 2020, ApJ, 892, 9, doi: 10.3847/1538-4357/ab75ab

Hirayama, T. 1974, SoPh, 34, 323, doi: 10.1007/BF00153671

Hodgson, R. 1859, MNRAS, 20, 15, doi: 10.1093/mnras/20.1.15

Hoeksema, J. T., Liu, Y., Hayashi, K., et al. 2014, Solar Physics, 289, 3483, doi: 10.1007/s11207-014-0516-8

Hou, Y. J., Zhang, J., Li, T., Yang, S. H., & Li, X. H. 2018, A&A, 619, A100, doi: 10.1051/0004-6361/201732530

Hou, Z., Tian, H., Wang, J.-S., et al. 2022, ApJ, 928, 98, doi: 10.3847/1538-4357/ac590d

Ichimoto, K., Huang, Y. W., Yamasaki, D., et al. 2022, Tech. Rep. from Astron. Obs. Grad. School of Science, Kyoto Univ., 6-3, doi: 2433/278127

Ichimoto, K., Lites, B., Elmore, D., et al. 2008, SoPh, 249, 233, doi: 10.1007/s11207-008-9169-9

Ichimoto, K., Ishii, T. T., Otsuji, K., et al. 2017, SoPh, 292, 63, doi: 10.1007/s11207-017-1082-7

Inoue, S. 2016, Progress in Earth and Planetary Science, 3, 19, doi: 10.1186/s40645-016-0084-7

Inoue, S., & Bamba, Y. 2021, ApJ, 914, 71, doi: 10.3847/1538-4357/abf835

Inoue, S., Hayashi, K., & Kusano, K. 2016, ApJ, 818, 168, doi: 10.3847/0004-637X/818/2/168

Inoue, S., Hayashi, K., Magara, T., Choe, G. S., & Park, Y. D. 2014a, ApJ, 788, 182, doi: 10.1088/0004-637X/788/2/182

—. 2015, ApJ, 803, 73, doi: 10.1088/0004-637X/803/2/73

Inoue, S., Hayashi, K., Shiota, D., Magara, T., & Choe, G. S. 2013, ApJ, 770, 79, doi: 10.1088/0004-637X/770/1/79

Inoue, S., Kusano, K., Büchner, J., & Skála, J. 2018, Nature Communications, 9, 174, doi: 10.1038/s41467-017-02616-8

—. 2018a, Nature Communications, 9, 174, doi: 10.1038/s41467-017-02616-8

Inoue, S., Kusano, K., Magara, T., Shiota, D., & Yamamoto, T. T. 2011, ApJ, 738, 161, doi: 10.1088/0004-637X/738/2/161

Inoue, S., Magara, T., Pandey, V. S., et al. 2014b, ApJ, 780, 101, doi: 10.1088/0004-637X/780/1/101

Inoue, S., Shiota, D., Bamba, Y., & Park, S.-H. 2018b, ApJ, 867, 83, doi: 10.3847/1538-4357/aae079

Ishiguro, N., & Kusano, K. 2017, ApJ, 843, 101, doi: 10.3847/1538-4357/aa799b

Ishikawa, R., Trujillo Bueno, J., Uitenbroek, H., et al. 2017, ApJ, 841, 31, doi: 10.3847/1538-4357/aa6ca9

Jiang, C., Feng, X., & Hu, Q. 2018, ApJ, 866, 96, doi: 10.3847/1538-4357/aadd08

Jiang, C., Feng, X., Wu, S. T., & Hu, Q. 2013, ApJL, 771, L30, doi: 10.1088/2041-8205/771/2/L30

Jiang, C., Wu, S. T., Yurchyshyn, V., et al. 2016, ApJ, 828, 62, doi: 10.3847/0004-637X/828/1/62

Jiang, C., Feng, X., Liu, R., et al. 2021, Nature Astronomy, 5, 1126, doi: 10.1038/s41550-021-01414-z

Jing, J., Liu, C., Lee, J., et al. 2018, ApJ, 864, 138, doi: 10.3847/1538-4357/aad6e4

Joshi, N. C., Joshi, B., & Mitra, P. K. 2021, MNRAS, 501, 4703, doi: 10.1093/mnras/staa3480

Kane, S. R., Kreplin, R. W., Martres, M. J., Pick, M., & Soru-Escaut, I. 1974, SoPh, 38, 483, doi: 10.1007/BF00155083

Kang, J., Magara, T., Inoue, S., Kubo, Y., & Nishizuka, N. 2016, PASJ, 68, 101, doi: 10.1093/pasj/psw092

Karpen, J. T., Antiochos, S. K., & DeVore, C. R. 2012, ApJ, 760, 81, doi: 10.1088/0004-637X/760/1/81

Kawabata, Y., Asensio Ramos, A., Inoue, S., & Shimizu, T. 2020, ApJ, 898, 32, doi: 10.3847/1538-4357/ab9816

Kawabata, Y., Inoue, S., & Shimizu, T. 2017, ApJ, 842, 106, doi: 10.3847/1538-4357/aa71a0

Kihara, K., Huang, Y., Nishimura, N., et al. 2020, ApJ, 900, 75, doi: 10.3847/1538-4357/aba621

Kippenhahn, R., & Schlüter, A. 1957, ZA, 43, 36

Kliem, B., Lee, J., Liu, R., et al. 2021, ApJ, 909, 91, doi: 10.3847/1538-4357/abda37

Kliem, B., & Török, T. 2006, PhRvL, 96, 255002, doi: 10.1103/PhysRevLett.96.255002

Kopp, R. A., & Pneuman, G. W. 1976, SoPh, 50, 85, doi: 10.1007/BF00206193

Kosugi, T., Matsuzaki, K., Sakao, T., et al. 2007, SoPh, 243, 3, doi: 10.1007/s11207-007-9014-6

Kuckein, C., Centeno, R., Martínez Pillet, V., et al. 2009, A&A, 501, 1113, doi: 10.1051/0004-6361/200911800

Kuperus, M., & Raadu, M. A. 1974, A&A, 31, 189

Kusano, K., Iju, T., Bamba, Y., & Inoue, S. 2020, Science, 369, 587, doi: 10.1126/science.aaz2511

Landi Degl'Innocenti, E., & Landolfi, M. 2004, Polarization in Spectral Lines, Vol. 307, doi: 10.1007/978-1-4020-2415-3

Lemen, J. R., Title, A. M., Akin, D. J., et al. 2012, Solar Physics, 275, 17, doi: 10.1007/s11207-011-9776-8

Leroy, J. L., Bommier, V., & Sahal-Brechot, S. 1983, SoPh, 83, 135, doi: 10.1007/BF00148248

—. 1984, A&A, 131, 33

Li, X., Wang, Y., Guo, J., & Lyu, S. 2022, ApJL, 928, L6, doi: 10.3847/2041-8213/ac5b72

Liu, L., Cheng, X., Wang, Y., & Zhou, Z. 2019, ApJ, 884, 45, doi: 10.3847/1538-4357/ab3c6c

Liu, R., Kliem, B., Titov, V. S., et al. 2016, ApJ, 818, 148, doi: 10.3847/0004-637X/818/2/148

Martin, S. F. 1998, SoPh, 182, 107, doi: 10.1023/A:1005026814076

Martínez González, M. J., Manso Sainz, R., Asensio Ramos, A., et al. 2015, ApJ, 802, 3, doi: 10.1088/0004-637X/802/1/3

Masuda, S., Kosugi, T., Hara, H., Tsuneta, S., & Ogawara, Y. 1994, Nature, 371, 495, doi: 10.1038/371495a0

Mitra, P. K., Joshi, B., Prasad, A., Veronig, A. M., & Bhattacharyya, R. 2018, ApJ, 869, 69, doi: 10.3847/1538-4357/aaed26

Miyoshi, T., Kusano, K., & Inoue, S. 2020, ApJS, 247, 6, doi: 10.3847/1538-4365/ab64f2

Moore, R. L., Sterling, A. C., Hudson, H. S., & Lemen, J. R. 2001, ApJ, 552, 833, doi: 10.1086/320559

Muhamad, J., Kusano, K., Inoue, S., & Bamba, Y. 2018, ApJ, 863, 162, doi: 10.3847/1538-4357/aad181

Nagata, S., Morita, S., Ichimoto, K., et al. 2014, PASJ, 66, 45, doi: 10.1093/pasj/psu023

Nakai, Y., & Hattori, A. 1985, Memoirs Faculty of Sciences University of Kyoto, 36, 385

Okada, S., Ichimoto, K., Machida, A., et al. 2020, PASJ, 72, 71, doi: 10.1093/pasj/psaa014

Okamoto, T. J., Tsuneta, S., Lites, B. W., et al. 2008, ApJL, 673, L215, doi: 10.1086/528792

Orozco Suárez, D., Asensio Ramos, A., & Trujillo Bueno, J. 2014, A&A, 566, A46, doi: 10.1051/0004-6361/201322903

Papaioannou, A., Kouloumvakos, A., Mishev, A., et al. 2022, A&A, 660, L5, doi: 10.1051/0004-6361/202142855

Parenti, S. 2014, Living Reviews in Solar Physics, 11, 1, doi: 10.12942/lrsp-2014-1

Pesnell, W. D., Thompson, B. J., & Chamberlin, P. C. 2012, Solar Physics, 275, 3, doi: 10.1007/s11207-011-9841-3

Pevtsov, A. A., Balasubramaniam, K. S., & Rogers, J. W. 2003, ApJ, 595, 500, doi: 10.1086/377339

Prasad, A., Bhattacharyya, R., Hu, Q., Kumar, S., & Nayak, S. S. 2018, ApJ, 860, 96, doi: 10.3847/1538-4357/aac265

Priest, E. 2014, Magnetohydrodynamics of the Sun (Cambridge University Press), doi: 10.1017/CBO9781139020732

Priest, E. R. 2020, Solar Physics: Overview, doi: 10.1093/acrefore/9780190871994.013.21

Priest, E. R., & Forbes, T. G. 2002, A&A Rv, 10, 313, doi: 10.1007/s001590100013

Rimmele, T. R., Warner, M., Keil, S. L., et al. 2020, SoPh, 295, 172, doi: 10.1007/s11207-020-01736-7

Sakurai, T. 1982, Solar Physics, 76, 301, doi: 10.1007/BF00170988

Sasso, C., Lagg, A., & Solanki, S. K. 2011, A&A, 526, A42, doi: 10.1051/0004-6361/200912956

—. 2014, A&A, 561, A98, doi: 10.1051/0004-6361/201322481

Savcheva, A., & van Ballegooijen, A. 2009, ApJ, 703, 1766, doi: 10.1088/0004-637X/703/2/1766

Scherrer, P. H., Schou, J., Bush, R. I., et al. 2012, Solar Physics, 275, 207, doi: 10.1007/s11207-011-9834-2

Schmieder, B., Aulanier, G., & Vršnak, B. 2015, SoPh, 290, 3457, doi: 10.1007/s11207-015-0712-1

Seki, D., Otsuji, K., Isobe, H., et al. 2019, PASJ, 71, 56, doi: 10.1093/pasj/psz031

—. 2017, ApJL, 843, L24, doi: 10.3847/2041-8213/aa7559

Shen, C., Xu, M., Wang, Y., Chi, Y., & Luo, B. 2018, ApJ, 861, 28, doi: 10.3847/1538-4357/aac204

Shibata, K., & Magara, T. 2011, Living Reviews in Solar Physics, 8, 6, doi: 10.12942/lrsp-2011-6

Shibata, K., Masuda, S., Shimojo, M., et al. 1995, ApJL, 451, L83, doi: 10.1086/309688

Shimizu, T., Nagata, S., Tsuneta, S., et al. 2008, SoPh, 249, 221, doi: 10.1007/s11207-007-9053-z

Shimizu, T., Imada, S., Kawate, T., et al. 2020, in Society of Photo-Optical Instrumentation Engineers (SPIE) Conference Series, Vol. 11444, Society of Photo-Optical Instrumentation Engineers (SPIE) Conference Series, 114440N, doi: 10.1117/12.2560887

Soni, S. L., Gupta, R. S., & Verma, P. L. 2020, Research in Astronomy and Astrophysics, 20, 023, doi: 10.1088/1674-4527/20/2/23

Spicer, D. S. 1982, SSRv, 31, 351, doi: 10.1007/BF00171370

Sturrock, P. A. 1966, Nature, 211, 695, doi: 10.1038/211695a0

Su, Y., van Ballegooijen, A., Lites, B. W., et al. 2009, ApJ, 691, 105, doi: 10.1088/0004-637X/691/1/105

Suematsu, Y., Tsuneta, S., Ichimoto, K., et al. 2008, SoPh, 249, 197, doi: 10.1007/s11207-008-9129-4

Toriumi, S., & Wang, H. 2019, Living Reviews in Solar Physics, 16, 3, doi: 10.1007/s41116-019-0019-7

Török, T., & Kliem, B. 2004, in ESA Special Publication, Vol. 575, SOHO 15 Coronal Heating, ed. R. W. Walsh, J. Ireland, D. Danesy, & B. Fleck, 56

Török, T., & Kliem, B. 2005, ApJL, 630, L97, doi: 10.1086/462412

Trujillo Bueno, J., Landi Degl'Innocenti, E., Collados, M., Merenda, L., & Manso Sainz, R. 2002, Nature, 415, 403. https://arxiv.org/abs/astro-ph/0201409

Tsuneta, S. 1996, ApJ, 456, 840, doi: 10.1086/176701

Tsuneta, S., Hara, H., Shimizu, T., et al. 1992, PASJ, 44, L63

Tsuneta, S., Ichimoto, K., Katsukawa, Y., et al. 2008, SoPh, 249, 167, doi: 10.1007/s11207-008-9174-z

UeNo, S., Nagata, S.-i., Kitai, R., Kurokawa, H., & Ichimoto, K. 2004, in Society of Photo-Optical Instrumentation Engineers (SPIE) Conference Series, Vol. 5492, Ground-based Instrumentation for Astronomy, ed. A. F. M. Moorwood & M. Iye, 958–969, doi: 10.1117/12.550304

van Ballegooijen, A. A., & Martens, P. C. H. 1989, ApJ, 343, 971, doi: 10.1086/167766

Vemareddy, P. 2019, ApJ, 872, 182, doi: 10.3847/1538-4357/ab0200

Vernazza, J. E., Avrett, E. H., & Loeser, R. 1981, ApJS, 45, 635, doi: 10.1086/190731

Wang, S., Jenkins, J. M., Martinez Pillet, V., et al. 2020, ApJ, 892, 75, doi: 10.3847/1538-4357/ab7380

Wiegelmann, T., Inhester, B., & Sakurai, T. 2006, Solar Physics, 233, 215, doi: 10.1007/s11207-006-2092-z

Wiegelmann, T., & Sakurai, T. 2012, Living Reviews in Solar Physics, 9, 5, doi: 10.12942/lrsp-2012-5

Xu, Y., Tian, H., Hou, Z., et al. 2022, ApJ, 931, 76, doi: 10.3847/1538-4357/ac69d5

Xu, Z., Lagg, A., Solanki, S., & Liu, Y. 2012, ApJ, 749, 138, doi: 10.1088/0004-637X/749/2/138

Yamasaki, D., Inoue, S., Bamba, Y., Lee, J., & Wang, H. 2022a, ApJ, 940, 119, doi: 10.3847/1538-4357/ac9df4

Yamasaki, D., Inoue, S., Nagata, S., & Ichimoto, K. 2021, ApJ, 908, 132, doi: 10.3847/1538-4357/abcfbb

Yamasaki, D., Nagata, S., & Ichimoto, K. 2022b, PASJ, 74, 1344, doi: 10.1093/pasj/psac072

Yamasaki, D., Huang, Y. W., Hashimoto, Y., et al. 2022c, Tech. Rep. from Astron. Obs. Grad. School of Science, Kyoto Univ., 6-2, doi: 2433/278126

Yan, X. L., Priest, E. R., Guo, Q. L., et al. 2016, ApJ, 832, 23, doi: 10.3847/0004-637X/832/1/23

Yan, X. L., Wang, J. C., Pan, G. M., et al. 2018, ApJ, 856, 79, doi: 10.3847/1538-4357/aab153

Yang, S., Zhang, J., Zhu, X., & Song, Q. 2017, ApJL, 849, L21, doi: 10.3847/2041-8213/aa9476

Yelles Chaouche, L., Kuckein, C., Martínez Pillet, V., & Moreno-Insertis, F. 2012, ApJ, 748, 23, doi: 10.1088/0004-637X/748/1/23

Yokoyama, T., Katsukawa, Y., & Shimojo, M. 2019, PASJ, 71, 46, doi: 10.1093/pasj/psz014

Zeeman, P. 1897, ApJ, 5, 332, doi: 10.1086/140355

Zhong, Z., Guo, Y., & Ding, M. D. 2021, Nature Communications, 12, 2734, doi: 10.1038/s41467-021-23037-8

Zirker, J. B., Martin, S. F., Harvey, K., & Gaizauskas, V. 1997, SoPh, 175, 27, doi: 10.1023/A:1004946303735